

Cross-Scatter in Dual-Cone X-ray Imaging: Magnitude, Avoidance, Correction, and
Artifact Reduction

by

William Michael Giles

Department of Medical Physics
Duke University

Date: _____

Approved:

Fang-Fang Yin, Co-Supervisor

James Bowsher, Co-Supervisor

James Colsher

Zhiheng Wang

Terence Wong

Dissertation submitted in partial fulfillment of
the requirements for the degree of Doctor of Philosophy in the Graduate Program in
Medical Physics in the Graduate School
of Duke University

2012

ABSTRACT

Cross-Scatter in a Dual-Cone X-ray Imaging System: Magnitude, Avoidance, and
Correction

by

William Michael Giles

Department of Medical Physics
Duke University

Date: _____

Approved:

Fang-Fang Yin, Co-Supervisor

James Bowsher, Co-Supervisor

James Colsher

Zhiheng Wang

Terence Wong

An abstract of a dissertation submitted in partial
fulfillment of the requirements for the degree
of Doctor of Philosophy in the Graduate Program in
Medical Physics in the Graduate School
of Duke University

2012

Copyright by
William Michael Giles
2012

Abstract

Onboard cone beam computed tomography (CBCT) has become a widespread means of three-dimensional target localization for radiation therapy; however, it is susceptible to metal artifacts and beam-hardening artifacts that can hinder visualization of low contrast anatomy. Dual-CBCT provides easy access to techniques that may reduce such artifacts. Additionally, dual-CBCT can decrease imaging time and provide simultaneous orthogonal projections which may also be useful for fast target localization. However, dual-CBCT will suffer from large increases in scattered radiation due to the addition of the second source.

An experimental bench top dual CBCT system was constructed so that each imaging chain in the dual CBCT system mimics the geometry of gantry-mounted CBCT systems commonly used in the radiation therapy room. The two systems share a common axis of rotation and are mounted orthogonally. Custom control software was developed to ensure reproducible exposure and rotation timings. This software allows the implementation of the acquisition sequences required for the cross scatter avoidance and correction strategies studied.

Utilizing the experimental dual CBCT system cross scatter was characterized from 70-145 kVp in projections and reconstructed images using this system and three cylindrical phantoms (15cm, 20cm, and 30cm) with a common Catphan core. A novel

strategy for avoiding cross-scatter in dual-CBCT was developed that utilized interleaved data acquisition on each imaging chain. Contrast and contrast-to-noise-ratio were measured in reconstructions to evaluate the effectiveness of this strategy to avoid the effects of cross scatter.

A novel correction strategy for cross scatter was developed wherein the cross scatter was regularly sampled during the course of data acquisition and these samples were used as the basis for low- and high- frequency corrections for the cross-scatter in projections. The cross scatter sampling interval was determined for an anthropomorphic phantom at three different sites relevant to radiation therapy by estimating the angular Nyquist frequency. The low frequency portion of the cross scatter distribution is interpolated between samples to provide an estimate of the cross scatter distribution at every projection angle and was then subtracted from the projections.

The high-frequency portion of the correction was applied after the low-frequency correction was applied. The novel high-frequency correction utilizes the fact that a direct estimate of the high-frequency components was obtained in the cross scatter samples. The high-frequency components of the measured cross scatter were subtracted from the projections in the Fourier domain, a process referred to as spectral subtraction. Each projection is corrected using the cross scatter sample taken at the closest projection angle. In order to apply this correction in the Fourier domain the high-frequency component of the cross scatter must be approximately stationary. To improve the

stationarity of the high-frequency cross scatter component a novel two-dimensional, overlapping window was developed. The spectral subtraction was then applied in each window and the results added to form the final image.

The effectiveness of the correction techniques were evaluated by measuring the contrast and contrast-to-noise-ratio in an image quality phantom. Additionally, the effect of the high-frequency correction on resolution was measured using a line pair phantom.

Cross scatter in dual CBCT was shown for large phantoms to be much higher than forward scatter which has long been known to be one of the largest degrading factors of image quality in CBCT. This results in large losses of contrast and CNR in reconstructed images. The interleaving strategy for avoiding cross scatter during projection acquisition showed similar performance to cross scatter free acquisitions, however, does not acquire projections at the maximum possible rate. For those applications in which maximizing the acquisition rate of projections is important, the low- and high-frequency corrections effectively mitigated the effects of cross scatter in the dual CBCT system.

Contents

Abstract	iv
List of Tables	xiii
List of Figures	xiv
List of Abbreviations	xix
Acknowledgements	xxi
1. Introduction	1
1.1 General Introduction	1
1.2 Motivation	1
1.3 Overview of Chapters	3
2. Background	6
2.1 Current Applications of CBCT	6
2.2 Principles of CBCT	7
2.2.1 Data Acquisition	7
2.2.1.1 Flat-Panel Imagers	7
2.2.1.2 Geometry	8
2.2.1.3 Projection Acquisition Geometry	9
2.2.2 Bowtie Filters	10
2.3 Scatter in CBCT	10
2.3.1 Scatter Effects	10
2.3.2 Current Methods for Addressing Scatter in CBCT	11

2.3.2.1	Measurement-Based Methods	12
2.3.2.2	Computational Methods.....	13
2.3.2.3	Beam Modulation	14
2.4	Dual-Cone Flat-Panel Systems.....	15
2.4.1	Advantages	16
2.4.2	Compounded Scatter Problem	16
3.	Development of Dual-Source Cone Beam System.....	18
3.1	System Components.....	18
3.1.1	Detectors	20
3.1.1.1	Detector Readout Cycle	20
3.1.1.2	Image Processing.....	21
3.1.1.3	Detector/System Interface	22
3.1.2	Generators and X-ray Tubes.....	23
3.1.2.1	Programming the Generator	24
3.1.2.2	Generator Hardware Interface.....	24
3.1.3	Motion Controller and Rotational Stage	25
3.2	Hardware Interface	27
3.2.1	Electrical Isolation	27
3.2.2	Computer Interface	29
3.3	Software Control.....	32
3.3.1	Normal Scanning.....	32
3.3.2	Periodic Cross-Scatter Sampling	35

3.4	Image Artifacts.....	38
3.5	Future Directions	39
4.	Geometric Artifacts in CBCT	40
4.1	Motivation	40
4.2	Methods	43
4.2.1	Numerical Investigation into Mechanical Causes of the Artifact.....	44
4.2.2	Clinical-Scanner Study of Artifact Reduction	46
4.3	Results	48
4.3.1	Numerical Investigation into Mechanical Causes of the Artifact.....	48
4.3.2	Clinical-Scanner Study of Artifact Reduction	51
4.4	Discussion.....	54
4.5	Conclusion	56
5.	Magnitude and Avoidance of Cross-Scatter Effects in Dual CBCT	57
5.1	Motivation	57
5.2	Methods	57
5.2.1	Acquisition Sequences	57
5.2.2	Phantoms	59
5.2.3	Imaging Technique	60
5.2.4	Measurements of Forward Scatter in Projections	61
5.2.5	Image Reconstruction	62
5.2.6	Quantitative Analysis of Scatter in Projections.....	62
5.2.7	Quantitative Analysis of Scatter in Reconstructions	64

5.3	Results	65
5.3.1	Projection Effects	65
5.3.2	Reconstruction Effects	70
5.4	Discussion.....	73
5.5	Conclusions	76
6.	Deterministic Cross Scatter Correction	78
6.1	Motivation	78
6.2	Correction Strategy Overview	79
6.3	Materials and Methods.....	81
6.3.1	Correction Strategy	81
6.3.2	Cross-Scatter Sampling Frequency	83
6.3.2.1	Nyquist Sampling Frequency	85
6.3.2.2	Empirical Sampling Frequency	87
6.3.3	Correction Evaluation.....	87
6.4	Results	88
6.4.1	Cross-Scatter Sampling Frequency	88
6.4.1.1	Nyquist Sampling Frequency	88
6.4.1.2	Empirical Sampling Frequency	91
6.4.2	Correction Evaluation.....	93
6.5	Discussion.....	96
6.6	Conclusion	97
7.	Stochastic Scatter Correction.....	98

7.1	Motivation	98
7.2	Methods and Materials	98
7.2.1	Theoretical Basis for Spectral Subtraction	98
7.2.2	Application of Spectral Subtraction for Cross Scatter Correction	100
7.2.3	Windowing.....	102
7.2.4	Correction Evaluation.....	105
7.3	Results	107
7.4	Discussion.....	110
7.5	Conclusion	113
8.	Summaries and Conclusions	114
9.	Appendix: Dual Source CBCT User Guide.....	117
9.1	Hardware Power-Up Procedures.....	117
9.2	Data Acquisition	118
9.2.1	Tab 1: Set Detector Frame Rate.....	118
9.2.2	Tab 2: Calibrate Detectors	121
9.2.3	Tab 3: Exposure Parameters.....	122
9.2.4	Tab 4: Begin Exposure	124
10.	Appendix: Dual Source CBCT Troubleshooting Guide	126
10.1	Motion Controller.....	126
10.1.1	Begins Rotation Too Early	126
10.1.2	Does Not Rotate	126
10.1.3	No Motor Detected	127

10.2	Detectors	128
10.2.1	Cannot Initialize Camera	128
10.2.2	Allocate Buffers	128
10.3	Generators	128
	References	129
	Biography	137

List of Tables

Table 1.1: Specific aims.....	2
Table 5.1: Material and nominal CT number for each plug in the Catphan core.	60
Table 5.2: Exposure parameters used for all studies in this chapter.....	61
Table 6.1: Contrast and CNR recovery for the uncorrected case with cross scatter and with the correction applied. The reductions reported are relative to a scan of equal dose, but no cross scatter present in the scan.....	95
Table 7.1: Physical size of the line pairs used to measure resolution.	107
Table 7.2: Contrast and CNR recovery relative to the cross scatter free case for 8 cases: no correction; low-frequency (LF) correction only, no windowing (Equation (7.9)), and with windowing for 5 different values of r	108
Table 7.3: Normalized contrast for the plots in Figure 7.6.	109

List of Figures

Figure 3.1: The dual X-ray system with a pelvic phantom ready to be imaged.....	19
Figure 3.2: Schematic diagram of the dual X-ray system illustrating the geometry and origins of forward and cross scatter as well as the system control components.	19
Figure 3.3: Cross sectional schematic of generic amorphous silicon detector. ICS is short for integrated circuits [24].....	20
Figure 3.4: Diagram illustrating how the detector scans each line of pixels	21
Figure 3.5: Generator console.....	24
Figure 3.6: Rotation stage mounted on table with largest PVC spacer.	26
Figure 3.7: A simple circuit diagram illustrating the basic principle of optoisolation.....	27
Figure 3.8: Simple diagram of relays used to trigger the optoisolated circuits within the generator room interface board.	29
Figure 3.9: Schematic wiring diagram of the dual X-ray control system.....	31
Figure 3.10: Schematic representation of cross scatter sampling pulse sequence.....	37
Figure 3.11: Artifacts caused by inconsistent User_Sync signal.....	38
Figure 3.12: Stripe artifact caused by exposing during the readout period of the detector.	39
Figure 4.1: Imaging artifacts caused by shifts in a step-wedge style bowtie filter observed in the experimental dual X-ray imaging system.....	41
Figure 4.2: Reconstruction of a uniform phantom by the clinical reconstruction engine. The dark and light bands seen in this image of a uniform phantom are characteristic of the crescent artifacts in some clinical scanners.....	42
Figure 4.3: Geometry used for the simulation studies. For the tube-rotation simulations, the radius of rotation was set to 1, 5, and 10 cm behind the focal spot.....	45

Figure 4.4: A projection of the bowtie filter with the tungsten wires in place. The dotted lines indicate the regions used to track changes in position as a function of angle. The thickness difference between wires is due to the different magnification factors in the trough of the bowtie filter versus at the top..... 46

Figure 4.5: Plots of measured COM and wire shifts versus gantry angle..... 49

Figure 4.6: Reconstructions of blank scans by the in-house implementation of FDK resulting from (a) simulated bowtie filter sag, (b) simulated X-ray tube sag , and (c) simulated tube rotation with ROR = 1 cm. (d) Horizontal profiles through the center of the reconstructions in (a) and (c). 50

Figure 4.7: Profiles through the center of the reconstructed image (solid line) and through blank projections (dashed and dotted lines). The profiles through blank projections are scaled to the width they would have if the projection plane passed through the center of the image space. The two blank-projection profiles (dashed and dotted lines) indicate the minimum and maximum bowtie shifts, which occur at projection angles of 0° and 140°. The boxes indicate the location of the artifact relative to the shapes of the blank projection profiles. 51

Figure 4.8: In-house FDK reconstructions of a uniform phantom utilizing (a) 1 blank, (b) 175 blanks, and (c) 380 blanks. (d) The RMS error in reconstructions using a variable number of projections in the blank scan. The range plotted represents reconstructing with 1 to 380 blanks over a 200 degree scan angle. Data points for 40, 175, and 380 blanks are identified by the 3 labeled arrows..... 53

Figure 4.9: Patient images reconstructed with the in-house implementation of FDK using (a) a single blank and (b) 380 blanks. (c) The subtraction of fig 8a. and fig 8b. The dashed line indicates where the profiles (d) were taken. The arrows in (d) indicate where the crescent artifacts are located..... 54

Figure 5.1: Schematic representations of three projection acquisition sequences: (a) simultaneous, (b) interleaved, and (c) sequential..... 59

Figure 5.2: Reconstructed slice of the Catphan showing the ROIs of varying contrast. The solid circles indicate the ROI regions in Equations (5.7-9) while the dashed circles indicate the pixels used as the background (BG) regions in Equations (5.7-9). 65

Figure 5.3: Plots of CS (left) and FS (right) for the 20 cm phantom. The CS is heavily sloped in the transaxial direction, increasing towards the orthogonal source. It also

shows a peak in the axial direction in the center of the detector. This differs from FS which is symmetric in the axial and transaxial directions. 66

Figure 5.4: (a) Projection of the Catphan® at 100kVp, with BSA in place, and taken with Tube/Detector 1, without firing Tube 2. (b) The cross scatter as imaged by Detector 2 during the projection in Figure 5.4a. (c) The forward scatter component estimated from the projection in Figure 5.4a. (d) Horizontal profiles taken through Figure 5.4a-c at the position indicated by the arrow in Figure 5.4a. The left side of the cross scatter profile is closest to the orthogonal detector. 67

Figure 5.5: (a) Forward Scatter Fraction as a function of kVp. (b) Cross Scatter Fraction as a function of kVp. (c) Forward Scatter to Primary Ratio. (d) Cross Scatter to Primary Ratio. (e) Scatter to Primary Ratio. (f) Cross Scatter to Forward Scatter Ratio. Error bars are only shown for series when the bars are larger than the data markers. 69

Figure 5.6: Plots of CS, FS, and primary transmission (T-CS-FS) all normalized to the initial intensity I_0 . The cross scatter (CS) normalized to the initial intensity is independent of phantom size. This suggests that the large changes seen in the cross-scatter fractions and scatter-to-primary ratios observed in Figure 5.5 are driven largely by changes in the primary transmission and forward scatter. 70

Figure 5.7: Reconstructed slices of the 20cm phantom at 100 kVp for acquisition protocols: (a) simultaneous, (b) interleaved, and (c) sequential. The window for the reconstructions is [-1000, 1000] and the level is 0 HU. (d) Profiles through each image along the dashed line in (a). The interleaved and sequential reconstructions have the same contrast. The reduction in contrast in the simultaneous reconstruction seen in the profiles manifests as a visibly darker image in Figure 5.7a. 71

Figure 5.8: Plots of the reconstructed HU values for each ROI vs. the nominal HU values are shown for the (a) 15cm and (b) 30cm phantoms. The dashed line indicates the identity line where the reconstructed HU is equal to the nominal HU. The sequential acquisitions are not shown because they directly overlap the interleaved acquisitions. .72

Figure 5.9: The numbers above each group of three acquisitions indicate the diameter of the phantom used for those measurements. (a) Contrast in all ROIs at 100 kVp. (b) Contrast in ROI 1 at all kVps. (c) CNR in all ROIs at 100 kVp. (d) CNR in ROI 1 for all kVps. Both contrast (C) and CNR are approximately the same for the sequential and interleaved acquisitions. However, the simultaneous acquisition shows a decrease in contrast and CNR compared with the other two acquisitions. Data for the 20cm phantom are not displayed here, but follows the same trends. 73

Figure 6.1: Illustration of the cross-scatter sampling protocol and flowchart of the correction strategy	80
Figure 6.2: Representation of radially symmetric low-pass filter.	82
Figure 6.3: Anthropomorphic pelvic phantom.	84
Figure 6.4: Anthropomorphic phantom used for the head and neck and lung anatomic sites.....	85
Figure 6.5: Cross-scatter angular frequency content of anthropomorphic pelvic phantom.	90
Figure 6.6: Cross-scatter angular frequency content of anthropomorphic lung phantom.	90
Figure 6.7: Cross-scatter angular frequency content of anthropomorphic lung phantom.	91
Figure 6.8: Scatter estimation error averaged over all pixels as a function of projection angle for 3 and 10 cross-scatter samples in a 110 degree acquisition.	92
Figure 6.9: Mean error in interpolated cross-scatter distributions averaged over all pixels and projection angles as a function of the number of cross-scatter samples taken.	93
Figure 6.10: Reconstructed image of the Catphan showing the ROI numbers and indicating where the profiles for Figure 6.11 were taken.....	94
Figure 6.11: Horizontal profiles through reconstructions along the line indicated in Figure 6.10.....	95
Figure 7.1: Flowchart of spectral magnitude subtraction.....	100
Figure 7.2: Flowchart of the spectral subtraction process as it is applied in the high-frequency component of the cross scatter correction.....	101
Figure 7.3: A two-dimensional plot of the overlapping window.....	103
Figure 7.4: Four overlapping windows offset by a half the total width of the window (r). The shaded region in the upper right indicates the size of a single window and the region indicated by the dashed lines shows where the four windows overlap.....	104

Figure 7.5: Reconstructed slice of the line pair gauge of the Catphan. The number line pairs are the ones that were used to measure resolution. Their physical dimensions are given in Table 7.1.	106
Figure 7.6: Plots of the normalized contrast for the low-frequency correction alone, the high-frequency correction with no windowing, and the high-frequency correction with windows of various sizes. The values plotted here are listed in Table 7.3.	109
Figure 7.7: The stationarity of the noise within the windowed segments for varying window sizes.	110
Figure 9.1: Tab 1 of the control software.....	119
Figure 9.2: The second tab in the control software GUI.	122
Figure 9.3: The third tab in the control software GUI.....	123
Figure 9.4: The final tab in the control GUI.....	124

List of Abbreviations

1D	one-dimensional
2D	two-dimensional
3D	three-dimensional
4D	four-dimensional
a-Se	amorphous selenium
a-Si:H	amorphous hydrogenated silicon
BSA	beam stop array
CBCT	cone beam computed tomography
CNR	contrast to noise ratio
COM	center of mass
Cs:TI	thallium activated cesium iodide
CT	computed tomography
DSCT	dual-source ct
DTS	digital tomosynthesis
FBP	filtered back projection
FDK	Feldkampp Davis Kress reconstruction algorithm
FOV	field of view
FPS	frames per second

I/O	input/output
IGRT	image guided radiation therapy
kVp	peak kilovoltage
MTF	modulation transfer function
OBI	on board imager
RMSE	root mean squared error
ROI	region of interest
ROR	radius of rotation
SAD	source to axis distance
SID	source to imager distance
TFT	thin film transistor

Acknowledgements

First, I would like to thank my advisors Dr. Fang-Fang Yin and Dr. James Bowsher. Dr. Yin arranged financial support for this project. I would also like to thank Dr. Yin for challenging me with detailed questions. Dr. Bowsher has been an incredible mentor who taught me to be a more thorough scientist. I want to thank Dr. Bowsher for always making time for my questions. To the rest of my committee: Dr. James Colsher, Dr. Zhiheng Wang, and Dr. Terrence Wong, I thank all of you for the time you have spent reading my work and for all of your helpful feedback and criticisms.

Finally, I would like to thank my wife, Janice, for her unwavering support. The encouragement and comfort that you provided through the highs and lows of graduate school has been invaluable.

1. Introduction

1.1 *General Introduction*

This dissertation examines the hypothesis that dual X-ray imaging can be implemented with negligible degradations of image quality due to cross scattered radiation.

1.2 *Motivation*

Gantry-mounted conebeam computed tomography (CBCT) with flat panel imagers plays a key role in radiation therapy and is the predominant means of three-dimensional positioning verification and target localization. CBCT currently suffers three drawbacks: poor rejection of scattered radiation which degrades image quality, slow data acquisition rates which limit its ability to image moving anatomy and increase the amount of time the patient spends on the treatment couch, and artifacts caused by beam hardening and photon starvation which can obfuscate the anatomy of interest. Adding a second detector and X-ray source in an orthogonal position – i.e. dual CBCT – potentially alleviates two of these drawbacks. It inherently increases the data acquisition rate by approximately a factor of two. Secondly, it provides the means to perform dual energy techniques that can reduce metal artifacts and beam hardening artifacts to allow better visualization of soft tissues. However, the second X-ray source introduces a second source of scattered photons. This is referred to as cross scatter. This work is largely concerned with the development of an experimental dual CBCT scanner, the

characterization of cross scatter within that system, and techniques to avoid or correct the effects of cross scatter in the dual CBCT system.

During our investigations into cross scatter, we became aware of artifacts that are common in some clinical onboard CBCT scanners. Similar artifacts were observed in the experimental system which provided insight into the artifacts in the clinical scanners. Accordingly, potential causes of the artifact were studied and a correction technique was developed. The four specific aims of this project are presented in Table 1.1.

Table 1.1: Specific aims.

Specific Aim 1: Develop bench-top dual-cone X-ray system
1.a Install system hardware
1.b Design and implement a control system, including software and hardware components, for dual-cone imaging system
1.c Identify sources of any system artifacts and implement protocols and techniques to eliminate these artifacts
1.d Update control software to allow for protocols developed in Aim 4.
1.e Write user manual and troubleshooting guide for system
Specific Aim 2: Investigate source of crescent artifact
2.a Develop explanation for and hypotheses regarding the source of crescent artifacts
2.b Simulate three mechanical deviations that are hypothesized to lead to crescent artifacts
2.c Develop method to correct for the crescent artifacts
2.d Apply correction to clinical scans
Specific Aim 3: Characterize cross scatter effects in dual-cone system for different

acquisition modes
3.a Develop dual-cone acquisition methods that may alleviate cross-scatter effects
3.a Investigate magnitude of cross scatter in projections
3.b Investigate effects of cross scatter in reconstructions
Specific Aim 4: Develop cross scatter correction method
4.a Develop cross-scatter sampling protocol
4.b Develop correction for deterministic component
4.c Develop correction for stochastic component
4.d Evaluate correction in tomographic data sets

1.3 Overview of Chapters

Chapter 2: *Background and Significance* provides an overview of the principles of cone-beam ct (CBCT) and its applications. Also discussed are the potential advantages a dual-cone system provides over current CBCT systems. The chapter concludes with a review of the effects of scatter in current CBCT and dual-source CT systems and methods that have been employed in the literature to reduce these effects.

Chapter 3: *Development of Dual Source Cone Beam System* is a discussion of the hardware and software used in the experimental system. This chapter covers the completion of specific aim 1 and its sub-aims. The operating principles of each component are discussed as well as how each component interfaces with the rest of the system. Finally, a description of the control software is provided.

Chapter 4: *Geometric Artifacts in Cone-Beam CT* discusses specific aim 2 and its sub-aims. Geometric artifacts are currently seen in clinical gantry-mounted CBCT systems. Simulation studies of one of these systems were performed to identify potential causes of the artifacts. Additionally, a practical correction technique was developed to mitigate the artifact. Findings from this chapter were published in a peer-reviewed journal *Medical Physics*, 38(4): 2116-21 March 2011.

Chapter 5: *Characterization of Cross Scatter* describes investigations into the magnitude of cross scatter and its effects in fulfillment of specific aim 3 and its sub-aims. The magnitude and effects of cross scatter in the experimental system for three different acquisition protocols, three different phantom diameters, and six beam energies. The magnitude of cross scatter was measured in 2D projections and the effects of cross scatter were evaluated in reconstructed images. A cross scatter avoidance technique, interleaved acquisitions, is proposed and evaluated in this chapter. Findings from this chapter have been submitted for publication in the peer reviewed journal *Medical Physics*.

Chapter 6: *Deterministic Cross Scatter Correction* proposes a novel technique for estimating and subtracting the low-frequency, deterministic components of cross scatter in dual CBCT in completion of specific aims 4.a and 4.b. The correction is based on regular sampling of the cross scatter during projection acquisition and includes a study into the necessary sampling interval required to perform the proposed correction.

Chapter 7: *Stochastic Cross Scatter Correction* discusses a novel approach to correcting for the high-frequency, stochastic components of cross scatter in dual CBCT. This chapter covers the investigations performed in completion of specific aims 4.c and 4.d.

2. Background

2.1 *Current Applications of CBCT*

Investigations into the use of flat-panel imagers for CBCT began in the late 1990's [1-3]. A typical CBCT system consists of a kilovoltage X-ray source, flat panel detector, and a rotation mechanism. CBCT has been widely adopted as a means of 3D localization for image guided radiation therapy and kilovoltage imaging systems for CBCT are commonly found mounted onto clinical linear accelerators [4-8]. On-going research is working to expand the capabilities of the on-board CBCT systems to 4D CBCT [9-11] as well as 3D and 4D digital tomosynthesis (reconstructions using limited angle scans) [12-16].

Mobile C-arm systems have gained widespread use as method for intraoperative 3D imaging. These systems tend to have similar geometry as those used for on-board imaging in radiation therapy with the exception that they are on their own, mobile gantry. The mobile systems are capable of CBCT, DTS, fluoroscopy, and radiography. They are commonly used to help guide head, neck, and spinal surgeries [17-20]. C-arm CBCT has also been used for dosimetry verification of prostate seed implants [21].

CBCT has also been adopted for use in dentistry and oral surgery. These systems typically have fixed anode X-ray tubes and operate at lower energies. Additionally, the patient is usually imaged in a sitting or standing position. The SAD and SDD also tend to be must smaller than in C-arm or gantry mounted systems. [22, 23]

2.2 Principles of CBCT

Here the principles that make CBCT possible, from the acquisition of data to the reconstruction, are discussed. Special emphasis is placed on the work of those who have pioneered the development and use of CBCT for image guidance of radiation therapy. Herein, CBCT will refer to cone-beam computed tomography with flat panel detectors.

2.2.1 Data Acquisition

2.2.1.1 Flat-Panel Imagers

There are two categories of flat-panel imagers: direct and indirect conversion. Direct detection flat-panel imagers are typically composed of a layer of photo-conducting amorphous selenium (a-Se) between a metal plate electrode and an array of charge collecting electrodes [24, 25]. A bias voltage is applied across the electrodes which moves charge to the charge collecting electrodes which are each connected to charge storage capacitors and thin film transistor (TFT) switches [24]. The TFT switches are used to release the charge during the readout cycle. This design of detector is generally not suitable for tomography because after every exposure the detector must be exposed to light for several seconds to remove charge still trapped in the detection elements [24].

Indirect conversion detectors use an intermediary X-ray fluorescent layer to convert X-rays to visible light which is then detected by an array of amorphous hydrogenated silicon (a-Si:H) photodiodes. The most commonly used fluorescent

material is thallium activated cesium iodide (CsI:Tl). The detection efficiency of the photodiodes for the light emitted from CsI:Tl is about 80%. An added benefit of the CsI:Tl is its channeled structure which acts similarly to fiber optic cables such that light is guided along the channel. This minimizes scatter of emitted light and maintains spatial resolution.

During the readout of each pixel the accumulated charge is discharged. The rate at which charge leaves the pixel is the main factor in magnitude of lag effects for both types of flat panel imagers. If all of the accumulated charge cannot be discharged from a pixel in the allotted readout time, then there is latent charge which contributes to the signal of the next frame [26-28]. This can cause artifacts that are typically minor in comparison to the contrast of patient anatomy in kilovoltage imaging [27, 28]. However, these effects can be substantial in megavoltage 3D imaging [26].

2.2.1.2 Geometry

In 2000, Siewerdsen and Jaffray published their findings on the optimal magnification factor in CBCT [29]. The magnification factor (M) is defined in Equation (2.1), where SID is the source to imager distance and SAD is the source to axis distance.

$$M = \frac{SAD}{SID} \quad (2.1)$$

Optimal values of M were calculated for focal spot size, imaging task (localization of varying size objects), X-ray scatter fraction, detector spatial resolution, and exposure. Of the studied parameters, X-ray scatter fraction was the most dominant and it was found

that a magnification of between 1.4 and 1.6 is optimal for highly scattering objects such as a human. Clinical systems such as the Varian on-board CBCT system have magnification factors of 1.5.

If the imager is positioned such that a ray from the focal spot to the center of the detector is perpendicular to the imager and passes through the axis of rotation, a magnification factor of 1.5 provides a reconstructed field of view (FOV) of approximately 26.5cm in diameter for the imagers described in section 3.1.1 that have an active width just under 40cm. Varian uses similar imagers in their on-board CBCT systems and can achieve a FOV of 40cm when by shifting the detector to one side and collimating the beam appropriately. Varian refers to this as “half-fan” mode. In both modes the FOV extends approximately 14cm in the axial direction. [30]

2.2.1.3 Projection Acquisition Geometry

Most CBCT systems use a circular orbit wherein projections are acquired evenly spaced and the imager and X-ray source both move along a circular trajectory. Smith [31] showed that for a circular orbit, only the central slice is fully sampled. This leads to what is known as the cone-beam effect in the superior and inferior slices of CBCT reconstructions [32]. Several other orbits have been proposed [33-36], however, circular orbits are still the most common.

2.2.2 Bowtie Filters

Compensators that selectively attenuate the X-ray beam near on the periphery of the FOV are commonly referred to as bowtie filters. The increased attenuation near the periphery of the beam is designed to compensate for the expected lack of attenuation by the object being imaged in the periphery, when the object is cylindrical or near cylindrical. This reduces the dynamic range constraints of the detector and helps to avoid saturation of pixels in these regions [37]. Saturation of the detector can lead to skin line loss and bones that appear to protrude from the patient. Bowtie filters have also been shown to reduce beam hardening [37-39], patient dose [40, 41], and scatter [41, 42]. These improve image uniformity, skin line, CT number linearity, and contrast.

2.3 Scatter in CBCT

Early in the development of CBCT scatter was identified as a large degrading factor of image quality and remains one of the largest degrading factors of image quality in CBCT today. The scientific community has invested substantial effort into characterizing the effects of scatter in CBCT and developing various techniques for reducing those effects.

2.3.1 Scatter Effects

The most widely cited paper on the effects of scatter was published in 2001 by Siewerdsen and Jaffray [43]. In their paper, they have shown that the number of detected scattered photons can exceed the number of detected primary photons even for optimal

CBCT geometries that utilize a large air gap. They reported errors in CT number and reductions in contrast and contrast-to-noise ratio. Taken together, these effects were seen to reduce the visibility of soft tissue which makes it difficult to localize soft tissue targets for IGRT.

Siewerdsen and Jaffray's observations were consistent with those of Glover who examined the effects of scattered radiation in fan-beam CT [44]. Glover found that scatter can lead to cupping artifacts, or dipping of the CT number in the center of an image, as well as streaking artifacts near high contrast objects. Glover also noted that as the collimation of beam is reduced – *i.e.* the beam becomes wider – the effects of scatter, expectedly, increase.

Endo et al. showed that scattered radiation substantially increases the noise in reconstructed images [45]. They also noted that a focused collimator greatly reduces these effects. Conventional anti-scatter grids were also shown improve the noise performance, but to a lesser degree.

2.3.2 Current Methods for Addressing Scatter in CBCT

There are many methods for addressing scattered photons in CBCT published in the literature. These methods tend to fall into one of three categories: measurement-based methods, computational methods, and beam-modulation methods. Measurement-based methods rely on using some form of beam blocker to measure scatter intensity at certain locations and estimate the distribution from these measurements. Computational

methods are those that rely on analytical approximations or results from Monte Carlo simulations as the basis of their scatter estimations. Several authors have also explored modulation the primary beam as a method of separating the primary signal (which has a minimum possible frequency due to the modulation) from the scatter distribution.

2.3.2.1 Measurement-Based Methods

A quintessential example of a measurement-based scatter correction method is patented by Ning [46]. He proposed the use of an array of beam blockers made from lead, commonly referred to as a beam stop array (BSA). It can be assumed that all of the primary photons are attenuated by the BSA and that any detected signal behind the array is due to only scattered photons. This allows an estimate of the scatter intensity at various points across the detector. The scatter distribution across the detector can then be interpolated from the measurements behind the BSA. Ning further proposed to only use the BSA periodically throughout the scan and interpolate across the angular direction to estimate the scatter distribution for all angles. The scatter distributions were subtracted from the projections prior to reconstruction.

Many other measurement-based methods have been proposed and all rely on somehow measuring the scatter at various points and interpolating to estimate the rest. One such proposed method suggests collimating the X-ray beam in the axial direction such that the scatter can be measured behind the collimator shadows and interpolated across the rest of the projection [47]. Flohr [48] has proposed a similar method in dual-

source CT whereby, scatter is measured using detector elements not illuminated by the primary beam and then interpolated across the other detector elements.

Other authors have proposed beam block arrays that are composed of large lead strips that block much larger portions of the image compared to conventional BSAs. These methods have the added advantage of blocking more of the primary beam which directly reduces the amount of scattered photons. Typically the lead strips are arranged such that after a 360° the object is still fully sampled (or nearly so). [49, 50]

2.3.2.2 Computational Methods

A first order analytic approximation of Compton scatter effects in CBCT was derived by Yao and Leszczynski [51]. They also described an implementation of their approximation [52] in which a primary reconstruction is performed of the raw data and the scatter distributions are calculated from the reconstructed attenuation. In their approximation, they allow for heterogeneous objects of arbitrary shape and for polyenergetic X-ray beams. They showed good agreement with Monte Carlo simulation of X-ray scatter that was generally within 5%. However, this approach has two main drawbacks: it is not as accurate as some of the measurement based methods and it requires accurate modeling of the beam spectrum and of the detector response. Errors in the detector response model or the beam spectrum model can greatly increase the error of the approximation. Once the scatter distribution is estimated it can be subtracted from

the projection data and a second reconstruction is performed. Alternatively, the scatter distributions can be reconstructed and then subtracted from the primary reconstruction.

Another type of computational approach mixes in elements of the measurement-based approaches. It is based on creating a library of scatter distributions for scattering plates of different thicknesses and then matching the scatter library to each individual projection [53]. The scatter distributions are then subtracted from the projections prior to reconstruction. This is classified as a computational method because no measurements of the scatter distributions for an individual object are made.

2.3.2.3 Beam Modulation

Beam modulation has recently been explored as a method to make the primary distribution and the scatter distribution separable in each projection without completely attenuating the primary beam at any point. This was first described by Zhu et al. using a semi-transparent beam blocker in a checkerboard pattern [54]. The checkerboard pattern modulates the primary signal which forces it into a higher frequency portion of the Fourier domain. It is then assumed that the scatter distribution occupies the lower frequency portions of the Fourier domain. This allows the two distributions to be mathematically separable. Of course, the modulated X-ray distribution is taken into account for image reconstruction. Modulation techniques can provide very good rejection of the low frequency components of the scatter distribution, however, they suffer greatly from beam hardening effects caused by the modulators.

2.4 Dual-Cone Flat-Panel Systems

Orthogonal dual-source X-ray imaging with flat panels has been examined for its ability to localize radio-opaque markers in three dimensions [55-57]. These systems have been mounted on linear accelerators and used clinically for orthogonal fluoroscopy and radiography in efforts to better localize anatomy or markers prior to or during radiation therapy [58].

Currently, there are several commercial imaging systems available for IGRT applications that utilize dual-source X-ray imaging. One of these systems by BrainLAB (BrainLAB AG Feldkirchin, Germany) uses two oblique imagers to provide high quality radiographs that can be used to check the alignment of bony anatomy of the patient versus the planned position [59] as well as the location of implanted fiducial markers [60]. The geometry of this system is such that the air gap between the patient and the detector greatly reduces the effects of scatter. The X-ray tubes and detectors of this system are fixed and therefore it is incapable of tomographic imaging. Another commercial system, which is capable of tomographic imaging, is the Vero SBRT system, also by BrainLAB, utilizes orthogonal view flat panel detectors to provide guidance for stereotactic body radiation therapy (SBRT) [61-63].

2.4.1 Advantages

In multi-slice CT the introduction of dual-source systems has allowed for improved temporal resolution [64] which can freeze cardiac motion. It also allows for dual-energy scans to be performed without the use of fast kV switching [65].

A dual-source, dual-detector CBCT system could provide several advantages over the single cone-beam system. It would have potential to provide dual-energy imaging without the use of fast kV switching [65]. The dual CBCT system may also reduce the total scan time required compared to current single CBCT systems. A dual cone-beam system could be configured with two non-coplanar imaging chains which may help alleviate cone-beam artifacts [66, 67] as well as extend the axial FOV. A dual cone-beam on-board imaging device would also allow for simultaneous, orthogonal radiographs, which have been shown to be highly useful in similar systems for target localization [59]. Finally this system would facilitate dual-arc digital tomosynthesis [68].

2.4.2 Compounded Scatter Problem

The largest disadvantage of a second X-ray tube is that there is now a second source of scattered photons in the imaging system. Scatter generated by one X-ray tube can be detected by both imagers. Cross-scatter effects have been studied in dual-source, multi-slice CT by several authors and can in some instances be a greater degrading factor than forward scatter [69-72]. In CBCT scatter is already the one of the largest degrading factors of image quality and in dual-cone CBCT a second and potentially

larger source of scatter is added to the imaging system. Given that, much of the following work is devoted to characterizing and addressing the cross scatter problem

3. Development of Dual-Source Cone Beam System

3.1 System Components

The dual X-ray system models the kV imaging systems commonly found on clinical linear accelerators. What makes this system unique is that it uses two separate imaging chains, each consisting of an X-ray tube, detector, and stage, to acquire tomographic data. Each detector is nominally positioned 50 cm from the rotational center of the stage and 150 cm from the focal spot of its respective tube. Each tube and detector is aligned such that the central ray passes through the axis of rotation of the stage and the central rays for each tube are at a right angle, as shown in Figure 3.1 and Figure 3.2. The system is capable of tomography as well as simultaneous, orthogonal radiography and fluoroscopy.

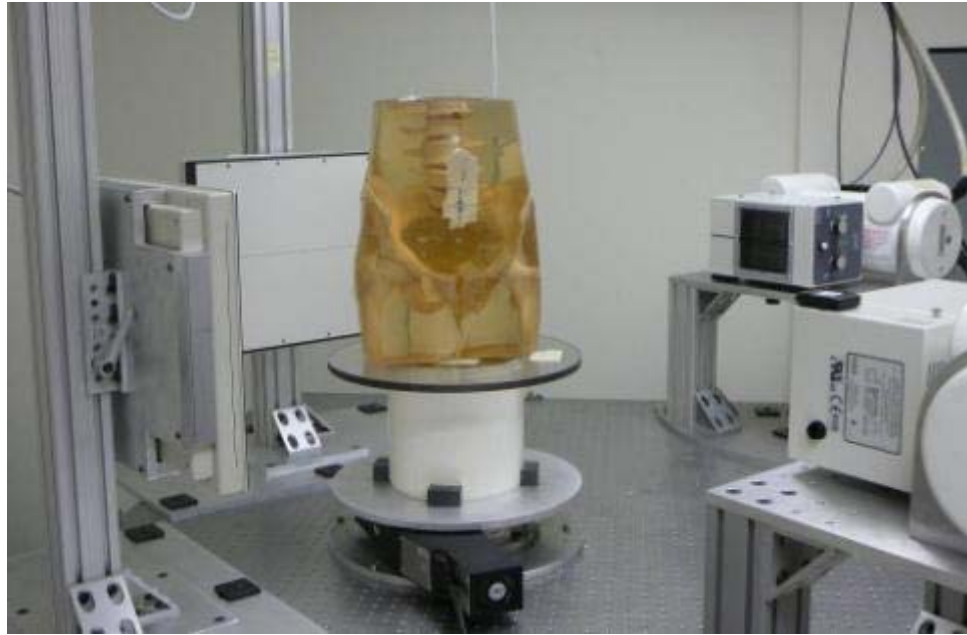


Figure 3.1: The dual X-ray system with a pelvic phantom ready to be imaged.

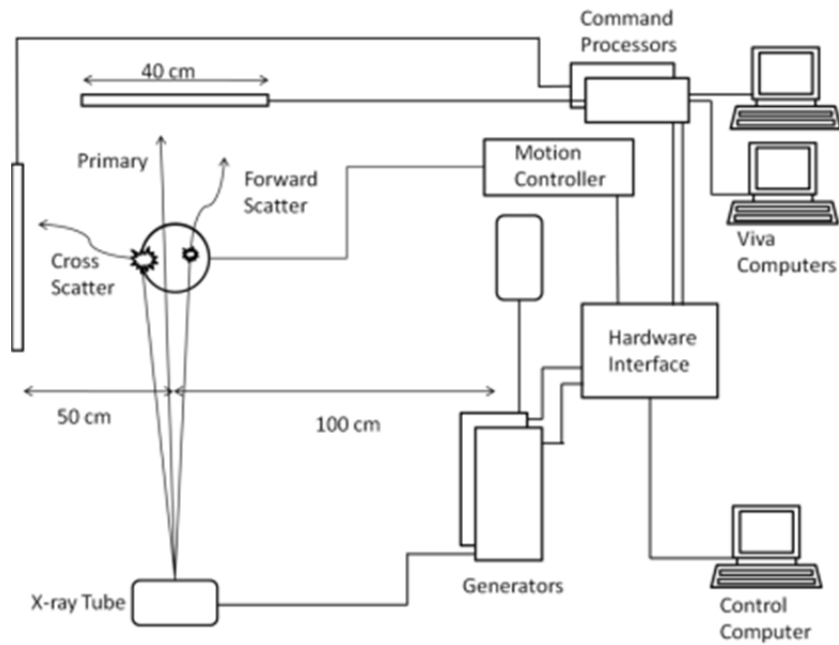


Figure 3.2: Schematic diagram of the dual X-ray system illustrating the geometry and origins of forward and cross scatter as well as the system control components.

3.1.1 Detectors

The dual X-ray system uses amorphous silicon detectors which are classified as indirect conversion detectors [24]. These detectors use a 2-dimensional array of photodiodes to capture light emitted by a cesium iodide scintillator [73]. Each pixel in the array contains a photodiode plus readout electronics. Figure 3.3 shows a cross sectional schematic of a generalized amorphous silicon detector.

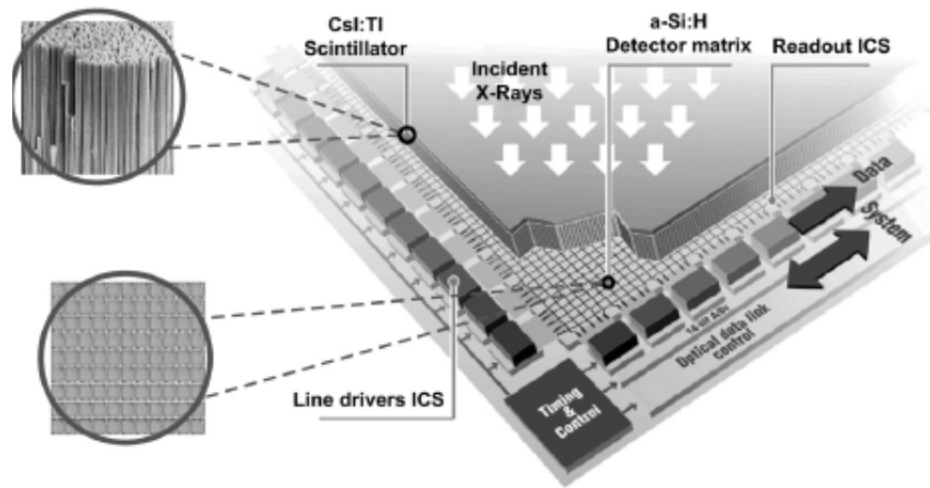


Figure 3.3: Cross sectional schematic of generic amorphous silicon detector. ICS is short for integrated circuits [24].

3.1.1.1 Detector Readout Cycle

The detectors operate in two modes: a readout mode and an integrate mode. The length of the readout mode is fixed depending on the binning selected by the user, the 4030CBs used in the dual X-ray system allow for 1x1, 2x2, and 2x1 binning. The length of the integrate mode is dependent on the user selected frame rate. The maximum detector frame rate is 30 frames per second (FPS) for 2x2 binning and 15 FPS for 1x1

binning. Integration mode is the longer of the two and is the time during which charge is collected on the capacitance of the photodiodes. This is also when it is appropriate to irradiate the detectors. [73]

After the buildup period (integrate mode) the detectors read out the charge on each pixel. The detector reads two lines of pixels and then moves on to the next starting from the top and bottom working towards the center as illustrated in Figure 3.4. Each line is read out one pixel at a time at approximately $40 \mu\text{s}$ a line. Each line contains 2048 pixels for 1x1 binning. [73]

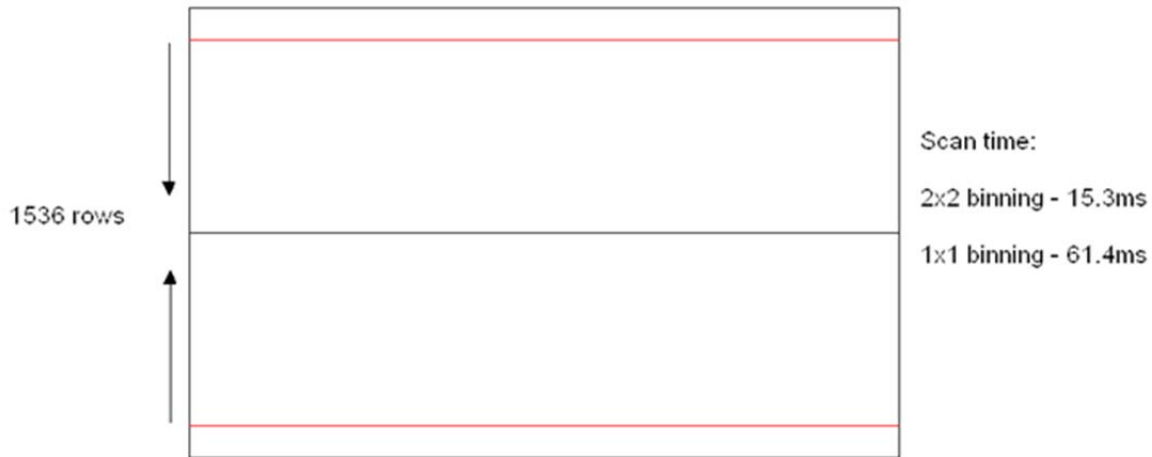


Figure 3.4: Diagram illustrating how the detector scans each line of pixels

3.1.1.2 Image Processing

Once the integrated charge has been read out it is transferred to the image processing unit via fiber optic cable. The image processing unit performs the vital task of correcting the raw data for inhomogeneities in the dark current of each pixel as well

as for intrinsic differences in the readout amplifiers, also known as offset and gain corrections. These corrections require that a flat field and a dark field image be taken, that is one with an unobstructed X-ray beam and one with no exposure. In practice, many (typically 128) flat and dark field images are used to reduce any error introduced by a single measurement. The algorithm for these corrections is given in Equation (3.1) courtesy of Varian. [73]

$$image_data = gain_median \times \left(\frac{raw_data - offset_data}{gain_data - offset_data} \right) \quad (3.1)$$

Once the data has been corrected in the image processing unit it is sent to a frame grabber mounted in a computer. During video acquisition Viva (Varian Image Viewer and Acquisition, the base software package accompanying the detectors) uses the frame grabber to capture every frame. Viva does not have the capability to allow outside triggering of the frame grabber or the beginning of acquisitions. All acquisitions must be started manually in the Viva software and since the frame grabber will grab every frame during video acquisition, large amounts of unwanted data are collected. [73]

3.1.1.3 Detector/System Interface

Like the other system components, the detectors have some capability to interface with the rest of the system and these interfaces manifest as digital input/output (I/O) signals. The most critical signals are named Expose_OK and User_sync. The Expose_OK signal, as its name suggests, is a signal that alerts the controller that it is safe

to expose the detector to radiation. This signal is high during the readout period of the detector which allows the controlling software to closely monitor the readout cycle of the detector. The second signal, User_sync, is an input to the detector. This rising edge of this signal can be used to define the beginning of the readout period and can therefore also define the frame rate of the detector. [73]

3.1.2 Generators and X-ray Tubes

The function of rotating anode X-ray tubes is well known and not critical to the design of the system. Understanding the generators that control and provide power to the X-ray tubes is vital to understanding the design of the system. The generators contain a circuit board dedicated to interfacing with other devices. This board contains terminals that allow various interlocks as well as triggering signals to be hardwired into the generator. [74]

The three signals that are vital to this project are remote exposure, remote prep, and remote fluoro. Early versions of the system utilized the remote prep signal to spin up the anode of the X-ray tube followed by the remote expose signal to request a radiographic exposure. There are limits designated by the manufacturer that prevent sustained, sequential use of radiographic exposures and so later versions transitioned to using only the remote fluoro signal. The generator was programmed to spin up the anode as well as initiate continuous X-rays when the remote fluoro signal was asserted. [74]

3.1.2.1 Programming the Generator

The generator can be programmed using the accompanying console, Figure 3.5. The user has the option to adjust the response to interface signals. Typically when a remote signal is being used the corresponding commands on the console itself are disabled. For example, the console cannot be used to initiate a fluoro exposure when the generator is programmed to respond to the remote fluoro input. The kVp and tube current are both set using the console. [74]



Figure 3.5: Generator console

3.1.2.2 Generator Hardware Interface

Each generator has 3 critical signals that are used to control the production of x-rays by the system software. The first one of these is the Remote_Fluoro signal. This allows a remote request for constant production of X-rays at a low tube current. (When this signal is true the generators will immediately start spinning the anode.) X-rays are

produced as long as requested. This signal is primarily used during detector calibration. [74]

The other two signals are used in conjunction with one another. The first is Remote_Prep which tells the generator when to spin the anode. The second signal is Remote_Expose which is used to request a predetermined X-ray exposure. Remote_Expose requires that Remote_Prep be active – the anode must be spinning for x-rays to be generated. X-ray production for Remote_Prep begins with the rising edge of the signal and the signal must remain true throughout the exposure to ensure consistent exposure times. [74]

3.1.3 Motion Controller and Rotational Stage

The rotation stage consists of three main parts: the motion controller, rotation stage (motor), and the table assembly. The table assembly, shown in Figure 3.6 is mounted on top of the rotation stage and is made of an aluminum base plate, a PVC spacer (three sizes), and a plastic table. The rotation stage is capable of rotating over 360 degrees in either direction and is controlled directly by the motion controller.

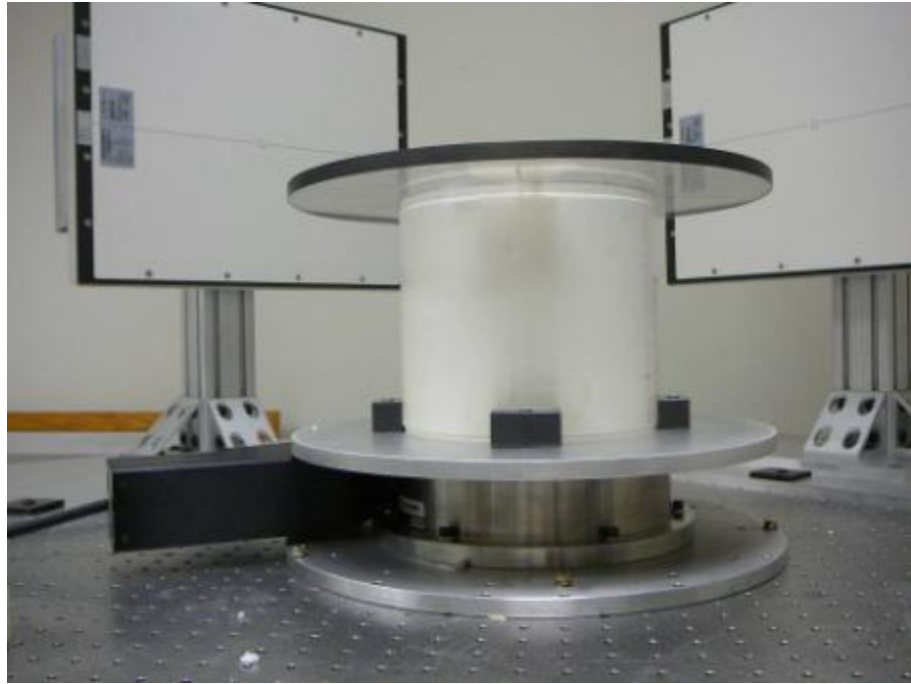


Figure 3.6: Rotation stage mounted on table with largest PVC spacer.

Newport's ESP300 motion controller is the most versatile device in the system in terms of communications and interfacing with other devices because it has the ability to be programmed. The programs have the ability to execute complex sequences of motion on up to three different motors (this system only requires one). The user can also program the controller to respond to inputs and define the use of its outputs. There are a total of 16 bits that can be used for inputs or outputs and these are further organized into two ports of 8 bits. Each port must be configured as either an input or an output (default is output) before it can be used by a program. [75]

3.2 Hardware Interface

3.2.1 Electrical Isolation

The detectors and generators both use optical isolation to protect their internal circuitry from circuits that are used to interface with other devices. Optical isolation may also be referred to as optocoupling or optoisolation. Figure 3.7 shows a generic form of an optoisolated circuit, the two circuits A and B have no direct electrical connections. Instead, a single binary signal can be sent between the two when A applies current in the proper direction causing light to be emitted by the LED. This in turn allows current to flow through the photodiode connected to circuit B. This also allows the two circuits to operate on different logic levels. [76]

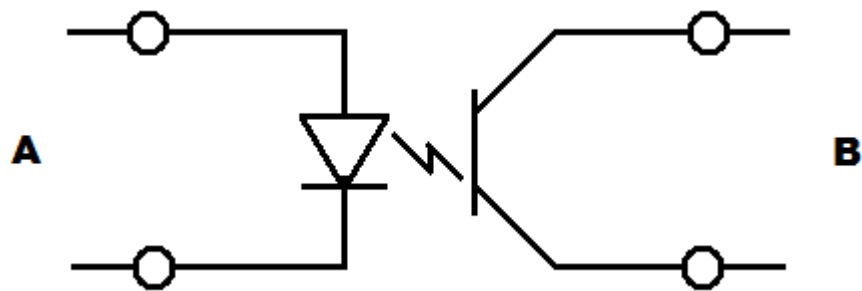


Figure 3.7: A simple circuit diagram illustrating the basic principle of optoisolation.

The detectors contain the optoisolators internally and connections are made at the terminals near A or B, depending on whether the signal transmitted through that circuit is an input or an output. [73]

While the detectors operate in the same manner as the example in Figure 3.7, the generator interface is slightly more complicated and is illustrated in Figure 3.8. The generator operates on a 24 volt logic level and the circuitry involved in the optoisolation has two possible configurations. One configuration is similar to that illustrated in Figure 3.7, however, the configuration shown in Figure 3.8 was chosen. This configuration was used because it does not require any outside power source; all that is required is that the two terminals corresponding to the input are simply jumped. This is easily accomplished with a relay which has the added benefit of adding another level of isolation between the extremely high voltages in the generator and the rest of the system. When the relay pictured in Figure 3.8 is activated and closed, current flows through the photodiode which then activates the phototransistor allowing current to flow through it and into the internal electronics of the generator. [74]

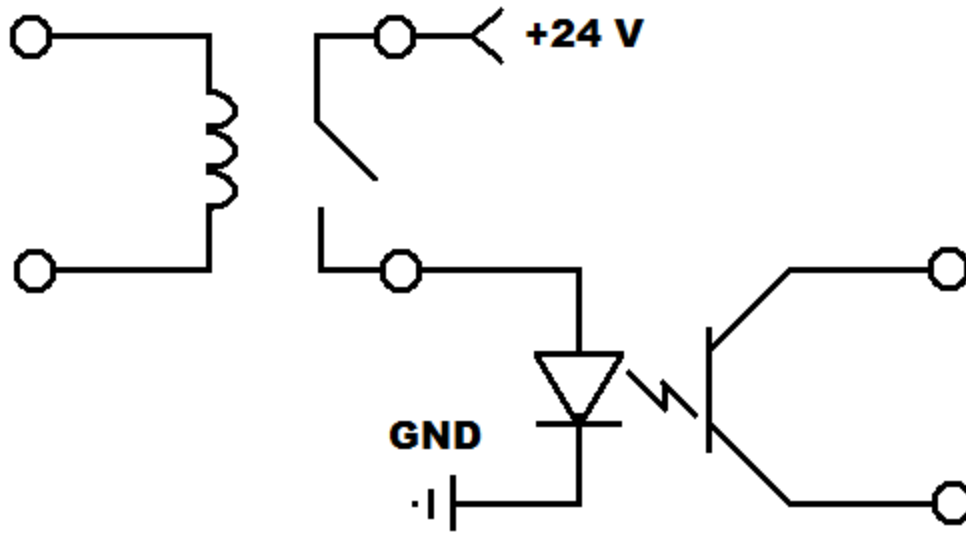


Figure 3.8: Simple diagram of relays used to trigger the optoisolated circuits within the generator room interface board.

3.2.2 Computer Interface

Ultimately, all components are controlled via computer. The computer I/O is handled by a National Instruments (Austin, TX) PCIe-6320 data acquisition card. The 6320 has 24 analog inputs, 24 bidirectional digital channels, and 4 digital counter/timer channels [77]. The counter/timer channels are hardware timed and can be programmed to generate pulses at frequencies up to 100 MHz with pulse widths as short as 10 ns [77]. These counter/timer channels are used to synchronize the frame rates of the detector (User_sync) and the exposures of the X-ray tube (Remote_Expose). The other digital channels are used for the other signals that do not require precise synchronization such

as Remote_Fluoro and Remote_Prep. Figure 3.9 is a schematic diagram of the electrical connections used in the control system of the dual X-ray system.

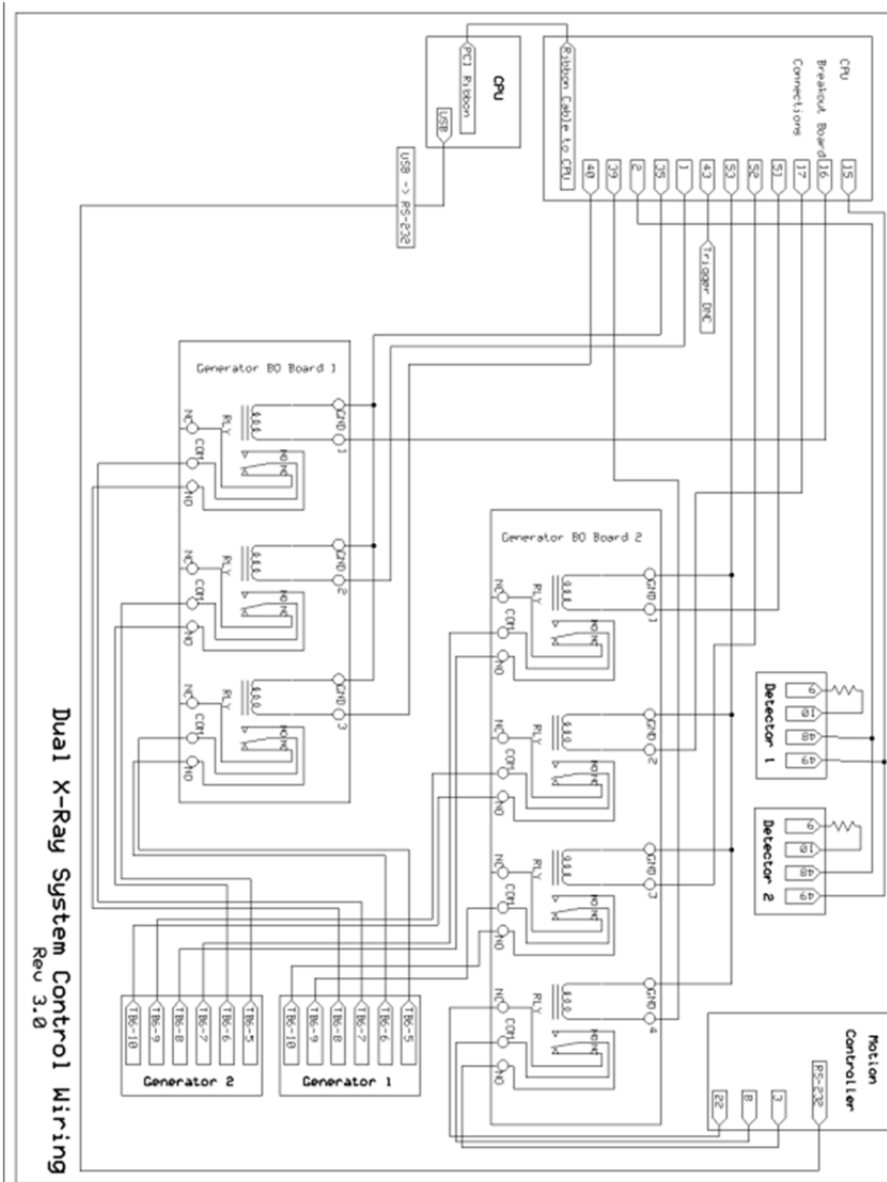


Figure 3.9: Schematic wiring diagram of the dual X-ray control system.

3.3 Software Control

The control software provides the user of the system with a means to customize the scanning parameters. The software allows for variable frame rate, variable rotation speed, and variable exposure timings. This is accomplished by defining and generating square waveforms which act as inputs for the interface circuitry of the system devices. The two detectors share a single output that defines the frame rate and synchronizes the detectors.

All waveforms rely on the hardware timing available in the PCIe-6320. This provides a much more reliable set of signals compared with software timed signals. Unlike software timed signals which are all generated with the CPU and then transmitted via the USB or serial ports, with hardware timed generation each waveform is generated on its own dedicated circuit.

3.3.1 Normal Scanning

There are two approaches used by the software for generating the waveforms that drive the system components. The first, and simplest, is for scans in which the both imaging chains will be utilized continuously across the entire scan angle. For this approach, the software generates four square waveforms: one for the detectors, one for each X-ray tube, and the fourth for the motion controller. All of the parameters that describe the waveforms are calculated and programmed into the timing circuits prior to the beginning of a scan. When the user is ready to scan the software generates a physical

trigger that triggers the beginning of all of the waveforms. This trigger ensures that the waveforms all begin at the same time and are in phase. Each waveform then runs, as described below, until completion and data acquisition is halted automatically with the cessation of the detector waveform.

The waveform for the motion controller serves only as a trigger to begin rotating. Having this signal hardware timed and synchronized to the other signals provides a high degree of reproducibility in the exact projection angles that are acquired. It is fully characterized by a single parameter that defines the wait time between the trigger that starts all of the waveforms and the beginning of rotation. The wait time is specified in an integer number of detector frames. Because the data acquisition software for the detectors (Viva) is self-contained and has no way of interfacing with the rest of the system, the user may specify a number of frames to wait before the rotation begins so that s/he may initialize data acquisition.

The detector waveform is described by two parameters, frame rate and high time of the signal. The signal high time is arbitrary as the detectors trigger off of the rising edge of the signal and is set to 10ms. The frame rate is set by the user. This waveform has no delay after the trigger. Because it defines the detector cycle, it is required for data acquisition. Therefore it must be active prior to the user initiating data acquisition in Viva.

At the time of writing, the X-ray generator waveforms required six inputs: frame rate, number of scrub frames (unexposed frames in between exposures), X-ray pulse length, wait time until rotation, rotation speed, and angular range of the scan. These parameters are used to calculate the frequency of the generator waveform, the start delay, and the high time of each pulse in the waveform. The frequency of the pulse train is given by Equation (3.2), where f_x is frequency of the X-ray generator waveform, f_d is the frequency of the detector cycle, and n_{scrub} is the number of scrub frames.

$$f_x = \frac{f_d}{1 + n_{scrub}} \quad (3.2)$$

The pulse width of the X-ray generator waveform is simply the length of the exposure in milliseconds plus an extra 10ms. The added length of the signal ensures that the generator has time to complete the requested exposure. The delay before the generator waveform begins is given by Equation (4.2), where D is the wait time until rotation, RO is the length of the detector readout period, T_{offset} is the time between the end of the detector readout and the beginning of the X-ray exposure, and T_x is a tube specific delay given by Equation (3.4). The expression (3.3) forces an offset between the exposures of the two X-ray tubes equal half the number of scrub frames (rounded up) to help distribution the exposures evenly about the scan angle.

$$d_x = D + RO + T_{offset} + T_x \quad (3.3)$$

$$T_x = \begin{cases} 0 & \text{if tube 1 or } n_{scrub} = 0 \\ \frac{1}{f_d} \times \left\lceil \frac{n_{scrub}}{2} \right\rceil & \text{tube 2} \end{cases} \quad (3.4)$$

Unlike the detector and motion controller waveforms, which have infinite lengths (in that they have no mathematically defined end), the waveforms for the generators have a specific number of pulses determined according to Equation (3.5). In Equation (3.5), θ_{max} and θ_{min} are the maximum and minimum rotation angles and v_{rot} is the rotation speed of the stage. This method of determining the number of pulses ignores the tube specific delay Equation (3.4) and therefore can cause tube 2 to fire one extra time at the end of a scan when scrub frames are present.

$$P_{num} = \frac{|\theta_{max} - \theta_{min}|}{v_{rot}} \frac{1}{\frac{1}{f_d}(1 + n_{scrub})} \quad (3.5)$$

3.3.2 Periodic Cross-Scatter Sampling

The second method for generating waveforms is designed to allow periodic measurements of the cross-scatter by only firing a single X-ray tube. For this method, the detector waveform remains unchanged; however, the generator and motion controller waveforms are much different. In addition to triggering the motion controller, the motion controller waveform is also used to trigger the generator waveforms in the cross-scatter sampling mode. In this section, it is referred to as the trigger waveform to more accurately describe its purpose.

The trigger waveform is now periodic (before it was a single pulse) and is triggered on the detector waveform. The trigger waveform has a delay equal to that of

the delay defined in Equation (3.3) when $T_x = 0$. The motion controller itself is still programmed to trigger on the rising edge of the first pulse and ignores any subsequent signals. There are $n_{sample} - 1$ pulses in the trigger waveform, where n_{sample} is the number of cross-scatter samples that will be taken during the scan. Each pulse in the waveform has a length equal to the time of one detector cycle (or frame). The frequency of the trigger waveform is given in Equation (3.6), where f_d is the frequency of the detector waveform. The number of pulses is given in Equation (3.6), where P_{num} is the number of pulses in the generator waveform calculated in Equation (3.5) when $n_{scrub} = 0$.

$$f_{mc} = f_d \frac{n_{sample} - 1}{P_{num}} \quad (3.6)$$

In the cross-scatter sampling mode, each generator waveform has the same number of pulses that trigger exposures as given in Equation (3.7). The generator waveforms trigger on the trigger waveform. Each rising edge triggers generator 1 and each falling edge triggers generator 2. The time between the rising and falling edge of the trigger signal is equal to the length of a single detector frame. This results in the generator waveforms being offset by exactly one detector frame.

$$P_{num}^{CS} = \left\lceil \frac{P_{num} - n_{sample}}{n_{sample}} \right\rceil \quad (3.7)$$

The offset between the generator waveforms forms the basis of the cross-scatter sampling technique. On the rising edge of the trigger waveform, the first generator waveform begins, which results in an exposure from tube 1 on that detector frame and

no corresponding exposure from tube 2. Generator waveform also ends one detector frame before generator waveform 2 which results in an exposure from tube 2 without a simultaneous exposure from tube 1. On the next frame, the trigger waveform will trigger the start of generator waveform 1 starting the process over again. This pulse sequence as described so far is represented in Figure 3.10 between the dashed lines.

In Figure 3.10, there is one pulse outside the dashed lines on each generator. These represent individual exposures that are requested by separate, temporary waveforms that the software generates before and after each scan so that the cross scatter can be sampled at the initial and final angle on each detector. The stage begins to rotate on the first rising edge of the trigger waveform and will always finish moving before the final exposure on generator 1 is taken. Occasionally, there will be an extra unexposed frame between the extra exposures (outside of the dashed lines) and the other acquisitions. This unexposed frame is caused by the lag created when the software has to clear the temporary waveform and generate the next one. It is possible that on high frame rates that there are multiple unexposed frames during this period.

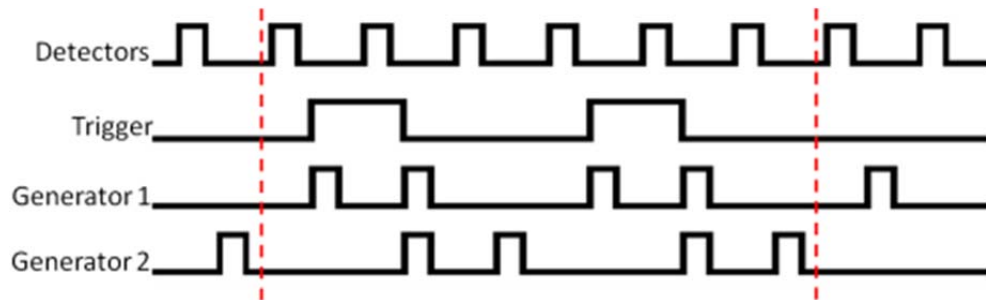


Figure 3.10: Schematic representation of cross scatter sampling pulse sequence.

3.4 Image Artifacts

The control system above was specifically designed to avoid certain artifacts that can be caused by improper control and synchronization of the X-ray system. Detailed descriptions of the artifacts and their causes can be found in *Timing and Communications for a Synchronous Dual X-ray System* [78]. Examples of these artifacts can be seen in Figure 3.11 and Figure 3.12.

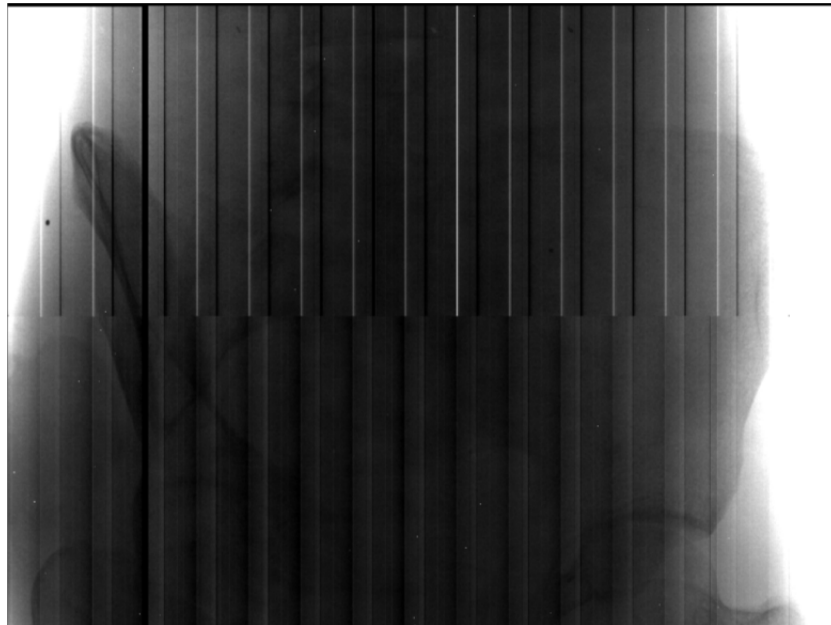


Figure 3.11: Artifacts caused by inconsistent User_Sync signal.

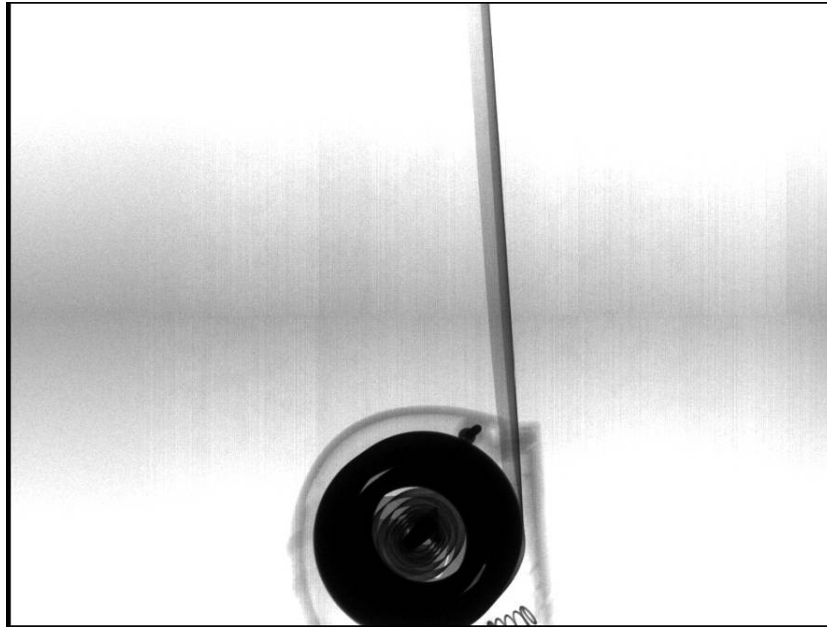


Figure 3.12: Stripe artifact caused by exposing during the readout period of the detector.

3.5 Future Directions

In addition to the investigations into cross scatter presented in later chapters, the dual X-ray system can be used to study several advanced applications of CBCT. Of particular interest to radiation therapy are techniques such as dual energy imaging, 4D CBCT, and 4D DTS.

4. Geometric Artifacts in CBCT

The findings presented in this chapter have been published in *Medical Physics* 38(4): 2116-21 March 2011.

4.1 Motivation

Some CBCT images include crescent artifacts, which are characterized by the dark and light bands shown in Figure 4.2. During the course of studying scatter in the dual X-ray imaging system similar artifacts (Figure 4.1) were observed while experimenting with different bowtie filters. The artifacts in Figure 4.1 were determined to be caused by a shift in the bowtie filter position between the acquisition of the blank scan and the acquisition of the projection data. Studying the cause of the artifact in the dual X-ray scanner gave rise to the hypothesis that the artifacts in the clinical scanners were also being caused by a mismatch of the actual bowtie filter position and the bowtie normalization.

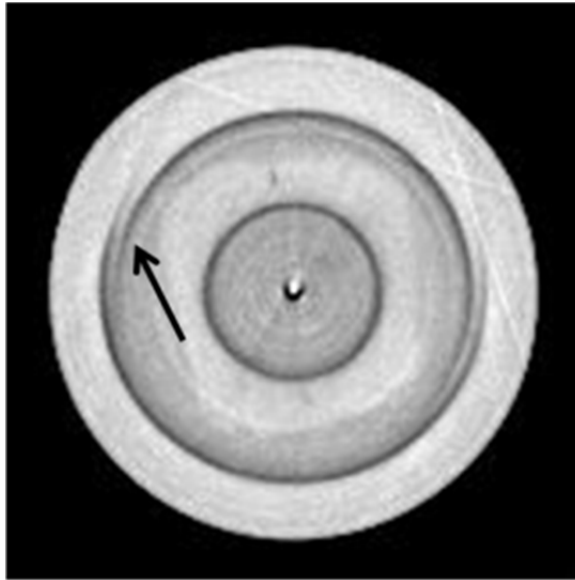


Figure 4.1: Imaging artifacts caused by shifts in a step-wedge style bowtie filter observed in the experimental dual X-ray imaging system.

For the geometry of a Varian Novalis Tx CBCT onboard imager (Varian Medical Systems, Palo Alto, CA), the bands of the crescent artifact trace out a circle with a diameter of approximately 15 cm. Such crescent artifacts have been noted in a study on CT number linearity [79], and the equipment manufacturer has commented on possible causes [80]. However, these studies were limited in their investigation into the artifact and further study was warranted.

Geometric calibration for CBCT scanners is vitally important, especially for gantry-mounted or C-arm systems. These systems have geometric calibrations that account for sag in the detector and focal spot and, in the case of gantry-mounted CBCT, align the CBCT isocenter with the linac isocenter. However, it is still possible that not all of the geometric parameters of a system are fully characterized by current calibration

procedures. In this chapter we examine the crescent artifact which is hypothesized to arise from a geometric error involving the location of the bowtie filter relative to the source and detector.

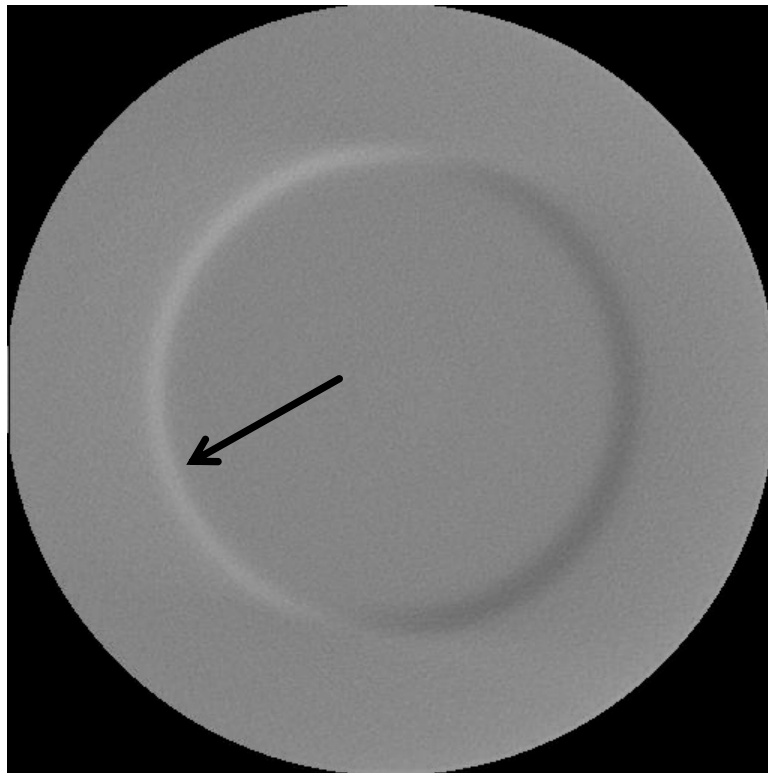


Figure 4.2: Reconstruction of a uniform phantom by the clinical reconstruction engine. The dark and light bands seen in this image of a uniform phantom are characteristic of the crescent artifacts in some clinical scanners.

Some bowtie filters have a steep gradient [40], such that small shifts in their position could result in large changes in the intensity across the detector. In an ideal system the bowtie filter is always in the same position relative to the focal spot and detector. However, in the case of gantry mounted CBCT systems, components are subjected to gravitational forces and may shift as the gantry rotates.

CBCT images are typically reconstructed using two sets of projection data: (i) blank projections in which no attenuating object is present between the detector and the X-ray-source system (including filters) and (ii) object projections, in which an object, such as a patient is present. CBCT image reconstructions generally utilize hundreds of different angles for the object projections, but may utilize only one angle for the blank projections. If the position of the bowtie filter, relative to the focal spot and detector, is angle-dependent, as suggested in the previous paragraph, then the single-angle blank projection will be inconsistent with the object projections. We investigate this inconsistency as a potential source of crescent artifacts, and we demonstrate artifact reduction through use of multiple angles of blank projections.

4.2 Methods

This chapter includes studies with computer-simulated and scanner-acquired data. The computer-simulation studies consider three deviations of the bowtie filter relative to the focal spot. These studies demonstrate that each deviation yields crescent artifacts similar to those observed in clinical CBCT images. The computer-simulation studies also gauge the magnitude of deviation that is required to produce clinically observed crescent artifacts. In the studies with scanner-acquired data, artifact severity is evaluated as a function of the number of projections in the blank scans.

Scanner data for all studies were acquired from a Novalis Tx treatment unit equipped with an onboard imager (Varian Medical Systems, Palo Alto, CA). A variety of

imaging protocols were available. In this study, the high quality head protocol (120 kVp, 2 mAs per projection, 200 degree scan angle) was used. This protocol requires the full-fan bowtie filter. It acquires approximately 380-390 projections over a 200-degree scan angle. The 200° range is always repeated, however, the exact number of projection angles acquired varies. Thus, there were a slightly different number of projections in the blank scan than in the object scan. The detector matrix was 2048x1536, and the raw data were acquired as a matrix of 1024x768 pixels, which were rebinned to 512x384 by the clinical system, as is standard for clinical scans using this protocol.

All image reconstructions were performed with an in-house implementation of the Feldkamp, Davis, and Kress (FDK) reconstruction algorithm [81].

4.2.1 Numerical Investigation into Mechanical Causes of the Artifact

Three deviations of the OBI geometry were modeled: (a) bowtie filter sag, in which the bowtie filter, shown in Figure 4.3, shifts tangentially (i.e. left/right in Figure 4.3) and the focal spot remains fixed in position relative to the detector, (b) X-ray tube sag, in which the bowtie filter and focal spot both shift tangentially relative to the detector while remaining in fixed configuration relative to one another, and (c) tube rotation, whereby the focal spot and bowtie filter rotate about an axis located behind the focal spot. In tube rotation (c), 1, 5, and 10 cm radii of rotation (ROR) were evaluated. The magnitudes of these deviations were set so as to match center-of-mass (COM) shifts

in the computer-simulated blank scans with COM shifts in scanner-acquired blank scans.

When measuring COM shifts in scanner-acquired blank scans, background trends were corrected prior to COM calculation. This correction was done by subtracting a low frequency fit to the projections of the flat regions of the bowtie filter.

To validate the COM measurements, a separate blank scan was performed with two tungsten wires (0.010 inches in diameter) fixed to the bowtie, one running down the trough and one perpendicular that spans the trough as seen in Figure 4.4. The Canny edge detection algorithm[82] was applied to each projection image to localize the edges of these wires. Then, the tangential (x -axis) displacements of the projection of the bowtie filter were calculated.

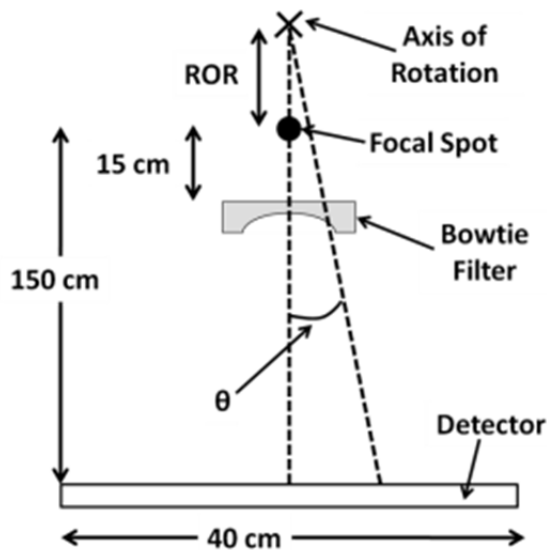


Figure 4.3: Geometry used for the simulation studies. For the tube-rotation simulations, the radius of rotation was set to 1, 5, and 10 cm behind the focal spot.

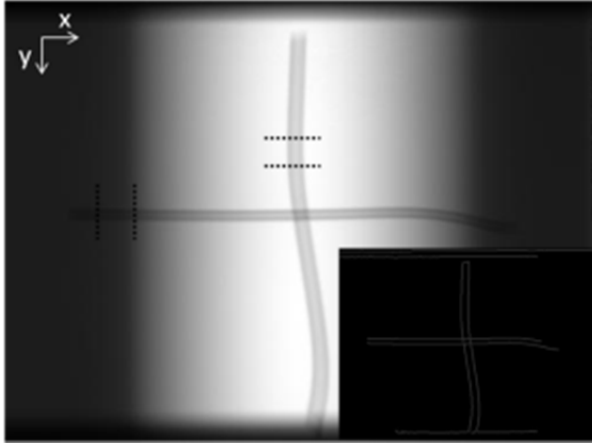


Figure 4.4: A projection of the bowtie filter with the tungsten wires in place. The dotted lines indicate the regions used to track changes in position as a function of angle. The thickness difference between wires is due to the different magnification factors in the trough of the bowtie filter versus at the top.

4.2.2 Clinical-Scanner Study of Artifact Reduction

For the scanner-acquired data, each projection was processed according to Equations (4.1) and (4.2), where $P(\theta)$ is the fully processed projection at projection angle θ , ready for FDK reconstruction, with processing specified by Equation (4.1). $\text{Proj}(\theta)$ is the projection through the phantom or patient with the bowtie filter in place at projection angle θ . $\text{Norm}(\theta_0)$ is a single projection through a uniform cylindrical calibration phantom. This projection combines a blank scan at angle θ_0 with a correction for the beam hardening caused by the varying thickness of the bowtie filter[83]. $\text{BT}(\theta)$ is the blank projection (including the bowtie filter) at angle θ . The factor $\text{Norm}(\theta)$ (Equation (4.2)) combines the beam-hardening correction with an angle-dependent blank scan. (In the simulation studies, $\text{Norm}(\theta_0)$ and $\text{BT}(\theta_0)$ were identical as the studies were done with a monochromatic beam and no beam hardening correction was

necessary.) The blank scan utilized with $\text{Proj}(\theta)$ was the one at the angle $\theta + \Delta\theta$ such that $|\Delta\theta|$ was a minimum, where $\Delta\theta$ specifies the angle, relative to θ , of each of the available blanks. As indicated before, for the scanner used in this study, the angular sampling was not exactly reproduced in different scans. Therefore, even if the number of blank projections matched the number of object projections, $\Delta\theta$ would rarely be zero.

$$P(\theta) = \frac{\text{Proj}(\theta)}{\text{Norm}(\theta)} \quad (4.1)$$

$$\text{Norm}(\theta) = \text{Norm}(\theta_0) \frac{\text{BT}(\theta + \Delta\theta)}{\text{BT}(\theta_0)} \quad (4.2)$$

Angle-dependent blanks were applied to two data sets: a patient scan and a uniform phantom scan. In this study, the blank scans were performed immediately following the scan of the phantom and the same day as the patient scan. Varying numbers of blank projections were utilized, ranging from 1 to 380, with approximately regular angular intervals. For the phantom study, root mean squared error (RMSE), as shown in Equation (4.3), was calculated in a ring-shaped region Ω encompassing the artifacts, as a function of number of blanks.

$$\text{RMSE} = \sqrt{\frac{1}{n_{\text{vox}}} \sum_{i=1}^{n_{\text{vox}}} (\text{Reconstruction}_i - \text{Ideal}_i)^2} \quad (4.3)$$

In Equation (4.3), n_{vox} is the number of image voxels in Ω and i is an index over voxels in Ω . Ideal_i is the amplitude at voxel i in the true phantom image. The phantom imaged in this study was the same phantom used to acquire $\text{Norm}(\theta_0)$. Therefore Ideal_i

in Equation (4.3) is zero for all voxels. Reconstruction_i is the amplitude at voxel i in the reconstructed image.

4.3 Results

4.3.1 Numerical Investigation into Mechanical Causes of the Artifact

The results of wire edge tracking and COM measurements are shown in Figure 4.5, indicating that the maximum shift was 3-4 mm relative to the first projection in the scan at a gantry angle of 0 degrees. This maximum occurred at a gantry angle of approximately 140 degrees in the system used in this study. There was good agreement, within 1 pixel, between the COM measures and the edge detection of the wires. The numerical simulation studies considered a maximum COM shift of 3.2 mm, corresponding to the COM result seen in Figure 4.5. The numerical simulations demonstrated that this shift could be recreated by a deviation of (a) 0.535 mm for bowtie filter sag or (b) 5.80 mm for X-ray tube sag. For (c) tube rotation with a 1-cm ROR, a rotation of 0.149° recreated the 3.2-mm shift, as did a 0.119° rotation with 5-cm ROR and a 0.096° rotation with 10-cm ROR.

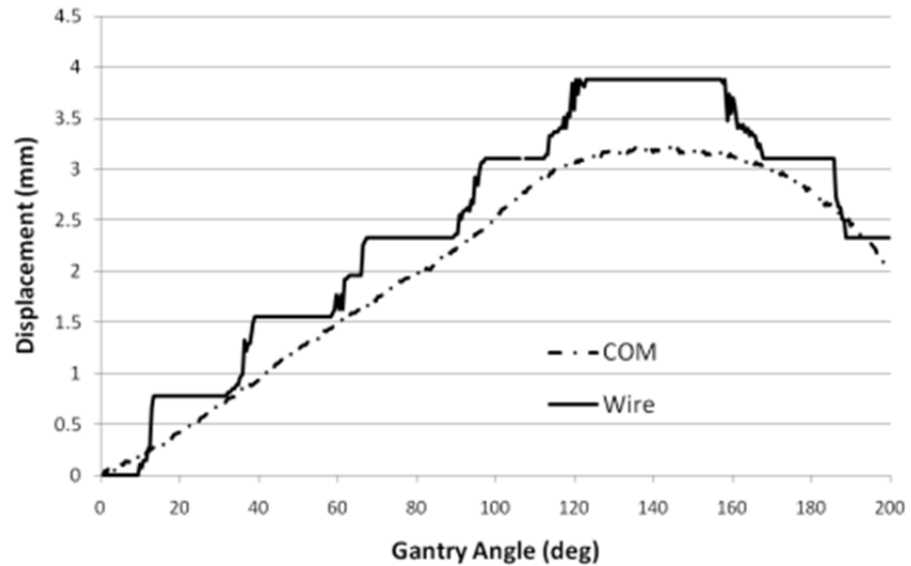


Figure 4.5: Plots of measured COM and wire shifts versus gantry angle.

Reconstructions of the simulated images are shown in Figure 4.6a-c. Each of the three idealized mechanical deviations caused crescent artifacts similar to those observed in the clinical scanner. Profiles through the centers of simulated images 5a and 5c are shown in Figure 4.6d. The profile for X-ray tube sag (b) is not shown because it is almost indistinguishable from the profile for bowtie filter sag (a). Likewise, only one profile is shown for the tube rotation cases (c) because these cases are largely indistinguishable from one another. Furthermore, the reconstructions resulting from mechanisms (a) and (b) differ from (c) primarily in that the artifact amplitude is greater for (a) and (b). Figure 4.7 depicts the relationship between the location of the crescent artifacts and the shape of the simulated bowtie filter as projected onto the central plane of the reconstruction space. The artifacts appeared in the regions of the highest gradient in the projections of the bowtie filter, and just inside of the flat portions of the bowtie filter. As the bowtie

filter shifted in one direction, the incident fluence was underestimated on one side and overestimated on the other. This caused the attenuation in the corresponding voxels, as calculated by the reconstruction, to be higher or lower than it actually was. The end result was one light and one dark crescent shape in the reconstructed image.

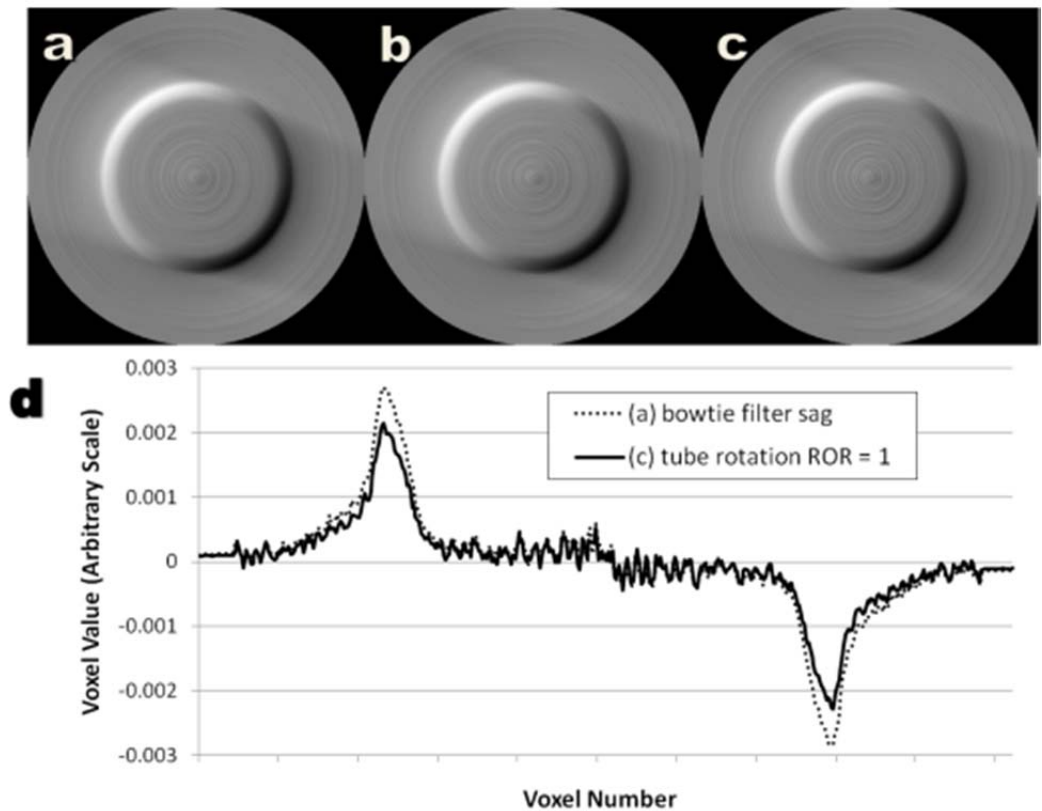


Figure 4.6: Reconstructions of blank scans by the in-house implementation of FDK resulting from (a) simulated bowtie filter sag, (b) simulated X-ray tube sag, and (c) simulated tube rotation with ROR = 1 cm. (d) Horizontal profiles through the center of the reconstructions in (a) and (c).

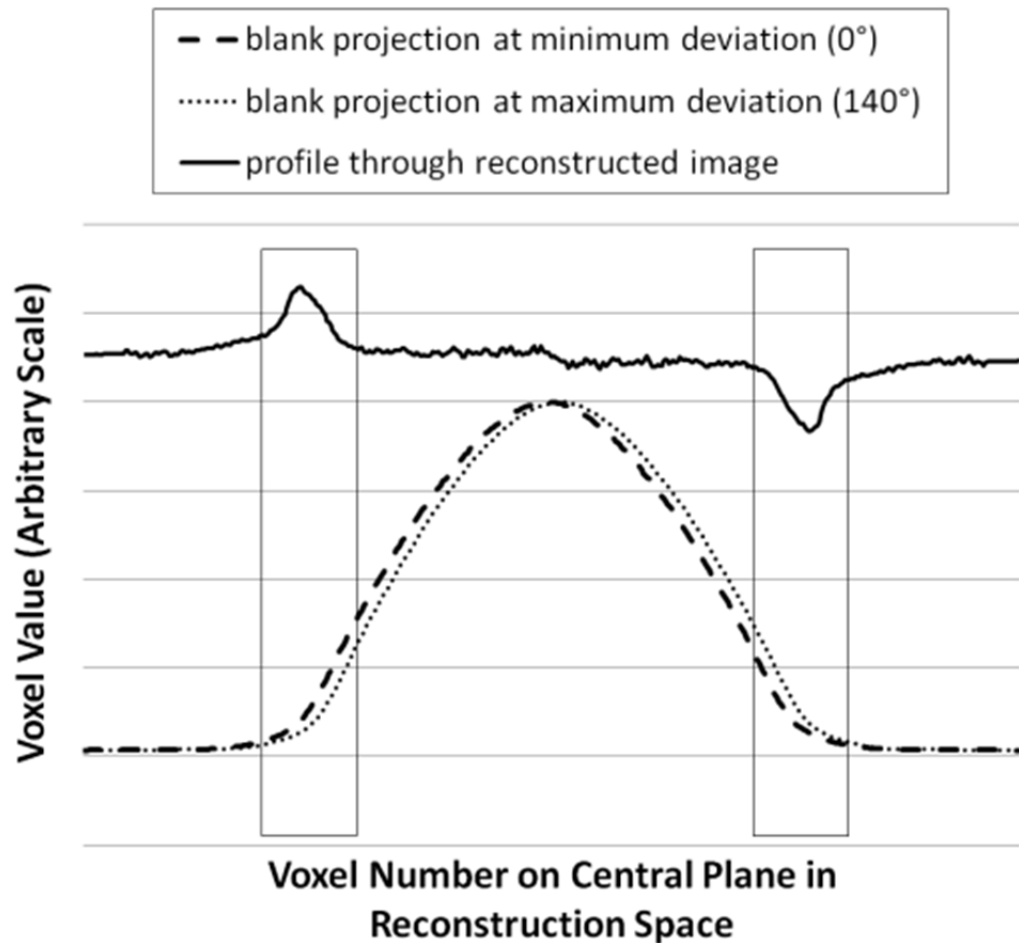


Figure 4.7: Profiles through the center of the reconstructed image (solid line) and through blank projections (dashed and dotted lines). The profiles through blank projections are scaled to the width they would have if the projection plane passed through the center of the image space. The two blank-projection profiles (dashed and dotted lines) indicate the minimum and maximum bowtie shifts, which occur at projection angles of 0° and 140° . The boxes indicate the location of the artifact relative to the shapes of the blank projection profiles.

4.3.2 Clinical-Scanner Study of Artifact Reduction

Figure 4.8a-c show reconstructed images of uniform phantom data acquired with the clinical scanner using the in-house implementation of the FDK algorithm. The 3

images correspond to 3 different numbers of blank scans, 1, 175, and 380. Figure 4.8d is a plot of calculated RMSE results for different numbers of blank projections ranging in small steps from 1 to 380. As the number of blank projections increased, the RMSE was level below about 40 blank projections. There was a dramatic reduction in RMSE as the number of blank scans became larger than 100. The RMSE reduced from 8.91×10^{-4} to 5.25×10^{-7} from 1 to 380 blank projections over a 200 degree scan angle.

The effect of blank-projection number on the crescent artifacts can also be seen in Figure 4.9. Figure 4.9a shows an image reconstructed from patient data using a single blank projection. The crescent artifact in this image can be seen as a bright crescent through the center of the head. The image in Figure 8b was reconstructed from the same projection data but utilizing 380 blanks, and the artifact is no longer visible. The crescent artifact is clearly visible in Figure 4.9c which shows the subtraction of Figure 4.9a and Figure 4.9b. The corresponding profiles in Figure 4.9d indicate that the primary differences between Figure 4.9a and Figure 4.9b are in the vicinity of the crescent artifact.

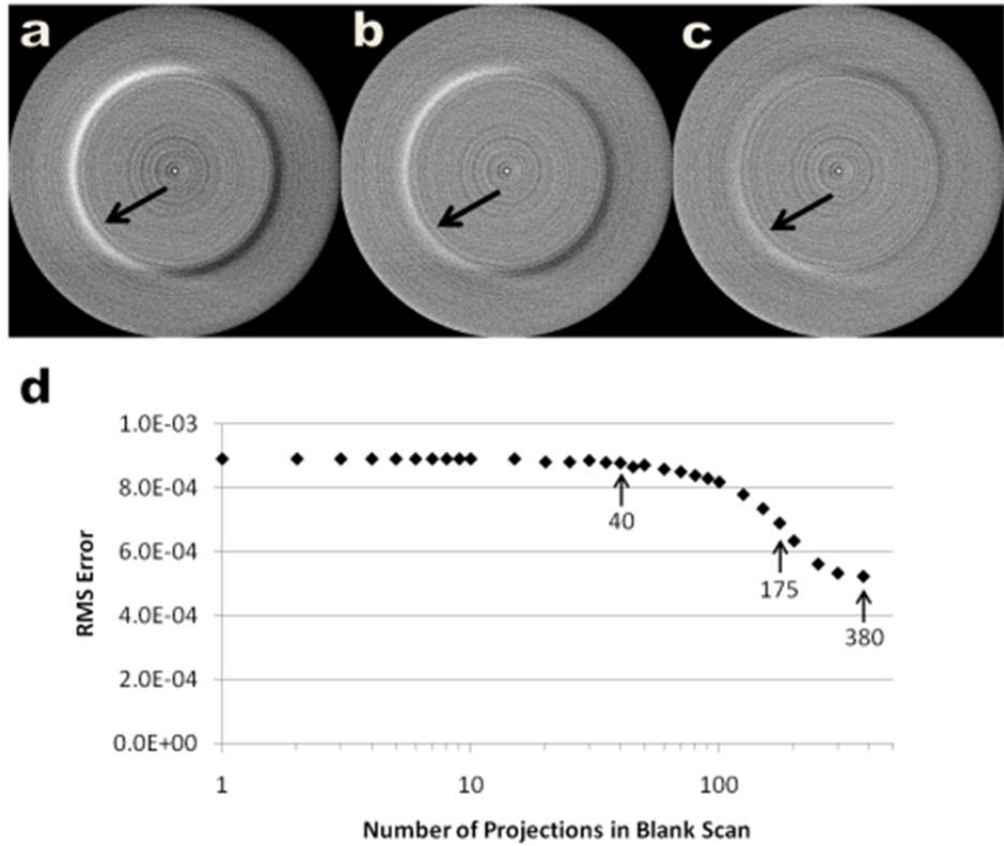


Figure 4.8: In-house FDK reconstructions of a uniform phantom utilizing (a) 1 blank, (b) 175 blanks, and (c) 380 blanks. (d) The RMS error in reconstructions using a variable number of projections in the blank scan. The range plotted represents reconstructing with 1 to 380 blanks over a 200 degree scan angle. Data points for 40, 175, and 380 blanks are identified by the 3 labeled arrows.

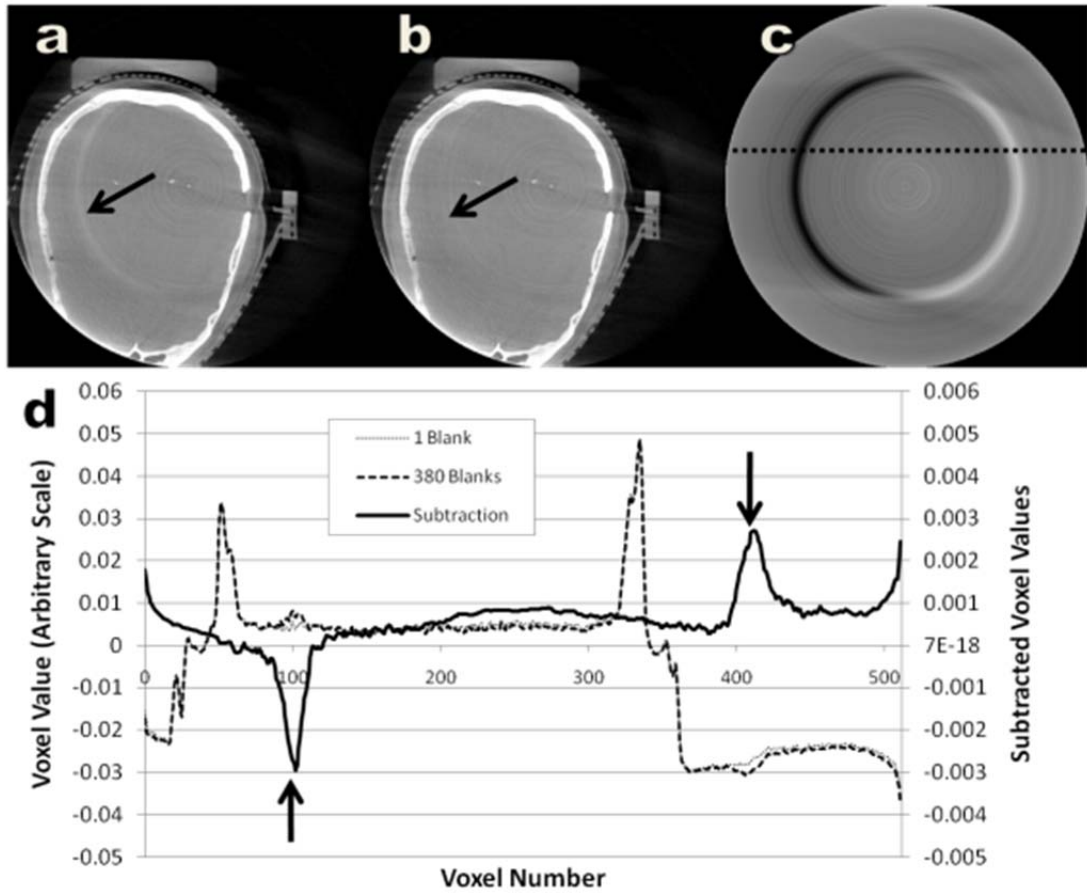


Figure 4.9: Patient images reconstructed with the in-house implementation of FDK using (a) a single blank and (b) 380 blanks. (c) The subtraction of fig 8a. and fig 8b. The dashed line indicates where the profiles (d) were taken. The arrows in (d) indicate where the crescent artifacts are located.

4.4 Discussion

The three mechanical deviations examined in this study were chosen because they result in movement along the direction of the bowtie filter gradient. Such movements are shown here to result in under- and over-estimation of incident photon intensities, which are in turn shown to result in crescent artifacts. Other degrees of

freedom exist that are perpendicular to the bowtie gradient; however, these motions were not investigated in this study and would involve different mis-estimations than considered here. The studies here do not identify which of the three motions is occurring in the particular commercial scanner utilized in these studies. Conversely, the studies do show that any of these three deviations could result in crescent artifacts in many various present or future commercial or research CBCT systems. Furthermore, the studies here characterize the magnitudes of deviation required in all three cases to produce crescent artifacts.

The COM measurements – which were used to set the amplitude of each of the three types of deviation – weight the central regions of the bowtie filter more heavily than the outer regions, whereas the artifact is influenced primarily by the outer portions of the bowtie filter profile (Figure 4.7). This may be associated with the differences in artifact magnitude, observed in Figure 4.6, for the translational mechanisms (a,b) versus the rotational mechanism (c).

These studies have shown that crescent artifacts can be mitigated by the use of angle-dependent blanks. The commercial scanner utilized for this paper does not precisely recreate the same specific acquisition angles on any two scans. Thus with 380 blank angles and 380 object projections, discrepancies between object projection angle and nearest blank projection angle were as great as 0.25 degrees. Figure 4.5, however, shows that deviations vary smoothly with angle, for the scanner considered. Given such

smooth variations, artifact reduction can still be effective even with some discrepancies between blank and object projection angles.

4.5 Conclusion

The crescent artifacts observed on some commercial OBI systems can be explained by (a) slight motions of the bowtie filter relative to the detector and focal spot, or by (b,c) motions of the bowtie filter and focal spot together, relative to the detector. The magnitudes of these deviations can be small. Such crescent artifacts can be greatly alleviated by use of angle-dependent blank scans.

5. Magnitude and Avoidance of Cross-Scatter Effects in Dual CBCT

The findings presented in this paper have been submitted for publication in *Medical Physics*, a peer-reviewed journal, and are currently under review.

5.1 Motivation

Cross-scatter effects have been studied in dual-source CT [69-72]. However, even though we were not the first to construct a dual-cone system with flat-panel imagers [55-57], cross scatter has not been extensively studied or characterized in a dual-conebeam x-ray imaging system. Herein, we investigate the magnitude and effects of cross scatter in dual-cone X-ray imaging system and a method for avoiding the cross-scatter is proposed and evaluated.

5.2 Methods

5.2.1 Acquisition Sequences

When the two detectors are synchronized, there are three general categories of acquisition sequence: (a) the simultaneous case in which there is one rotation and both X-ray tubes expose each frame, (b) the interleaved case in which there is one rotation and each tube fires on alternating detector frames, and (c) the sequential case where one tube fires on each frame for one rotation and the other tube for the next rotation. For the purposes of this study, we propose the interleaved acquisition (b) as an avoidance strategy to reduce cross scatter effects in dual-CBCT imaging. The sequential acquisition

(c) represents the gold standard, cross-scatter-free scenario. The three acquisition sequences are illustrated in Figure 5.1a-c. The rotation speed of the stage was halved in the interleaved acquisition sequence to maintain the same number of projections and approximately the same angular sampling as the other two acquisitions. Using the methods described in the next section, the effects of scatter on reconstructed images were studied for these three acquisition sequences.

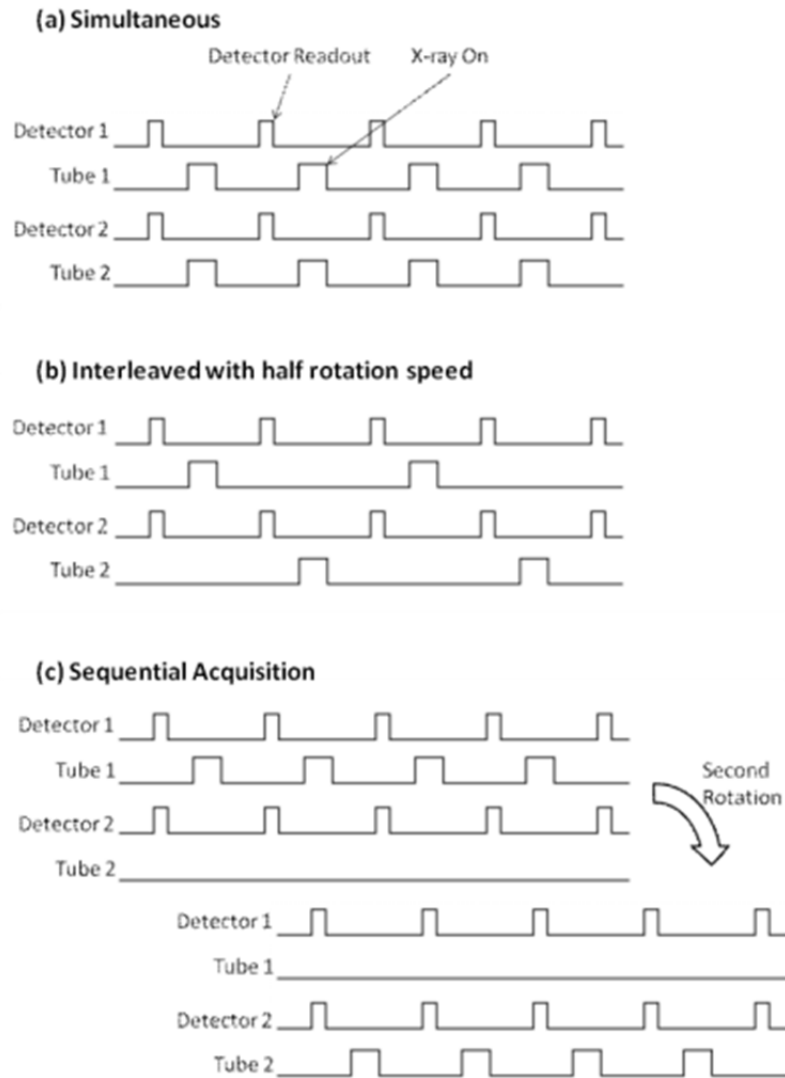


Figure 5.1: Schematic representations of three projection acquisition sequences: (a) simultaneous, (b) interleaved, and (c) sequential.

5.2.2 Phantoms

Object size was varied using a Catphan® 400 cylindrical image quality phantom.

This phantom consists of a containing cylinder that is 20cm in outer diameter, with a 2.5cm thick wall. A small phantom – with outer diameter of 15cm – was obtained by

removing the containing cylinder and utilizing only the inner portion of the Catphan. A larger phantom was obtained by submerging the Catphan in a roughly cylindrical water-filled 5-gallon bucket that was approximately 30cm in diameter. This provided three phantoms of varying diameter – 15cm, 20cm, and 30cm – with identical internal structure in the inner 15cm region, including contrast plugs approximately 12.3mm in diameter. Table 5.1 lists the material in each plug as well as its nominal HU and electron density as provided by the manufacturer for the CTP404 insert [84].

Table 5.1: Material and nominal CT number for each plug in the Catphan core.

ROI #	Material	Nominal HU	Electron Density (10^{23} e/g)
1	Air	-1000	3.007
2	Polystyrene	-35	3.238
3	LDPE	-100	3.429
4	PMP	-200	3.435
5	Air	-1000	3.007
6	Teflon	990	2.889
7	Delrin	340	3.209

5.2.3 Imaging Technique

As kVp was varied, mAs per projection was also varied in order to prevent detector saturation in shine-by regions as well as during the acquisition of blank scans used to normalize the projection data to account for the shape of the bowtie filter. Table 5.2 lists the nominal values of kVp, tube current, and exposure time used in this study.

Table 5.2: Exposure parameters used for all studies in this chapter.

Tube Voltage (kVp)	Tube Current (mA)	Exposure Time (ms)	mAs per Projection (mAs)
70	80	25	2
85	80	25	2
100	63	25	1.575
115	40	25	1
130	32	20	0.64
145	32	16	0.512

5.2.4 Measurements of Forward Scatter in Projections

Cross-scatter (CS) distributions were measured by firing a single X-ray tube and acquiring data on the orthogonal detector. Forward-scatter (FS) distributions were estimated using a beam stop array (BSA) [85, 86]. The BSA consisted of lead cylinders 3mm in diameter and 3mm long embedded into a 3mm-thick Lucite sheet on a 25.4mm (1 inch) grid. The BSA was positioned parallel to the detector plane, upstream from, but as close as possible to, the phantom (65cm from the focal spot), to maximize the number of lead cylinders in the beam. Each of the lead plugs was approximately 10 half-value layers at 150 kVp [87]. Thus, it was assumed that any signal detected behind the lead beam stops can only be attributed to scatter. Further, if only a single X-ray tube is firing, then the signal behind the lead beam stops is only forward scatter. The distribution of forward scatter across the image was then estimated by bilinear interpolation between the values measured behind the BSA. To reduce the noise, a final estimate of FS was obtained as the average of 10 measurements. The distribution T of total detected signal,

which includes CS, FS, and signal from non-scattered photons, was also obtained by averaging 10 measurements.

5.2.5 Image Reconstruction

For the three acquisition sequences described above – (a) simultaneous, (b) interleaved, and (c) sequential – 554 projections per detector were acquired evenly spaced over 360° , giving a total of 1108 projections over 360° . For each sequence all three phantoms were imaged with the six techniques indicated in Table 2. Image reconstruction was performed using an in-house implementation of the Feldkamp algorithm[81].

Conversion to Hounsfield units (HU) was performed by generating a lookup table between the reconstructed voxel values and the nominal HU value (Table 1) for the 20cm phantom at each energy in a fan beam geometry. The fan beam geometry was achieved by narrowing the collimators down to an axial beam width of 2.56cm at the axis of rotation.

5.2.6 Quantitative Analysis of Scatter in Projections

Scalar analogs to CS, FS, and T were computed by averaging these distributions over a 10 by 10 pixels (3.88mm) square ROI, i , in the center of the detector, giving CS_i , FS_i , and T_i . These ratios are defined such that they always represent the case in which both X-ray tubes are firing even if individual terms are measured when a single X-ray tube is firing.

Scatter to primary ratio (SPR_i), Equation (5.1), is a widely employed metric for reporting the scatter contribution in CBCT projections [43, 85, 88]. Herein, we also define forward-scatter fraction (FSF_i), Equation (5.2), and cross-scatter fraction (CSF_i), Equation (5.3), to differentiate the relative contributions, to the total signal, of the two sources of scatter, the primary and orthogonal X-ray tubes. Cross-scatter to primary ratio ($CSPR_i$), Equation (5.4), and forward-scatter to primary ratio ($FSPR_i$), Equation (5.5) constitute two components of SPR_i . Finally, cross-scatter to forward-scatter ratio is defined in Equation (5.6).

$$SPR_i = \frac{CS_i + FS_i}{T_i - FS_i - CS_i} \quad (5.1)$$

$$FSF_i = \frac{FS_i}{T_i} \quad (5.2)$$

$$CSF_i = \frac{CS_i}{T_i} \quad (5.3)$$

$$CSPR_i = \frac{CS_i}{T_i - FS_i - CS_i} \quad (5.4)$$

$$FSPR_i = \frac{FS_i}{T_i - FS_i - CS_i} \quad (5.5)$$

$$CFR_i = \frac{CS_i}{FS_i} \quad (5.6)$$

The quantity $T_i - CS_i$ in Equation (5.1) represents the total non-cross-scatter signal in one detector and was measured by firing one tube without the BSA in place. The scatter fractions defined in Equations (5.1-6) were measured as a function of object size and kVp. The ratios of CS_i , FS_i , and $(T_i - FS_i - CS_i)$ to I_0 are also calculated, where I_0 is

the intensity in the same ROI, i , of a projection with no phantom present. For simplicity, the subscript i will be dropped in subsequent references to these scalar quantities. Each fraction or ratio in Equations (5.1-6) was calculated 20 times with unique measurements (10 times on each detector). The reported values are the average of the 20 calculations and error is reported as the standard deviation of those 20 calculations.

5.2.7 Quantitative Analysis of Scatter in Reconstructions

For reconstructed images of the 20cm phantom, the three acquisition sequences were compared via profiles. In addition, 7.8mm-diameter ROIs (shown in solid circles in Figure 5.2) were placed on the 7 plugs, and 12 background ROIs of the same diameter (dashed circles in Figure 5.2) were placed at the same radius in the phantom. The following metrics were evaluated for each plug and each acquisition method as a function of phantom diameter and kVp: contrast (C), relative noise (N), and contrast-to-noise ratio (CNR), Equations (5.7-9) respectively. In Equations (5.7-9), μ is the mean voxel value in the ROI region or background (BG) regions, and σ_{BG} is the standard deviation of pixel values in the background. Note that μ_{BG} and Equation (4.8) are independent of the particular plug under consideration.

$$C = |\mu_{ROI} - \mu_{BG}| \quad (5.7)$$

$$N = \sigma_{BG} \quad (5.8)$$

$$CNR = \frac{|\mu_{ROI} - \mu_{BG}|}{\sigma_{BG}} \quad (5.9)$$

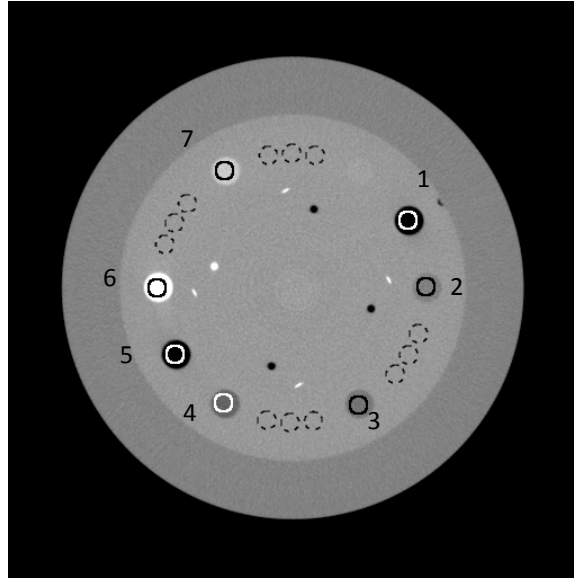


Figure 5.2: Reconstructed slice of the Catphan showing the ROIs of varying contrast. The solid circles indicate the ROI regions in Equations (5.7-9) while the dashed circles indicate the pixels used as the background (BG) regions in Equations (5.7-9).

5.3 Results

5.3.1 Projection Effects

Figure 5.3 shows plots of the cross scatter and forward scatter projection distributions for the 20 cm phantom. The top row shows the cross scatter distribution as measured on the detector. The bottom row shows the same distributions, but normalized by the initial intensity, and is heavily influenced by the shape of the bowtie filter. The cross-scatter distribution is sloped heavily in the transaxial direction, decreasing with distance from the X-ray tube that generated the primary photons. The

cross-scatter distribution is also sloped in the axial direction, peaking in the center of the detector. In contrast, forward scatter is symmetrically distributed both transaxially and axially about the phantom center.

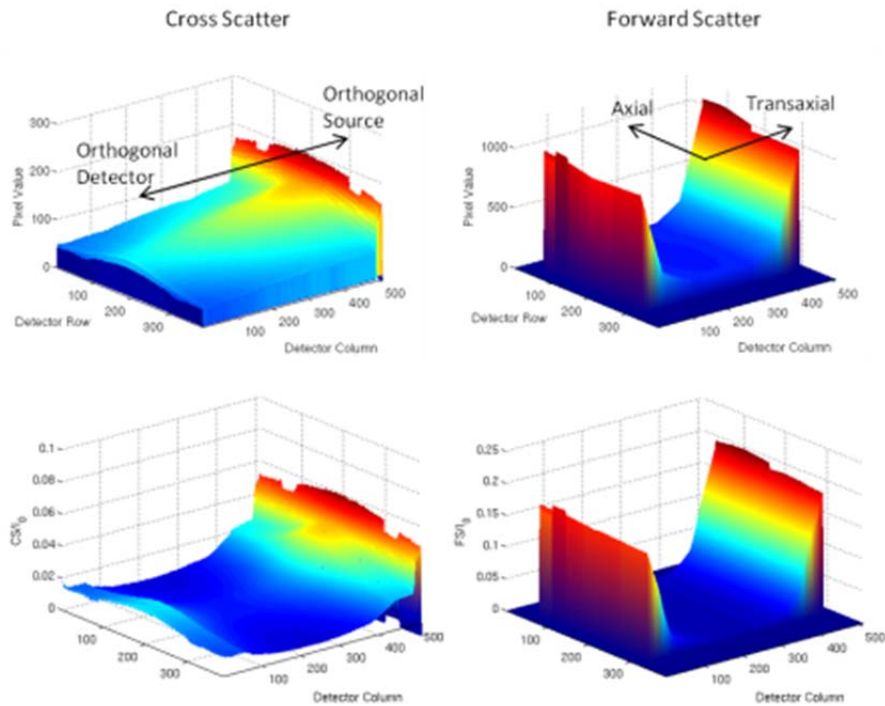


Figure 5.3: Plots of CS (left) and FS (right) for the 20 cm phantom. The CS is heavily sloped in the transaxial direction, increasing towards the orthogonal source. It also shows a peak in the axial direction in the center of the detector. This differs from FS which is symmetric in the axial and transaxial directions.

Figure 5.4a shows an average of 10 projections taken of the 20cm-diameter Catphan® with the beam stop array in place. The associated cross scatter distribution, acquired with the orthogonally positioned detector, also an average of 10 frames, is shown in Figure 5.4b. Results of the forward scatter estimation are shown in Figure 5.4c.

Transaxial profiles through Figure 5.4a-c, taken along the arrow in Figure 5.4a, are shown in Figure 5.4d. The profiles further illustrate the monotonically decreasing cross-scatter shape versus the transaxial symmetry of forward scatter.

The bright band seen on the left side of Figure 5.4b is thought to be caused by scattered photons that enter the detector beyond the edge of the anti-scatter grid. This band structure is not visible when the anti-scatter grid is not in place.

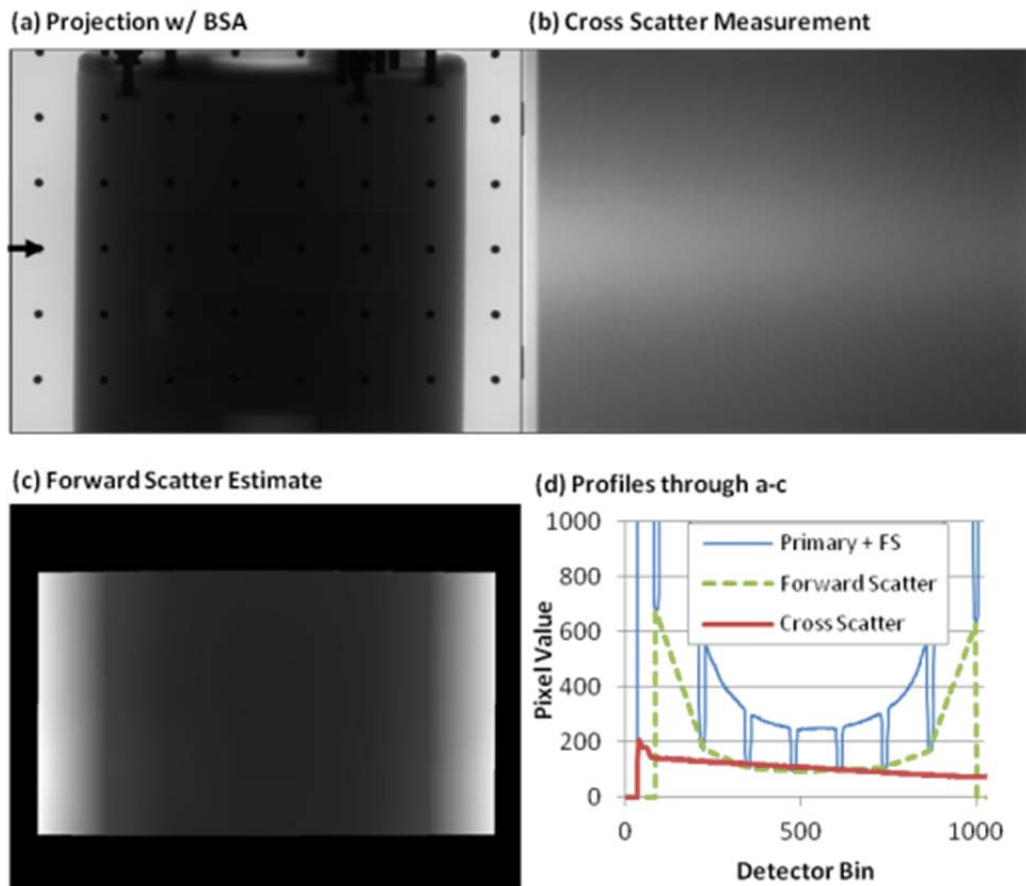


Figure 5.4: (a) Projection of the Catphan® at 100kVp, with BSA in place, and taken with Tube/Detector 1, without firing Tube 2. (b) The cross scatter as imaged by Detector 2 during the projection in Figure 5.4a. (c) The forward scatter component estimated from the projection in Figure 5.4a. (d) Horizontal profiles taken through

Figure 5.4a-c at the position indicated by the arrow in Figure 5.4a. The left side of the cross scatter profile is closest to the orthogonal detector.

Figure 5.5a plots the forward scatter fraction (FSF) as a function of kVp; for all three phantoms the FSF increases slightly with kVp. The FSF also decreases with phantom size. Conversely, Figure 5.5b shows that the CSF increases greatly with phantom size. CSF shows a much stronger dependence on object size than FSF. CSF varies slightly with kVp, but the direction of this variation depends on phantom size, decreasing with kVp for larger phantoms and increasing with kVp for smaller phantoms. As kVp increases, forward scatter, cross scatter, and total scatter all increase relative to the primary signal (SPRs in Figure 5.5c-e). The SPR of the 30cm phantom results predominantly from large cross scatter contributions; e.g. the CSF is 0.59 and 0.57 at 70 and 145 kVp respectively. The CFR (Figure 5.5f) of the 15cm phantom remains fairly constant with kVp; while the CFR of the 30cm phantom reduces strongly with kVp.

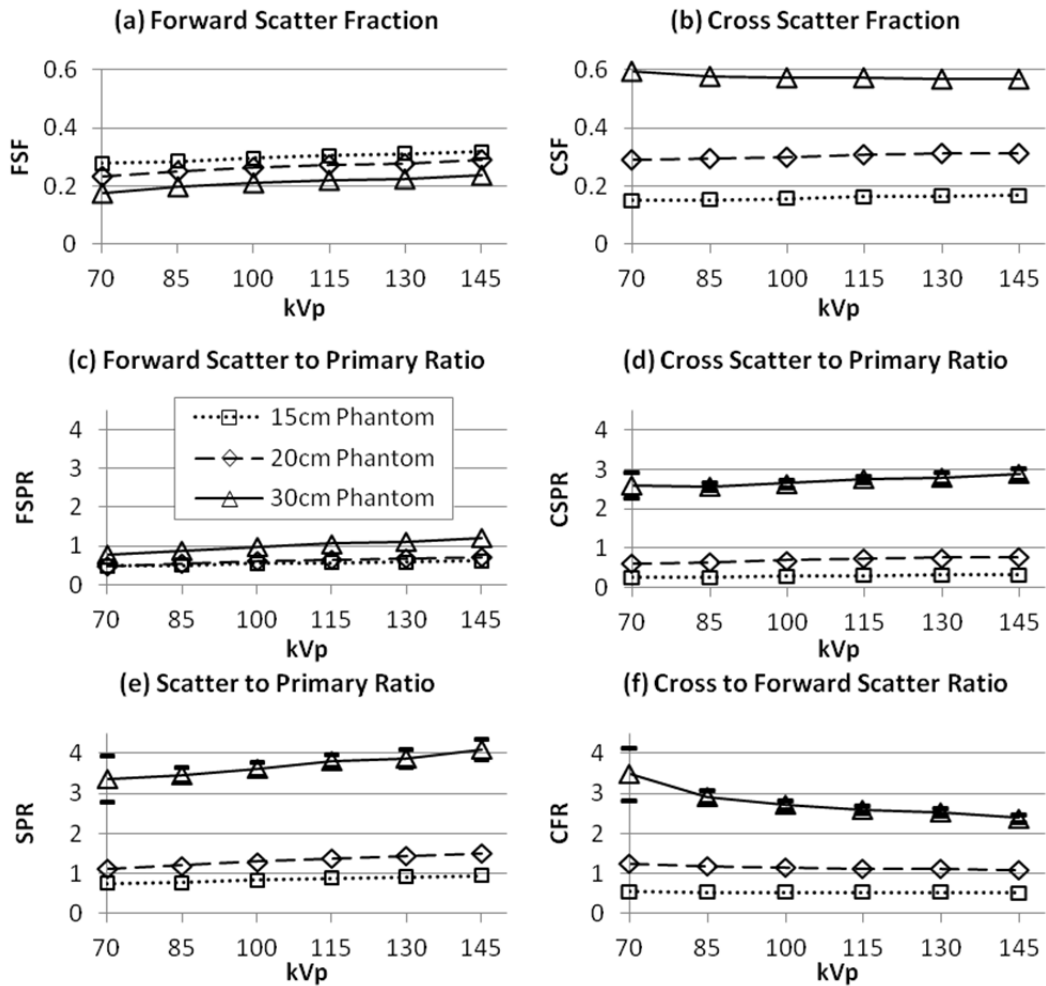


Figure 5.5: (a) Forward Scatter Fraction as a function of kVp. (b) Cross Scatter Fraction as a function of kVp. (c) Forward Scatter to Primary Ratio. (d) Cross Scatter to Primary Ratio. (e) Scatter to Primary Ratio. (f) Cross Scatter to Forward Scatter Ratio. Error bars are only shown for series when the bars are larger than the data markers.

Figure 5.6 shows the cross scatter, forward scatter, and primary transmission for the 15cm and 30cm phantoms for each value of kVp. All of these factors increase with kVp; however, cross scatter is the only one that does not decrease with object size. For all three phantoms (20cm is not shown) the plots of CS/I_0 overlay one another. This implies that, for the phantoms studied, the cross-scatter was independent of the object size. This

behavior is much different than forward scatter, which decreases as a function of object size.

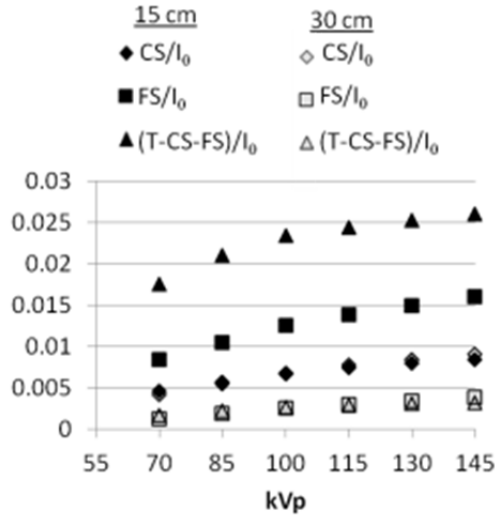


Figure 5.6: Plots of CS, FS, and primary transmission (T-CS-FS) all normalized to the initial intensity I_0 . The cross scatter (CS) normalized to the initial intensity is independent of phantom size. This suggests that the large changes seen in the cross-scatter fractions and scatter-to-primary ratios observed in Figure 5.5 are driven largely by changes in the primary transmission and forward scatter.

5.3.2 Reconstruction Effects

Figure 5.7a-c show reconstructed slices of the 20cm phantom at 100 kVp displayed at the same window and level. Figure 5.7d show profiles through these images. The reconstruction in Figure 5.7a is visibly darker than the indistinguishable reconstructions in Figure 5.7b and Figure 5.7c. This effect is also seen in the profiles in Figure 5.7d. In addition, the profiles show better contrast for sequential and interleaved acquisition as compared to simultaneous acquisition although the simultaneous case appears to have less noise. The noise (N) as given in Eq. 8 was measured to be 14.9 HU,

18.6 HU, and 17.7 HU for the (a) simultaneous, (b) interleaved, and (c) sequential reconstructions shown in Figure 5.7.

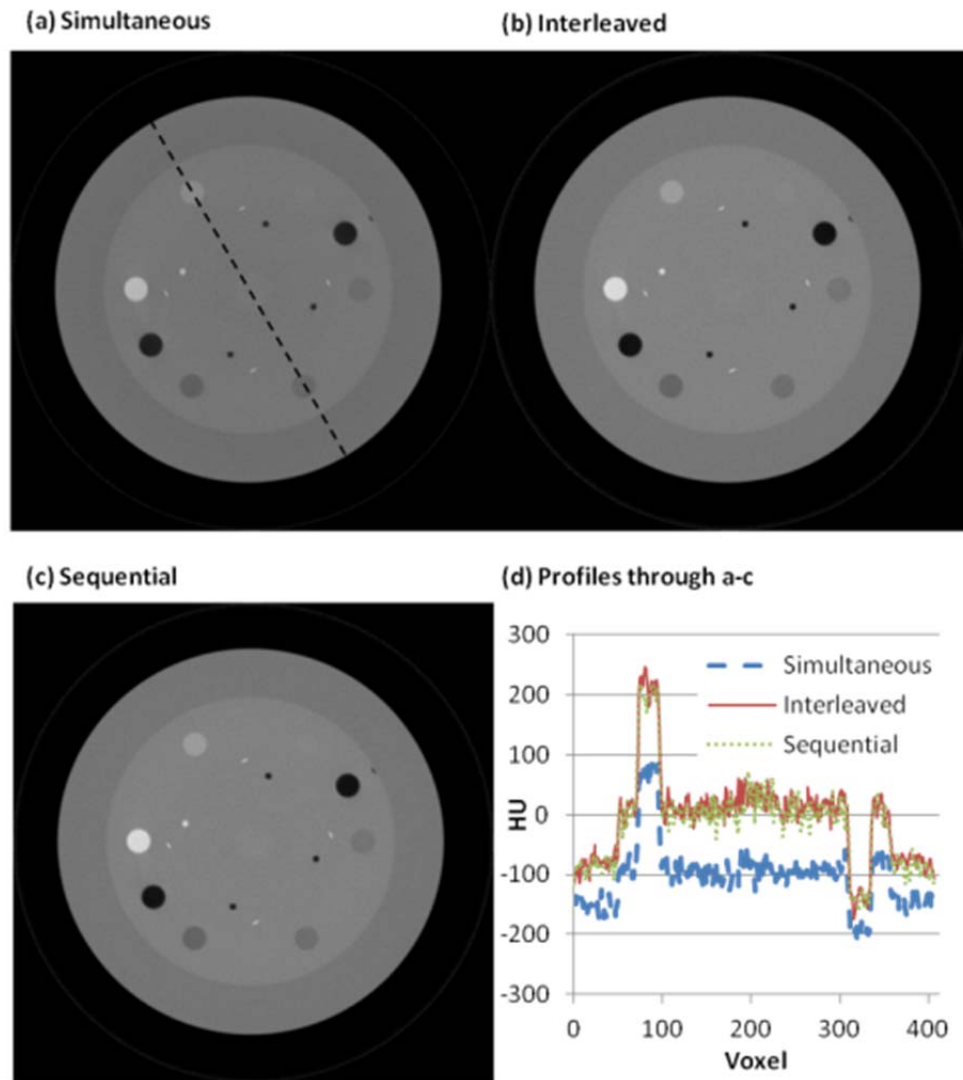


Figure 5.7: Reconstructed slices of the 20cm phantom at 100 kVp for acquisition protocols: (a) simultaneous, (b) interleaved, and (c) sequential. The window for the reconstructions is [-1000, 1000] and the level is 0 HU. (d) Profiles through each image along the dashed line in (a). The interleaved and sequential reconstructions have the same contrast. The reduction in contrast in the simultaneous reconstruction seen in the profiles manifests as a visibly darker image in Figure 5.7a.

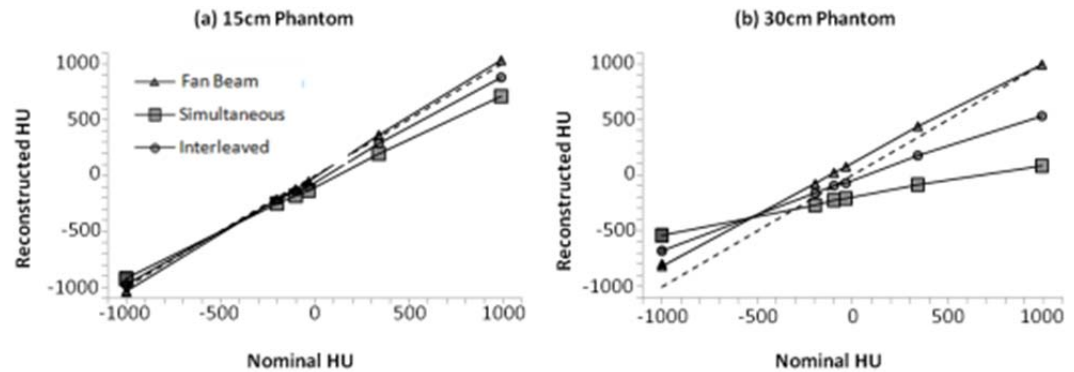


Figure 5.8: Plots of the reconstructed HU values for each ROI vs. the nominal HU values are shown for the (a) 15cm and (b) 30cm phantoms. The dashed line indicates the identity line where the reconstructed HU is equal to the nominal HU. The sequential acquisitions are not shown because they directly overlap the interleaved acquisitions.

The differences in HU caused by the presence of forward scatter and cross scatter can be seen in Figure 5.8. In both phantoms scatter pushes the reconstructed HU towards a single value regardless of the nominal value of the HU in the ROI, i.e. higher scatter corresponds to a more nearly horizontal line for reconstructed HU versus nominal HU. This effect is larger for the larger phantom which also has the greater SPR.

The simultaneous acquisition showed reduced contrast (C) in every phantom size for every kVp (see Figure 5.9a-b for 15cm and 30cm phantoms) compared to the sequential and interleaved acquisition modes, which had approximately equal contrast. Figure 5.9b shows the contrast for ROI 1 in the 15cm and 30cm phantoms for each kVp; here, the contrast reductions associated with simultaneous acquisition were more severe with increased phantom size. The sequential and interleaved acquisitions also showed approximately the same CNR in each ROI (Figure 5.9c) and for every kVp (Figure 5.9d).

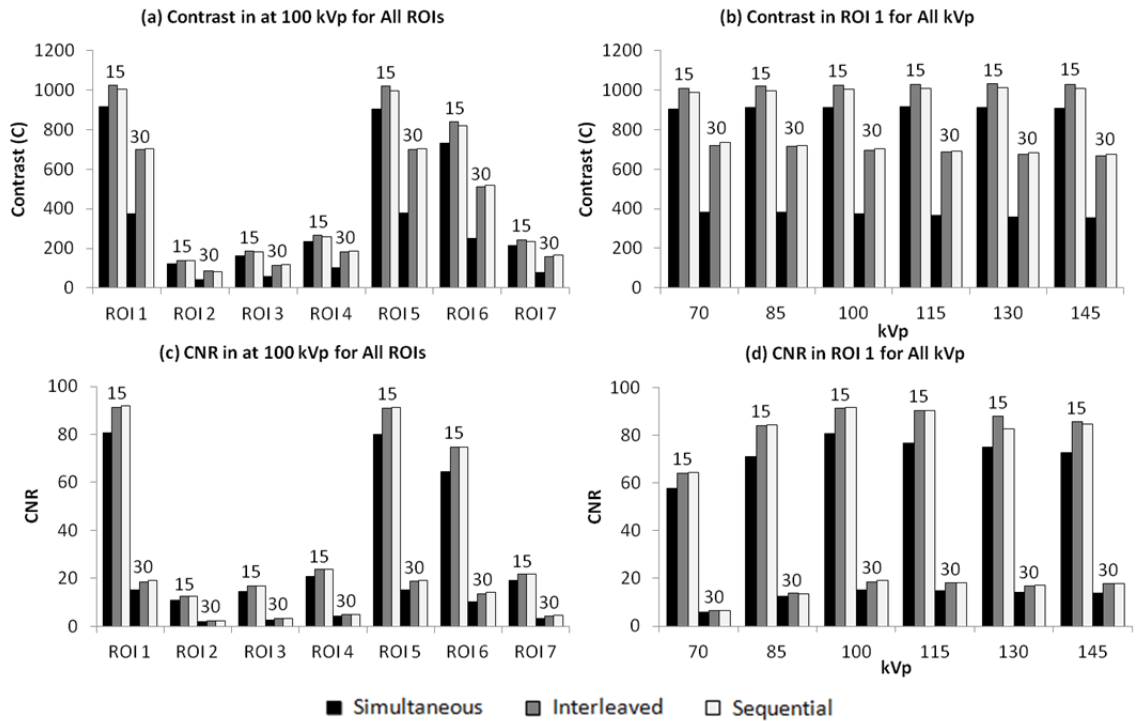


Figure 5.9: The numbers above each group of three acquisitions indicate the diameter of the phantom used for those measurements. (a) Contrast in all ROIs at 100 kVp. (b) Contrast in ROI 1 at all kVps. (c) CNR in all ROIs at 100 kVp. (d) CNR in ROI 1 for all kVps. Both contrast (C) and CNR are approximately the same for the sequential and interleaved acquisitions. However, the simultaneous acquisition shows a decrease in contrast and CNR compared with the other two acquisitions. Data for the 20cm phantom are not displayed here, but follows the same trends.

5.4 Discussion

Herein the magnitude and distribution of cross scatter are characterized for a dual cone-beam X-ray imaging system. The shape of the cross scatter distribution in the transaxial direction in dual CBCT is qualitatively similar to those reported by Kyriakou [71] and Engel [70] for dual source CT in that the cross scatter distribution is peaked towards the orthogonal X-ray source. Also investigated herein were scatter distributions in the axial direction, and it was found that, with the anti-scatter grid in place, the axial

cross-scatter distributions showed a peak at the detector center. Consequently, for a phantom where the primary signal is uniform in the axial direction, it may be that cross scatter degrades contrast and noise more severely in the central slices than in superior and inferior slices. In contrast, the forward scatter distribution was flat in the axial direction. In the transaxial direction, forward scatter was minimal at the center and peaked peripherally. These axial and transaxial shapes for forward scatter reflect the symmetries of a cylindrical phantom.

It was found that the CSF increases rapidly with object size. As object size increases, primary transmission and forward scatter decrease (Figure 7), however, the cross scatter remains constant. While cross-scatter becomes the dominate source of signal with increasing phantom size, this is mainly caused by reductions in the primary transmission and forward scatter intensity.

In reconstructed images, contrast and CNR are both degraded in the presence of cross scattered radiation which is consistent with the findings of Engel [70] and Kyriakou [71]. The presence of forward scatter pushed the reconstructed HU values towards a single value and reduced the contrast in reconstructed images (Figure 5.8). This effect was even stronger for cross scatter. Further, the HU inaccuracies increased with increasing object size. This result may change when different shape phantoms are used. For a cylindrical phantom in which the ROIs were placed at the same radius, the scatter affects each ROI equally. Engel et al. [70] have shown that in dual-source CT the

proximal periphery is the primary source of detected cross scatter events. Thus, for a non-cylindrical phantom, the cross-scatter intensity – like the primary transmission and forward scatter intensity – could change as the source rotates about the object. This could lead to non-uniform scatter effects.

The interleaved and sequential acquisitions were shown to have in general the best contrast and CNR performance. This is because, unlike the simultaneous acquisition, they do not use projections acquired when both tubes are firing in the same detector frame. The sequential technique is not practical since it requires two rotations and only uses a single tube/detector pair per scan. It was studied to provide the most cross-scatter-free case while maintaining other experimental parameters such as the noise and response characteristics of the detectors and the spectral composition of the X-ray tubes. The proposed interleaved acquisition is more practical in that it utilizes both X-ray chains in a single rotation. The rotation speed was halved for the interleaved case while detector frame rate was held constant to maintain the same experimental conditions, *i.e.* angular and temporal projection density and detector gain calibration, as the other acquisitions. This reduces the scan time benefits of the dual-source configuration. Rotation speed also plays a large role in some 4D CBCT techniques which may benefit from a dual-source technique [68]. However, even in the implementation presented here, the dual-cone system using interleaved technique with reduction in rotation speed has comparable scan time with single-cone system because the dual-cone

system only has to rotate 110° while the single-cone system must rotate 200° for complete sampling.

In principle, interleaved acquisition is not as cross-scatter free as sequential acquisition because of factors such as detector lag [27]. Charge trapping and scintillator afterglow are two effects that contribute to image lag; however, it is believed that charge trapping is the dominant source of lag effects for amorphous silicon flat panel imagers such as the ones used in this study [26, 89]. Unlike scintillator afterglow which decays with time, charge trapping effects decay with the number of readout cycles; of which there is exactly one per detector frame under normal operation. Therefore, lag effects are largely independent of frame rate [89].

The proposed interleaved acquisition avoids cross-scatter exposures during projection acquisition which not only mitigates the effects of the cross-scatter distribution (which can be addressed using cross scatter correction methods [90]), but also mitigates the effects of the stochastic components of the cross-scatter distribution. Herein it was found that interleaved acquisition provided contrast and CNR performance similar to the gold-standard but impractical sequential case.

5.5 Conclusions

Cross scatter in dual cone-beam X-ray imaging can be up to 3.4 times the magnitude of forward scatter. Cross scatter can greatly reduce contrast in reconstructed images and, in large phantoms, cross scatter is a larger contrast degrading factor than

forward scatter. The interleaved acquisition is an effective method for reducing the impact of cross scatter and has been shown to provide contrast and CNR comparable to scans where no cross scatter is present.

6. Deterministic Cross Scatter Correction

6.1 Motivation

The interleaved acquisition discussed in the previous chapter showed strong reduction of cross scatter effects in CBCT. That method of reducing cross-scatter effects has several draw-backs which may limit its benefits in some applications. First, the projection acquisition rate is immediately reduced by a factor of two; which when gantry rotation speed and frame rate are held constant reduces the angular density of acquired projections, which leads to a reduction in spatial resolution. If the gantry rotation speed is decreased, the total time it takes to scan the patient has not been improved by the addition of a second imaging chain and is actually slightly increased. Increasing the detector frame rate obviously requires a detector that can operate at that speed and an increase of at least a factor of two is required. An increase of the frame rate may also increase the magnitude of some lag effects. Finally, the use of interleaved acquisitions removes the ability of the dual-cone system to acquire simultaneous orthogonal views. The impact that any of these factors has on the clinical usefulness of the resulting images depends on the specific imaging task. Imaging protocols such as simultaneous orthogonal DTS and 4D CBCT may suffer from some of these effects of the interleaved acquisition. Thus, it is important to develop alternate methods for addressing the effects of cross-scatter.

6.2 Correction Strategy Overview

The correction strategy is comprised of two main steps: a subtraction in projection space to correct the low-frequency, deterministic component and a subtraction in Fourier space to correct the high-frequency, stochastic component of cross scatter. For both components, estimates of the cross scatter must be obtained. To this end, we propose to sample the cross scatter distribution intermittently throughout the scan as shown in Figure 6.1. This is accomplished by skipping the exposure from one X-ray tube for a single projection which allows that tube's corresponding detector to make a direct measurement of the cross scatter distribution at that angle.

This method is similar in principle to many forward-scatter estimation methods that rely on beam stop arrays or other methods of blocking the primary beam to estimate scatter at different points on the detector and to Ning's method of sampling the forward scatter distribution at sparse angular intervals [46]. Like these methods, the proposed correction relies on the assumption that the scatter distribution is slowly varying along the dimensions of interpolation. It differs from these methods in that it does not use a beam stop array or similar hardware to estimate the scatter at discrete points across the detector, but instead measures the cross scatter on the whole detector. Measuring the scatter across the entire detector provides information on the entire spectrum of the scatter distribution across the detector face and not just the lower frequencies that are obtained using a beam stop array.

This chapter discusses the correction for the deterministic component of the cross scatter and the sampling interval required to perform that portion of the correction accurately. The stochastic correction is detailed in the next chapter.

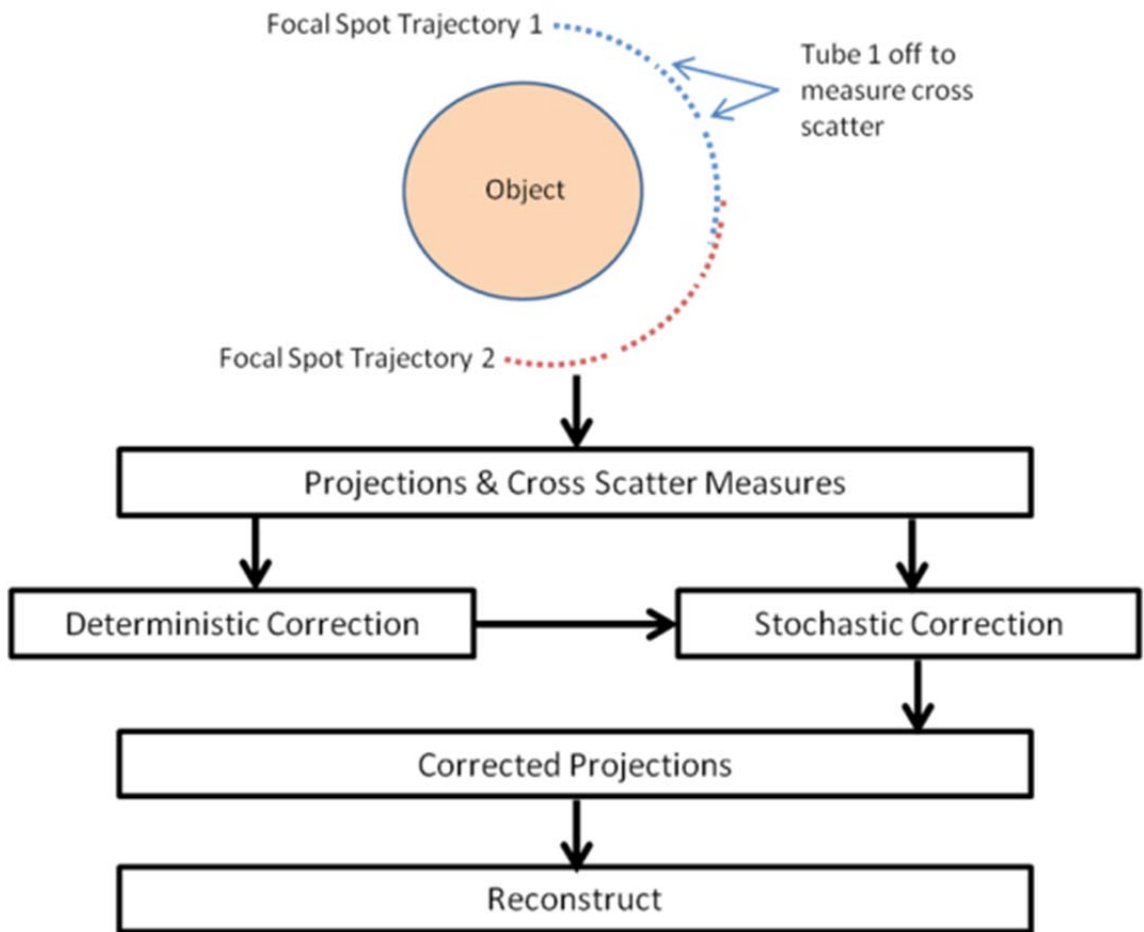


Figure 6.1: Illustration of the cross-scatter sampling protocol and flowchart of the correction strategy

6.3 Materials and Methods

6.3.1 Correction Strategy

The deterministic correction step is similar, in principle, to many forward-scatter correction techniques that rely on BSAs or collimator shadows to estimate the forward-scatter at several points on the detector and then interpolate across the detector plane [46]. Estimation of the scatter distribution is the first step in correction. Substantial literature exists suggesting that the scatter distribution can be sampled and then interpolated across the detector plane. Here, we propose to sample along the rotation axis by cutting projections. This is accomplished by only firing a single X-ray tube periodically throughout the scan which allows a direct measure of the entire cross scatter distribution at that particular angle.

After the scan is completed, the cross-scatter measurements and the projections are separated. The first step in the correction is to mask the shine-by regions in the cross-scatter measurements. These are regions which in the previous projection were exposed to the full intensity of the primary beam, *i.e.* there was no attenuating object between the bowtie filter and the detector in those pixels. The shine-by regions are identified as any pixels that have an attenuation of less than 5%, as given in Equation (6.1), in the previous projection.

$$Attenuation = \frac{Pixel\ Value\ in\ Previous\ Projection}{Pixel\ Value\ in\ Blank\ Image\ with\ Bowtie} \quad (6.1)$$

The measured cross scatter distributions are low-pass filtered according to the filter expressed in Equation (6.2) and illustrated in Figure 6.2, where the cutoff frequency (f_c) was chosen to be 40 bins from zero and the width of the falloff region (d) was chosen to be 40 bins.

$$h(f) = \begin{cases} 1 & f < f_c - \frac{d}{2} \\ \frac{1}{2} \left[1 - \cos \left(\pi \frac{f - (f_c - \frac{d}{2})}{d} \right) \right] & f_c - \frac{d}{2} \leq f \leq f_c + \frac{d}{2} \\ 0 & f > f_c + \frac{d}{2} \end{cases} \quad (6.2)$$

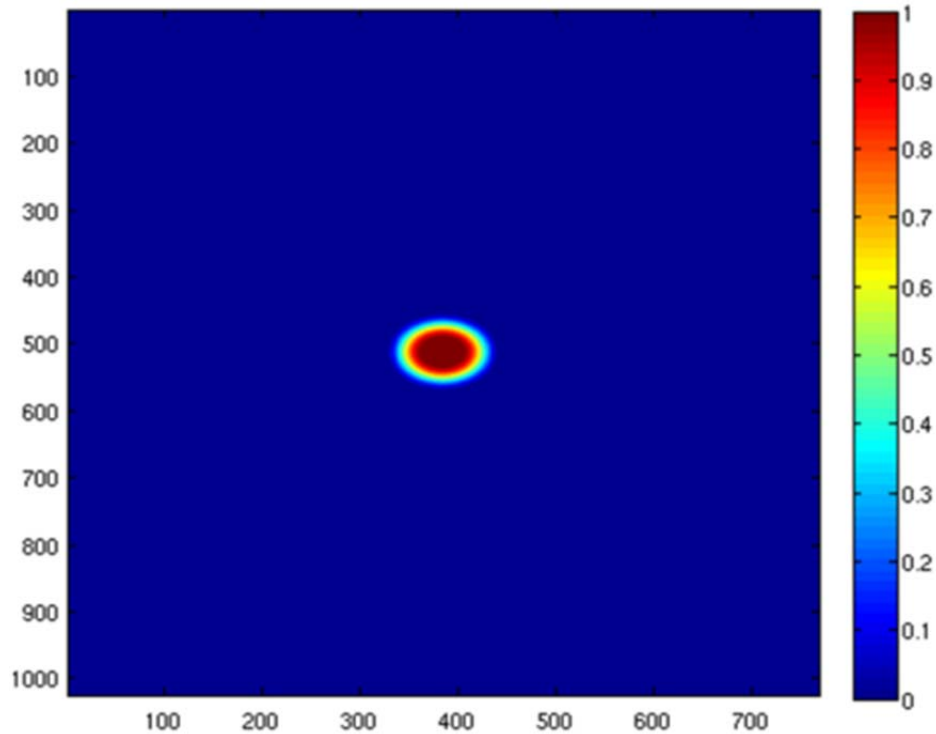


Figure 6.2: Representation of radially symmetric low-pass filter.

The cross-scatter distributions for every angle where there was not a cross-scatter measurement were estimated by cubic spline interpolation between the filtered cross-scatter distributions. Finally, the cross-scatter estimates are subtracted from projections.

6.3.2 Cross-Scatter Sampling Frequency

In order for the proposed method to be practical, it must not require a large number of projections be cut for the purposes of cross scatter measurements. Cutting too many projections can result in a substantial loss of angular sampling. To determine the sampling frequency two complimentary studies were performed: one that provides necessary data for a theoretically justified sampling frequency and a second that experimentally determines the accuracy of different sampling frequencies. Cross-scatter distributions are dependent on the shape of the scattering object, thus the sampling frequency required for one object is not necessarily the same for another. For the following studies anthropomorphic phantoms that represent three anatomic sites of interest for radiation therapy are used: head and neck phantom, lung phantom, and pelvic phantom.



Figure 6.3: Anthropomorphic pelvic phantom.



Figure 6.4: Anthropomorphic phantom used for the head and neck and lung anatomic sites.

6.3.2.1 Nyquist Sampling Frequency

The Nyquist sampling criteria (Equation (6.3)) describes the sampling frequency (f_s) required to reconstruct a signal with a maximum frequency (B) without aliasing.

$$f_s > 2B \quad (6.3)$$

Therefore, if the maximum frequency of the cross-scatter distribution as a function of angle can be known for a given object, an appropriate sampling frequency can be determined.

The cross-scatter distributions for the three phantoms were measured 517 times evenly distributed over 360° . The angular frequency content of the cross-scatter distribution was measured by taking the Fourier transform of each pixel along the angular direction and then averaging the spectra obtained for each pixel. This provided a single measure of the angular frequency content of the cross-scatter distribution.

Since the signal detected by any one pixel contains Poisson noise, the spectrum obtained above will be non-zero for all frequencies because the Fourier transform of a Poisson distribution is a flat line. This implies that strictly speaking no maximum frequency, beyond which all other Fourier coefficients are zero, exists. However, for the purposes of this study, the angular frequencies that are of greatest interest are those that are greater when the object is rotating than when the object is stationary. These are the frequencies that contain information on how the rotation of the phantom effects the cross scatter. Thus, angular (technically temporal) spectra for the phantom at eight different orientations with a rotation speed of zero were obtained. The eight different orientations were acquired at 45° intervals where 0° was defined as an anterior-posterior projection from the irradiating X-ray tube. This was repeated for both X-ray tubes. The maximum frequency was then the frequency where the spectra of the stationary and

rotating phantom diverges which is then used to define the minimum theoretical sampling frequency.

6.3.2.2 Empirical Sampling Frequency

In addition to determining the Nyquist sampling frequency, the minimum sampling frequency for the pelvic phantom was also determined empirically. This was done by scanning the pelvic phantom over 110° with 164 projections twice, each time only firing a single X-ray tube and acquiring data from both detectors, thereby providing a cross-scatter measurement at every projection angle. Then small numbers, starting with 3 and going up to 30, of these projections are used as simulated cross-scatter measurements. They are filtered according to Equation (6.2). The cross-scatter distributions for the other projection angles are then interpolated from the few selected, filtered measurements. The interpolated cross-scatter distributions are then compared to the measured cross-scatter distributions according to Equation (6.4), where I and J are the size of the detector matrix, and θ is the projection angle.

$$Error(\theta) = \frac{1}{IJ} \sum_{i,j} \left(\frac{Actual\ CS(\theta) - Interpolated\ CS(\theta)}{Actual\ CS(\theta)} \right)_{i,j} \quad (6.4)$$

6.3.3 Correction Evaluation

To evaluate the effectiveness of this method, the cross-scatter sampling frequency that was determined for the anthropomorphic phantoms was applied to the Catphan. This phantom allows measurement of contrast (Equation (6.5)) and contrast-to-noise ratio (CNR) (Equation (6.6)), where μ is the mean value in the ROI or background

region and σ is the standard deviation of pixel values in the background region. The ROIs and the background regions are the same as used in Chapter 4 and displayed in Figure 5.2.

$$C = \frac{|\mu_{ROI} - \mu_{BG}|}{\mu_{BG}} \quad (6.5), \quad CNR = \frac{|\mu_{ROI} - \mu_{BG}|}{\sigma_{BG}} \quad (6.6)$$

6.4 Results

6.4.1 Cross-Scatter Sampling Frequency

6.4.1.1 Nyquist Sampling Frequency

Figure 6.5-8 show results of the frequency analysis described in section 6.3.2.1. The plots of the stationary phantoms are generally the same shape as one another, but have different magnitudes. This is expected because there is no normalization applied and therefore the differences in magnitude of the cross-scatter distributions for the different orientations manifest as differences in the magnitude of the Fourier components. The stationary spectra also diverge from the flat line of a pure Poisson distribution due to the detector noise and calibrations applied to the raw data. In the higher frequency ranges, frequency shape and magnitude for the rotating phantom are similar to those for the stationary case. However, the rotating case has substantially greater lower frequency content compared to the stationary phantoms. This additional low-frequency content is the Fourier transform representation of angular variations in phantom cross scatter. The rotating phantom spectra diverge from the stationary spectra at or below approximately 0.041 cycles per degree for each of the three phantom

anatomical sites. This is taken as the maximum frequency – along the angular direction – of the cross-scatter distribution and is just under half of the sampling frequency of 10 samples in a 110° rotation. Therefore, 10 samples per 110° meets the Nyquist sampling criteria for the cross-scatter distribution for the phantoms studied.

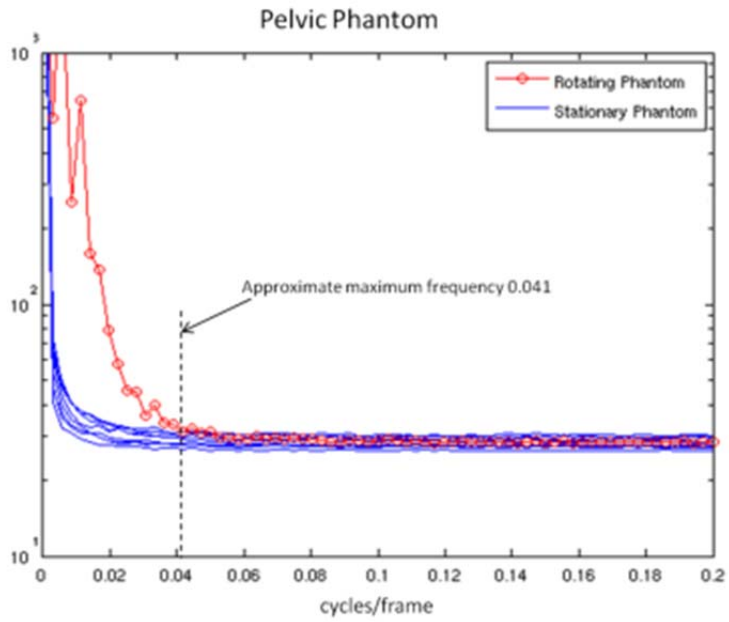


Figure 6.5: Cross-scatter angular frequency content of anthropomorphic pelvic phantom.

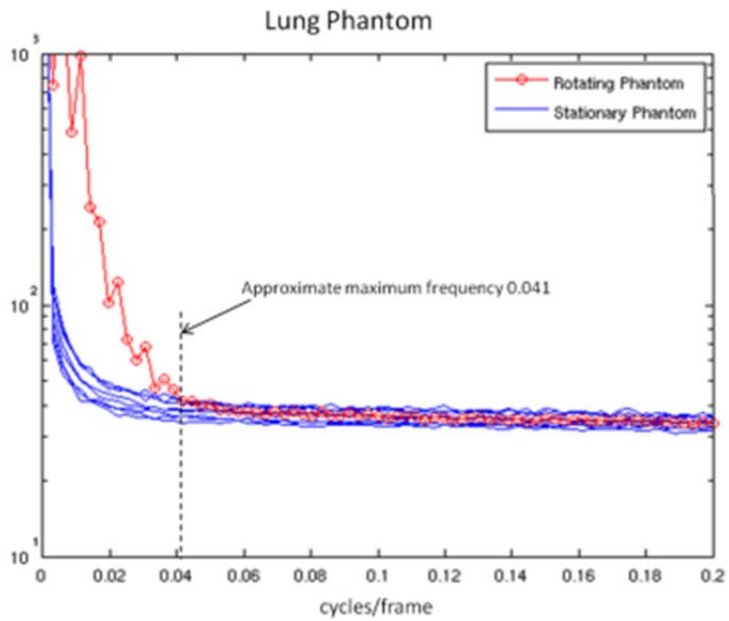


Figure 6.6: Cross-scatter angular frequency content of anthropomorphic lung phantom.

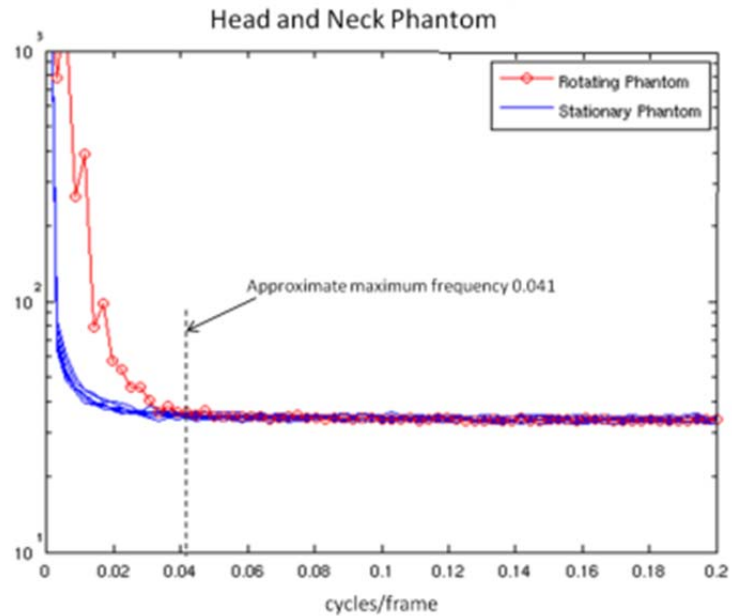


Figure 6.7: Cross-scatter angular frequency content of anthropomorphic lung phantom.

6.4.1.2 Empirical Sampling Frequency

Cross-scatter estimation error – Equation (6.4) – is shown in Figure 6.8 for the 3 sample and 10 sample cases, where 10 samples corresponds to the theoretical sampling minimum found in the previous section. Here, the error in the 10 sample case is essentially flat as a function of angle. In contrast the error in the 3 sample case varies greatly with angle – with large peaks in between each scatter sample. These peaks exceed 25% error.

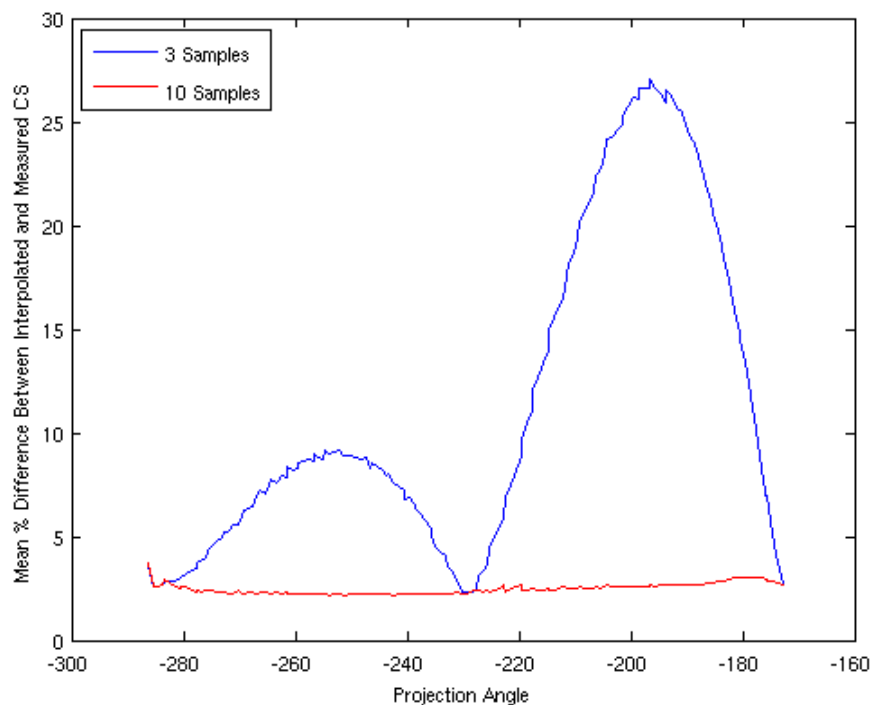


Figure 6.8: Scatter estimation error averaged over all pixels as a function of projection angle for 3 and 10 cross-scatter samples in a 110 degree acquisition.

Figure 6.9 shows a plot of the relative error between interpolated and measured cross-scatter distributions (Equation (6.4)) averaged over all projection angles for each detector as a function of the number of cross-scatter samples. The error levels off by 10 cross-scatter samples over 110 degree scan or a sampling frequency of about 1 every 11 degrees. The error never reaches zero because the interpolated distributions are based on filtered data which are being compared to noisy measurements.

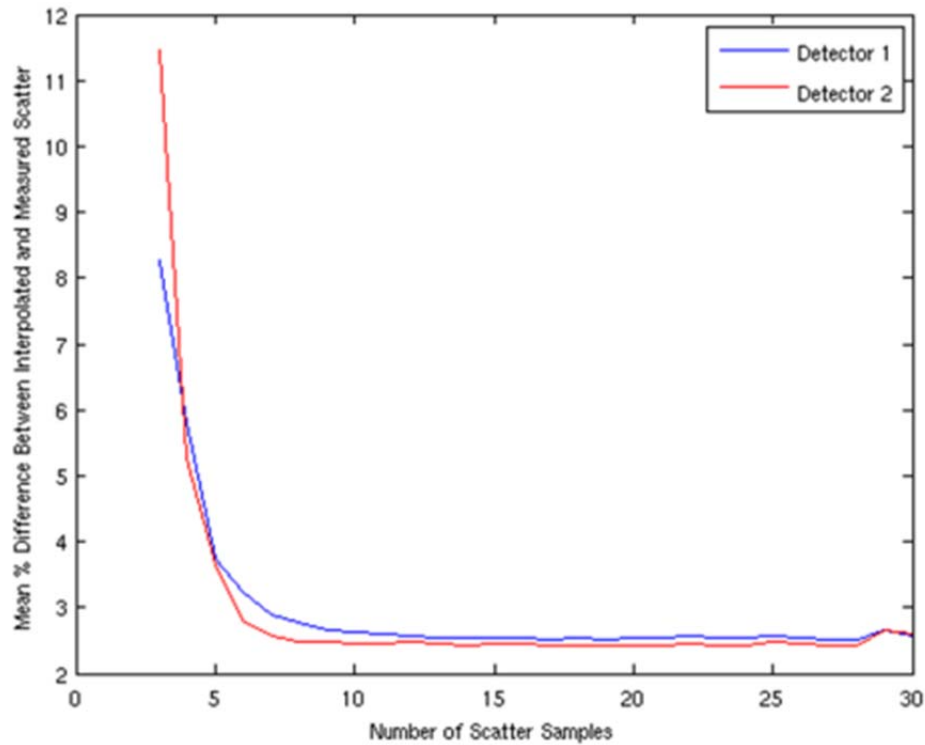


Figure 6.9: Mean error in interpolated cross-scatter distributions averaged over all pixels and projection angles as a function of the number of cross-scatter samples taken.

6.4.2 Correction Evaluation

Figure 6.10 shows a reconstruction of the Catphan indicating the numbered ROIs (which are the same as in Figure 5.2) as well as where the profiles were taken for Figure 6.11. The profiles from the corrected and cross-scatter-free images are nearly identical except that the corrected profile is noisier. The contrast and CNR recovery is given in Table 6.1 for each ROI relative to the gold standard cross scatter free case. The uncorrected reconstruction has an average of 83.6% of the contrast in the cross scatter free reconstruction. When the correction is applied the contrast is recovered nearly 100%

at 99.3%. CNR recovery without the correction was 64.8% on average and the correction, with an average of 63.5%, did not improve CNR recovery.

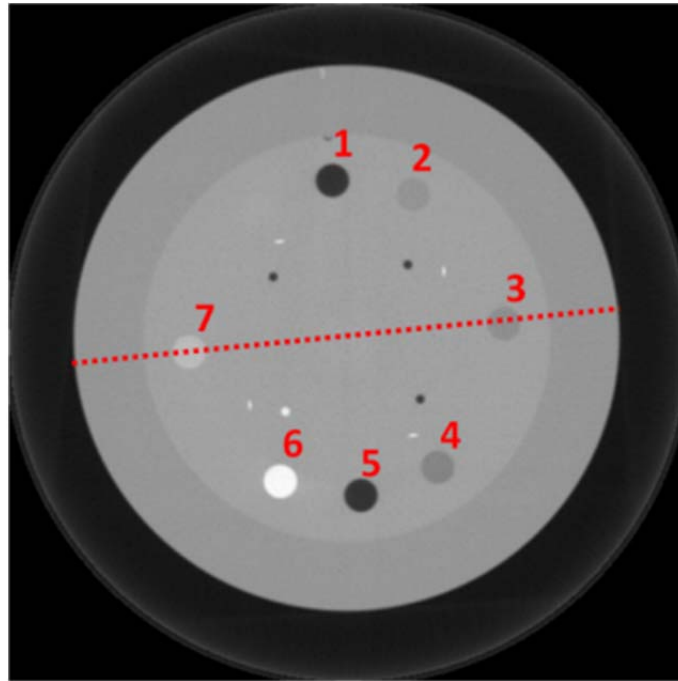


Figure 6.10: Reconstructed image of the Catphan showing the ROI numbers and indicating where the profiles for Figure 6.11 were taken.

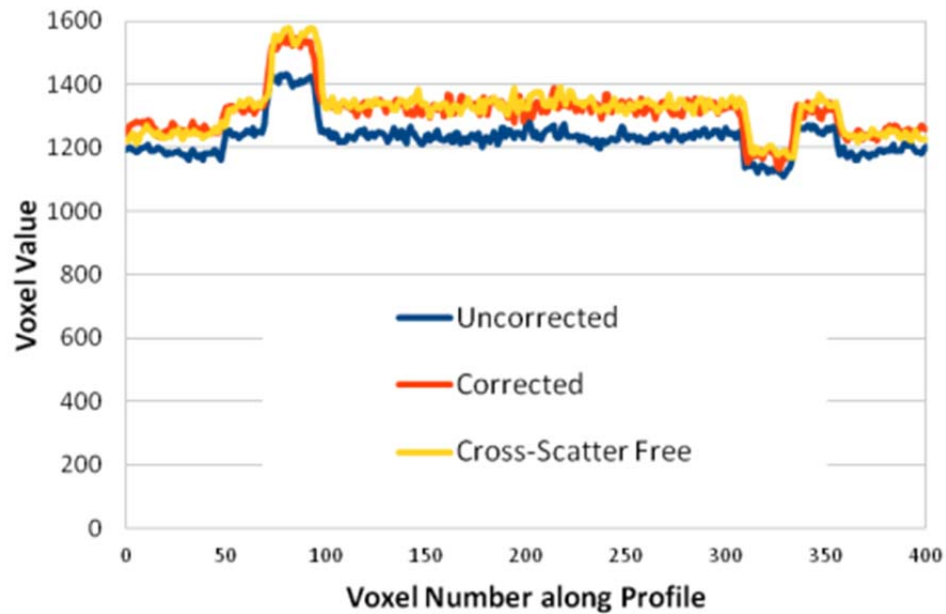


Figure 6.11: Horizontal profiles through reconstructions along the line indicated in Figure 6.10.

Table 6.1: Contrast and CNR recovery for the uncorrected case with cross scatter and with the correction applied. The reductions reported are relative to a scan of equal dose, but no cross scatter present in the scan.

Relative Contrast Recovery								
	ROI 1	ROI 2	ROI 3	ROI 4	ROI 5	ROI 6	ROI 7	Average
No Correction	85.1%	81.5%	80.1%	81.6%	84.4%	84.0%	88.5%	83.6%
Corrected	98.4%	100.6%	96.1%	98.0%	98.3%	99.9%	104.2%	99.3%
Relative CNR Recovery								
	ROI 1	ROI 2	ROI 3	ROI 4	ROI 5	ROI 6	ROI 7	Average
No Correction	66.0%	63.2%	62.1%	63.3%	65.5%	65.1%	68.6%	64.8%
Corrected	62.9%	64.3%	61.4%	62.6%	62.8%	63.8%	66.6%	63.5%

6.5 Discussion

A cross scatter sampling interval of ten degrees was determined to be sufficient for the three phantom anatomical sites used in this study. This sampling interval has the added advantage of being easy to implement as it can be easily divided into common scan ranges for CBCT such as 200° or 360° . It has been shown that cross scatter depends heavily on the shape of an object [70] [71] and, therefore, this sampling interval used in this study may not be sufficient for objects that have dramatically different shapes.

This correction has certain similarities with other correction that have been proposed. For example, Ning [46] proposed to measure forward scatter intermittently using a beam stop array. Here, we also propose to measure cross scatter intermittently, but also suggest a minimum sampling interval based on anthropomorphic phantoms. Additionally, the method proposed here does not require any additional hardware beyond what is required for the imaging task unlike several methods that require different kinds of beam stops [46] or detector elements that are unexposed by the primary beam [47, 48].

The cross scatter correction provided full recovery of the contrast in reconstructions. The CNR, however, was not improved by the low-frequency correction. Even though the contrast was greatly improved the subtraction of the low-frequency portion of the cross scatter degrades the noise in the image which, for the phantoms studied here, resulted in a CNR equal to that of the uncorrected image. A correction

specific to the high-frequency components of the cross scatter may improve the CNR recovery and such a correction is the focus of the next chapter.

6.6 Conclusion

Cross scatter at all angles can be accurately estimated from direct measurements of cross scatter taken at a small number of skipped projections. These estimates can be used to fully recover the contrast lost due to cross scatter.

7. Stochastic Scatter Correction

7.1 Motivation

The deterministic correction presented in Chapter 6 provides excellent contrast recovery in reconstructed images; however, does not improve CNR. This is partly because the deterministic correction ignores the high-frequency portion of the cross-scatter which most strongly contributes to the noise metrics used in Chapter 6. The aim of this project is to make use of the high frequency information contained in the cross scatter measurements (section 6.2) to correct for the high-frequency components of the cross scatter that are present in the projections.

7.2 Methods and Materials

7.2.1 Theoretical Basis for Spectral Subtraction

The high-frequency, stochastic correction is based on a technique known as spectral subtraction. This is a common technique for reducing noise in acoustic signals when the noise can be assumed to be independent of the signal and approximately stationary – *i.e.* white noise [91]. If the stated assumption holds the measured signal can be expressed as Equation (7.1), where y is the measured signal, x is the true signal, and n is the independent, stationary noise [91] The following derivation is presented by Vaseghi in *Advanced Digital Signal Processing and Noise Reduction* [91] and by Zavaheri [92].

$$y(t) = x(t) + n(t) \quad (7.1)$$

Taking the Fourier transform of both sides yields Equation (7.2).

$$Y(\omega) = X(\omega) + N(\omega) \quad (7.2)$$

The complex conjugate of Equation (7.2) is given in Equation (7.3) where $\Delta\theta$ is the phase difference between $X(\omega)$ and $N(\omega)$. Taking the expected values of both sides of Equation (7.3) gives Equation (7.4).

$$|Y(\omega)|^2 = |X(\omega)|^2 + |N(\omega)|^2 + 2|X(\omega)||N(\omega)|\cos(\Delta\theta) \quad (7.3)$$

$$E\{|Y(\omega)|^2\} = E\{|X(\omega)|^2\} + E\{|N(\omega)|^2\} + 2E\{|X(\omega)|\}E\{|N(\omega)|\}E\{\cos(\Delta\theta)\} \quad (7.4)$$

Here the derivation branches in two directions. First, the assumption could be made that $E\{\cos(\Delta\theta)\} = 0$, which implies that there is an expected phase difference between the noise (n) and the true signal (x). This results in Equation (7.5) and is known as spectral power subtraction.

$$|X(\omega)|^2 = |Y(\omega)|^2 - |N(\omega)|^2 \quad (7.5)$$

Alternatively, the assumption could be made that there is no expected phase difference between the noise (n) and true signal (x): $E\{\cos(\Delta\theta)\} = 1$. This is known as spectral magnitude subtraction, Equation (7.6) and is what was used for this study.

$$|X(\omega)| = |Y(\omega)| - |N(\omega)| \quad (7.6)$$

According to Equation (7.6), the magnitude of the Fourier transform of the true signal can be estimated with the measured signal and some estimate of the noise or an estimate of the noise spectrum. Of course, in order to perform and inverse Fourier transform, the phase and not just the magnitude must be known. In practice, this is very easily overcome by using the phase information from the measured signal. Once that

phase information is added to the magnitude calculated with Equation (7.7) – where $p(Y(\omega))$ is the phase angle of $Y(\omega)$ – an inverse Fourier transform to solve for $x(t)$, the true signal. This procedure is illustrated in Figure 7.1.

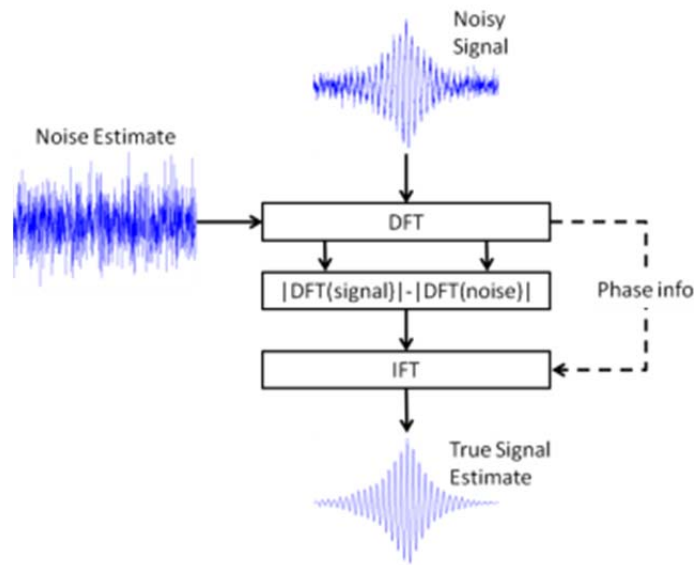


Figure 7.1: Flowchart of spectral magnitude subtraction.

7.2.2 Application of Spectral Subtraction for Cross Scatter Correction

To apply this method to the specific case of cross scatter correction, the measured signal – $y(t)$ in Equation (7.1) – becomes the result of the deterministic correction (Chapter 0). That is, projections that have had the low-frequency, deterministic cross-scatter distribution subtracted from them. This leaves the high-frequency stochastic noise added by the cross scatter as $n(t)$ in Equation (7.1). The noise estimates were

obtained by filtering the cross-scatter measurements with Equation (7.8).

$$h(f) = \begin{cases} 0 & f < f_c - \frac{d}{2} \\ 1 - \frac{1}{2} \left[1 - \cos \left(\pi \frac{f - (f_c - \frac{d}{2})}{d} \right) \right] & f_c - \frac{d}{2} \leq f \leq f_c + \frac{d}{2} \\ 1 & f > f_c + \frac{d}{2} \end{cases} \quad (7.8)$$

No interpolation of the stochastic noise estimates was performed, instead, for each angle the nearest noise estimate was chosen and used during the spectral magnitude subtraction. Figure 7.2 shows an updated flowchart of the spectral subtraction process as it applies to this specific correction. Note, that an extra step, windowing, has been added. This step was applied to help meet the assumption of stationary noise and is discussed further in the next section.

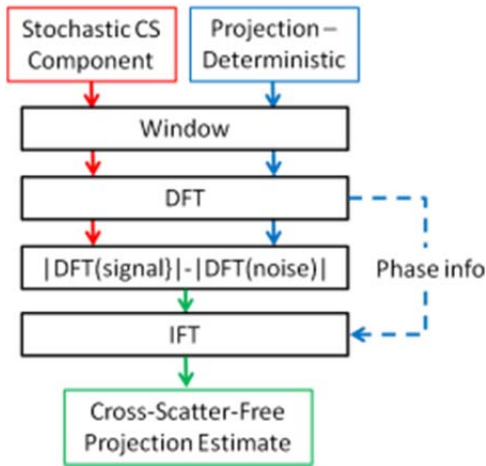


Figure 7.2: Flowchart of the spectral subtraction process as it is applied in the high-frequency component of the cross scatter correction.

7.2.3 Windowing

Spectral subtraction assumes that the noise is stationary and therefore only applies to noise that is largely independent of its phase. It cannot be used to correct for the low-frequency content of the cross-scatter distribution because of its regular shape. The existence of the regular shape suggests that the phase of the low-frequency components is important and these low frequency components are not stationary. Further, X-ray distribution itself is well described by Poisson statistics and therefore the variance of the number of X-rays incident on a given pixel is equal to the mean number of X-rays that are incident on that pixel if a given projection is repeated exactly many times. Thus, even though application of the gain and offset corrections mean that the data is no longer strictly a Poisson distribution, the variance still changes with the mean. This implies that the high-frequency noise is not stationary. However, if the variance changes slowly across the detector, then local stationarity may be assumed and spectral subtraction may be applied locally.

To apply the spectral subtraction to a local region of the image a novel two dimensional, overlapping window was developed. The equation for the window is given in Equation (7.9), where r is half the width of the window, and it is plotted in Figure 7.3.

$$w = \cos^2\left(\frac{x \times \pi}{2r}\right) \cos^2\left(\frac{y \times \pi}{2r}\right) \quad (7.9)$$

This window has two essential properties that make it suitable for this application. First, it falls off gradually to zero at the edges. This avoids ringing when taking the Fourier transforms. The second is that it can be overlapped such that it adds to one in every pixel as demonstrated in Figure 7.4.

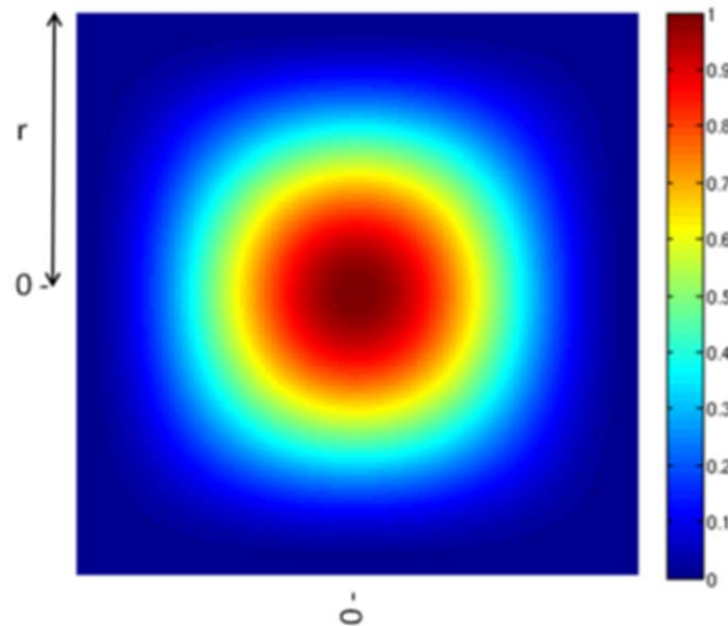


Figure 7.3: A two-dimensional plot of the overlapping window.

This window allows the spectral subtraction to be applied to individual segments of the image using the corresponding segments of the noise estimate. This was done by padding the projections and the noise estimates with zeros, r pixels on each side. The first segment starts in one corner of the padded images and the second is moved over in one direction a distance r . Once the window has reached the segment on the furthest edge it is shifted a distance r along the other dimension and then back across the image. Once all segments have been processed via spectral subtraction, they are all

added back together and the regions corresponding to the padding are discarded. When the segments are added back together, the total weight of the window as it was applied across all segments of the image adds to one.

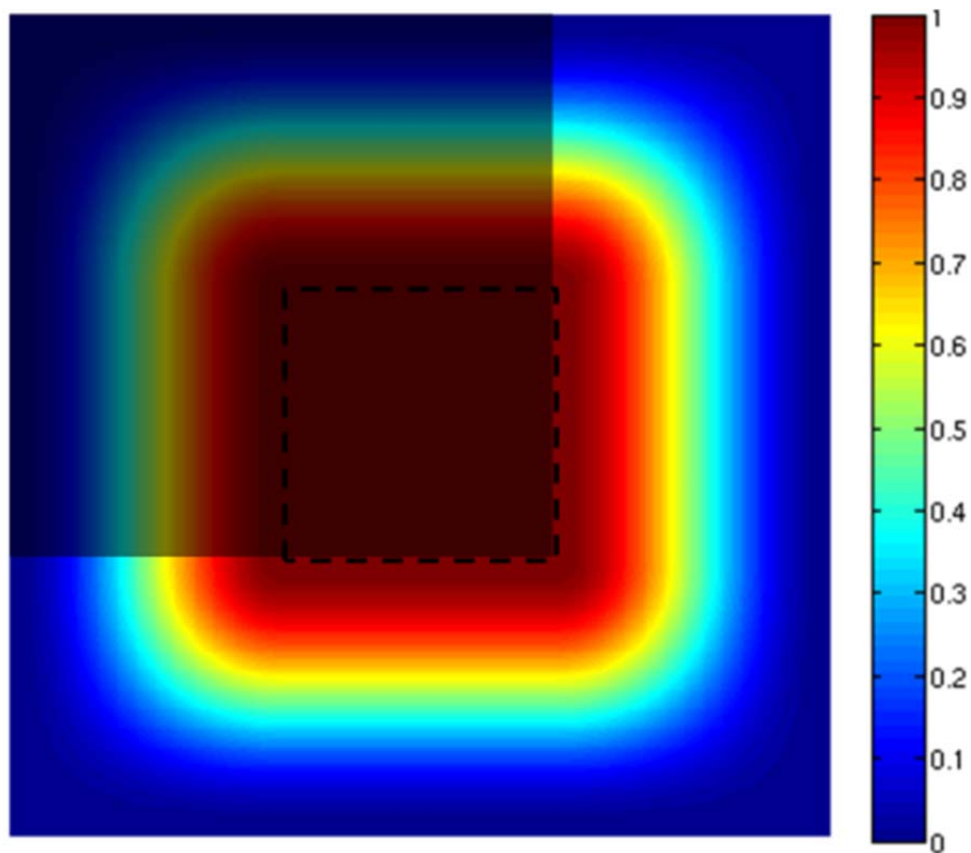


Figure 7.4: Four overlapping windows offset by a half the total width of the window (r). The shaded region in the upper right indicates the size of a single window and the region indicated by the dashed lines shows where the four windows overlap.

The size of the window is varied to evaluate the sensitivity of the spectral subtraction technique to the stationarity of the noise within the window. The window size is varied by setting r equal to 8, 16, 32, 64, and 128 pixels. These values are chosen so

that the size of the window will divide equally into both dimensions of the projection, 1024 x 768.

The stationarity within each windowed segment was calculated as the range of the variances within that segment. This was measured by acquiring 100 measurements of the cross scatter with the phantom in the same position and then applying the low-frequency correction to those projections. The resulting images, which contained only high-frequency components of the cross scatter, were used to calculate the variance of the high-frequency components of each pixel. Then the range of variances (maximum variance minus the minimum variance) within each segment was calculated. For each window size, the median range of all segments was reported. As a practical approximation to measuring the variance in each pixel value, the range of pixel values in each windowed segment after the low-frequency correction was also calculated.

7.2.4 Correction Evaluation

The effectiveness of the high frequency correction was evaluated using two metrics. The first, CNR recovery as defined in Chapter 0. The second measures the loss of resolution due to the application of the high-frequency correction. Resolution was measured by calculating contrast in line pair gauge in the Catphan reconstructed at very high resolution (0.0976 mm voxels). To correct for some of the slight differences in the overall contrast of each reconstruction, the reported values of contrast for the different line pairs were normalized to the value of contrast on line pair 1.

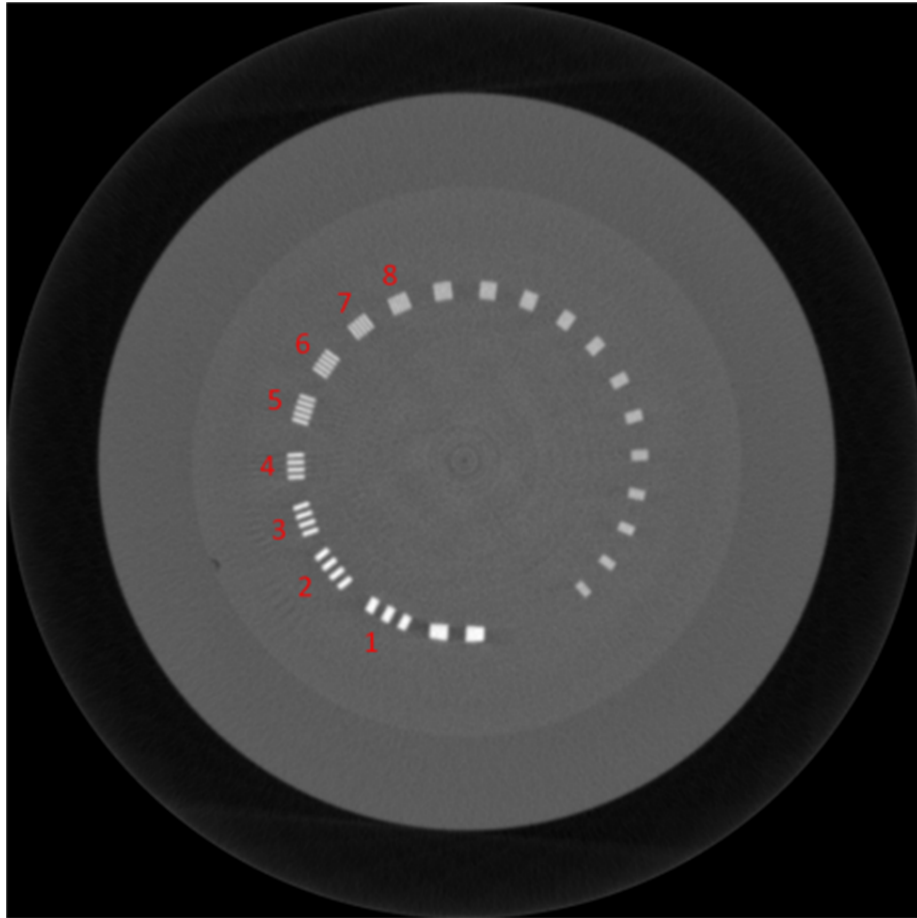


Figure 7.5: Reconstructed slice of the line pair gauge of the Catphan. The number line pairs are the ones that were used to measure resolution. Their physical dimensions are given in Table 7.1.

Table 7.1: Physical size of the line pairs used to measure resolution.

Line Pair	lp/cm	Gap Size (cm)
1	2	0.25
2	3	0.167
3	4	0.125
4	5	0.1
5	6	0.083
6	7	0.071
7	8	0.063
8	9	0.056

7.3 Results

Table 7.2 is an expanded version of Table 6.1 that shows the contrast and CNR recovery for each ROI when the high frequency correction is applied with varying window sizes. The high-frequency correction has very little effect on the contrast recovery. When the high-frequency correction is applied without windowing, it does not improve the CNR recovery at all. However, when the overlapping two-dimensional window is applied, the CNR recovery improves by about 10%. The CNR recovery varies slightly with the size of the window, peaking at $r = 32$.

Figure 7.6 shows plots of the normalized contrast in the line pair gauges for the low-frequency correction, high-frequency correction without windowing, and the high-frequency correction with various window sizes. In these plots, very little reduction in resolution is visible; these observations are confirmed in Table 7.3 which lists the values plotted in Figure 7.6.

Table 7.2: Contrast and CNR recovery relative to the cross scatter free case for 8 cases: no correction; low-frequency (LF) correction only, no windowing (Equation (7.9)), and with windowing for 5 different values of r .

Relative Contrast Recovery								
	ROI 1	ROI 2	ROI 3	ROI 4	ROI 5	ROI 6	ROI 7	Average
No Correction	85.1%	81.5%	80.1%	81.6%	84.4%	84.0%	88.5%	83.6%
LF Correction	98.4%	100.6%	96.1%	98.0%	98.3%	99.9%	104.2%	99.3%
No Windowing	98.4%	100.6%	96.1%	98.0%	98.3%	99.9%	104.2%	99.3%
$r = 8$	98.5%	100.6%	95.9%	97.6%	98.3%	99.9%	104.4%	99.3%
$r = 16$	98.6%	101.1%	96.2%	98.0%	98.5%	100.1%	104.4%	99.6%
$r = 32$	98.5%	100.8%	96.1%	97.7%	98.5%	100.2%	104.1%	99.4%
$r = 64$	98.4%	99.8%	95.4%	96.8%	98.1%	99.8%	103.0%	98.7%
$r = 128$	97.9%	99.6%	95.1%	96.7%	97.8%	99.3%	102.6%	98.4%

Relative CNR Recovery								
	ROI 1	ROI 2	ROI 3	ROI 4	ROI 5	ROI 6	ROI 7	Average
No Correction	66.0%	63.2%	62.1%	63.3%	65.5%	65.1%	68.6%	64.8%
LF Correction	62.9%	64.3%	61.4%	62.6%	62.8%	63.8%	66.6%	63.5%
No Windowing	62.9%	64.3%	61.4%	62.6%	62.8%	63.8%	66.6%	63.5%
$r = 8$	71.3%	72.8%	69.4%	70.7%	71.2%	72.3%	75.6%	71.9%
$r = 16$	72.3%	74.1%	70.5%	71.8%	72.2%	73.4%	76.6%	73.0%
$r = 32$	73.0%	74.7%	71.2%	72.4%	72.9%	74.2%	77.1%	73.6%
$r = 64$	72.9%	73.9%	70.7%	71.7%	72.7%	73.9%	76.3%	73.1%
$r = 128$	72.4%	73.6%	70.3%	71.5%	72.3%	73.4%	75.8%	72.8%

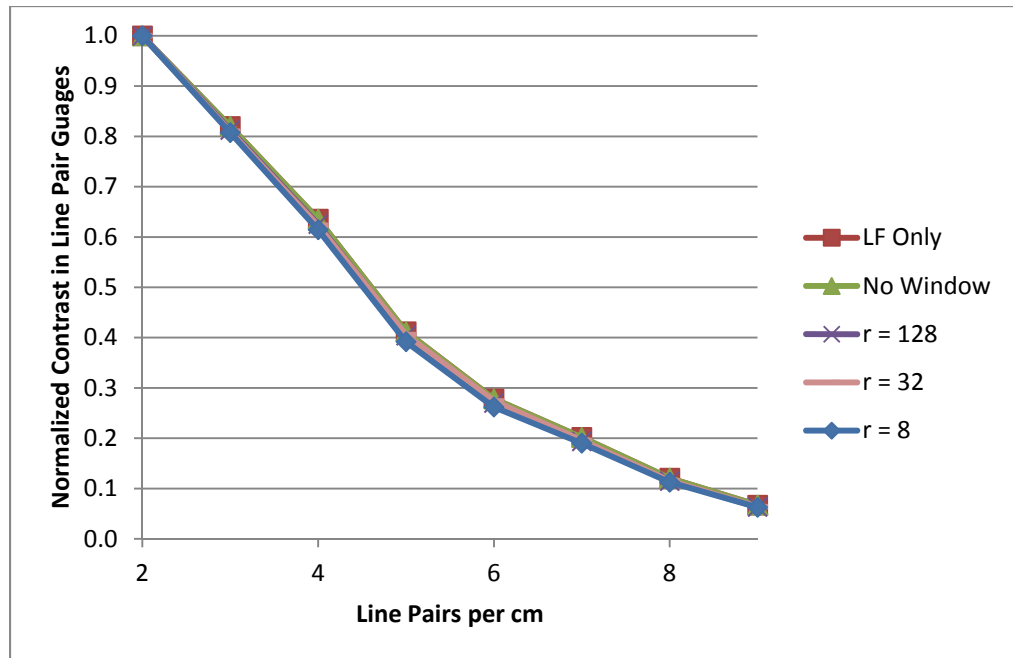


Figure 7.6: Plots of the normalized contrast for the low-frequency correction alone, the high-frequency correction with no windowing, and the high-frequency correction with windows of various sizes. The values plotted here are listed in Table 7.3.

Table 7.3: Normalized contrast for the plots in Figure 7.6.

	2 lp/cm	3 lp/cm	4 lp/cm	5 lp/cm	6 lp/cm	7 lp/cm	8 lp/cm	9 lp/cm
LF Only	1.000	0.820	0.636	0.412	0.278	0.202	0.121	0.067
No Window	1.000	0.820	0.636	0.412	0.278	0.202	0.121	0.067
r = 128	1.000	0.813	0.625	0.404	0.270	0.193	0.115	0.063
r = 32	1.000	0.810	0.623	0.406	0.274	0.196	0.115	0.064
r = 8	1.000	0.807	0.614	0.392	0.262	0.190	0.112	0.063

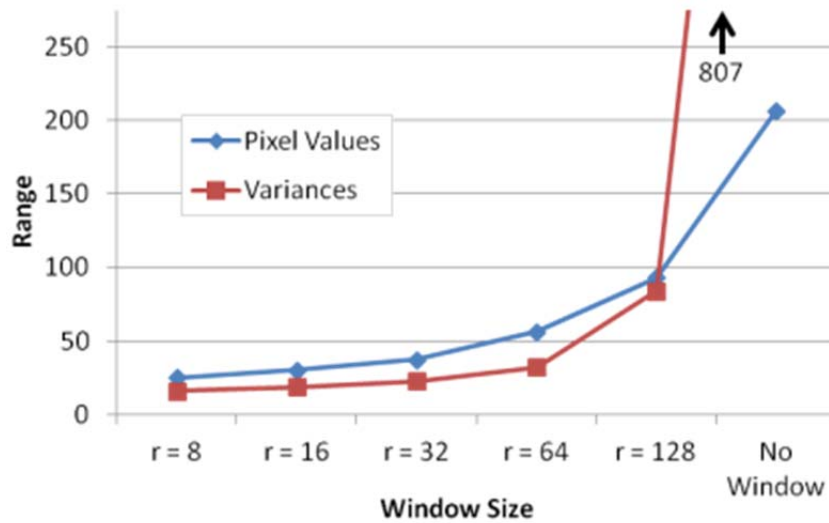


Figure 7.7: The stationarity of the noise within the windowed segments for varying window sizes.

Figure 7.7 shows the stationarity in the windowed segments for varying window sizes as estimated by the range of variances and pixel values within those segments. Using the overlapping, two-dimensional windowing greatly reduces the range of variances within the windowed segments. The range of variances continues to decrease with decreasing window size; however, it decreases slowly as r becomes less than 32. The range in pixel values shows a similar trend as the range in variances for the windowed cases.

7.4 Discussion

A novel technique for addressing the high-frequency content of cross scatter in dual X-ray imaging has been shown to improve CNR recovery while maintaining resolution using a small number of measurements of the cross scatter.

The use of an overlapping two-dimensional window allows the assumption of stationarity within that window. Without the use of this technique the spectral subtraction on its own does nothing to improve CNR. Improvements in the windowing, could lead to higher CNR recovery. For instance, in this study, only square windows were considered. It is possible that a rectangular window could be developed that could be larger along dimensions where the high-frequency noise is more stationary and short along dimensions where the variance changes rapidly.

The range of variances within the windowed segments provides an estimate of the stationarity of the high-frequency components of the cross scatter that was corrected using spectral subtraction. As a more practical estimate of the stationarity that could be implemented for a specific patient or phantom without a large ensemble of scatter measurements, stationarity was also estimated using the range of pixel values within the windowed segments. Both of these metrics showed very similar trends and therefore the pixel value range may be an acceptable and practical means of estimating stationarity for the purposes of choosing a window size.

The maximum CNR recovery was achieved using a window of $r = 32$. Smaller windows should increase the stationarity of the high-frequency cross scatter component within those windows. However, this is not the only factor contributing to the effectiveness of spectral subtraction. If the window is too small, then it begins to exclude some of the lower frequencies that were not corrected for in the low-frequency portion

of the correction (Chapter 0). For the window proposed here, the full-width at half maximum is equal to r . For $r = 8$, this corresponds to a cutoff frequency of 0.16 cycles/mm and the filter used to separate the low- and high-frequency components of the cross-scatter has a cutoff frequency of 0.10 cycles/mm. Therefore, using a window of only $r = 8$ does not apply corrections across the entire frequency spectrum.

Spectral subtraction provides a method for denoising images that does not require an estimate of the true signal. This is different from common filters used in image processing such as the Metz or Wiener filters. Since, in the implementation presented here, it uses a direct measurement of the high-frequency content of the cross-scatter it does not require modeling of the noise in the projection images. These measurements allow this correction to be self-adjusting to different sizes and shapes of patients in the scanner without the need for determining specific parameters.

The use of the overlapping windowing scheme and spectral subtraction proved an effective combination of techniques for reducing high frequency noise. This could be potentially applied to forward scatter as well if appropriate noise models exist since it is extremely difficult, if not impossible, to measure the high-frequency content of the forward scatter across the face of the detector the way that it was measured for cross scatter here.

7.5 Conclusion

The proposed correction for the high-frequency components of cross scatter utilizing spectral subtraction and two-dimensional windowing provide increased CNR recovery with minimal losses in resolution.

8. Summaries and Conclusions

A realistic dual CBCT system was constructed to study the effects of scatter in dual X-ray imaging. Cross scatter in dual X-ray imaging was found to have a larger effect on reconstructions than forward scatter in phantoms larger than 20cm in diameter. The flexible timing system developed allowed implementation of the interleaved and cross scatter sampling techniques used for cross scatter avoidance and correction.

During the course of studying cross scatter in this system artifacts similar to the crescent artifacts in clinical CBCT systems were observed. This provided insights into the potential causes of these artifacts. Simulation studies identified three possible mechanical deviations that could lead to crescents artifacts in reconstructed images and a correction method was developed that largely mitigates the appearance of the crescent artifacts.

An interleaved technique was proposed and developed to avoid the effects of cross scatter in dual CBCT. It was shown to provide nearly identical contrast and CNR as cross scatter free reconstructions; however, it did reduce the projection acquisition rate. As a consequence, it may not be suitable for some imaging tasks in which high acquisition rates are necessary, such as 4D CBCT and 4D DTS.

A novel, two-step cross scatter correction technique was developed that uses intermittent samples of the cross scatter to correct both the low-frequency, deterministic portion of the cross scatter distribution as well as the high-frequency, stochastic portion

of the cross scatter. A sampling interval of ten degrees was found, via analysis of the angular frequency content of the cross scatter, to be sufficient for the three anatomic sites (head and neck, lung, pelvis) studied with anthropomorphic phantoms. A novel two-dimensional partitioning scheme was proposed which allows the application of non-local corrections or filters, such as spectral subtraction, to smaller portions of the image. This partitioning scheme helps to approximate stationary noise within each partition which is often assumed by non-local filters. The deterministic portion of the correction provided nearly 100% contrast recovery; however, it did not improve CNR. The stochastic correction improved CNR recovery from 63% in the deterministic correction to 73% with minimal losses in resolution.

Cross scatter can have severe effects in dual CBCT. However, with the use of interleaved avoidance these effects can be mitigated and dual CBCT does not suffer from greater scatter degradations than single CBCT. When an interleaved technique is ideal for a given imaging task, the proposed scatter correction technique can be used to retain contrast and improve CNR.

The developed dual X-ray imaging system with effective cross scatter correction and system alignment allows implementation of many new applications of image-guidance in radiation therapy. This technology enables techniques such as dual energy CBCT to reduce metal artifacts and beam hardening artifacts which can improve visibility of low contrast soft tissues that are the target of radiation therapy. Dual X-ray

imaging reduces the imaging time of CBCT which can help ensure that patient positioning remains constant throughout treatment and can also enable 4D imaging techniques to effectively manage organ motion.

9. Appendix: Dual Source CBCT User Guide

This appendix includes illustrated, step-by-step instructions for using the dual-source cone beam CT system in the dual X-ray lab. The instructions here describe a standard, continuous rotation acquisition.

9.1 Hardware Power-Up Procedures

1. Turn on detectors. The detectors are powered on with a toggle switch on the back near the power cord. The detectors should be turned on approx. 3 hours prior to use. This will allow them to reach thermal equilibrium which helps maintain a more constant dark current throughout the course of a scan.
2. Open water valves. All valves– **except the one that bypasses the filtration system** – in the water cooling system should be opened by turning the valve handle so that it is parallel with the pipe.
3. Turn on generators. The circuit breakers leading into the generators must be in the on position. Then press the power on button (vertical line) on the generator consoles.
4. Turn on the motion controller.
5. Turn on the stage by using the top button just to the right of the LED screen on the motion controller. The screen should indicate that Axis 1 motor is ON.
6. Press the 'Axis 1' button in the 'Home' group on the motion controller. This will reset the stage to its home position and recalibrate the device.

9.2 Data Acquisition

1. Once all of the hardware has been turned on and is ready for acquisition, load the main2.vi virtual instrument in LabVIEW and open Viva on each of the data acquisition computers.
2. Choose the appropriate detector mode in Viva.
3. Allocate memory buffers for frame grabber
4. Run the main2.vi in LabVIEW and click on the left-most tab.

9.2.1 Tab 1: Set Detector Frame Rate

The first tab, Figure 9.1, has several useful functions. The item numbers listed below correspond to the indicated portions of the graphical user interface (GUI) for the control software shown in Figure 9.1.

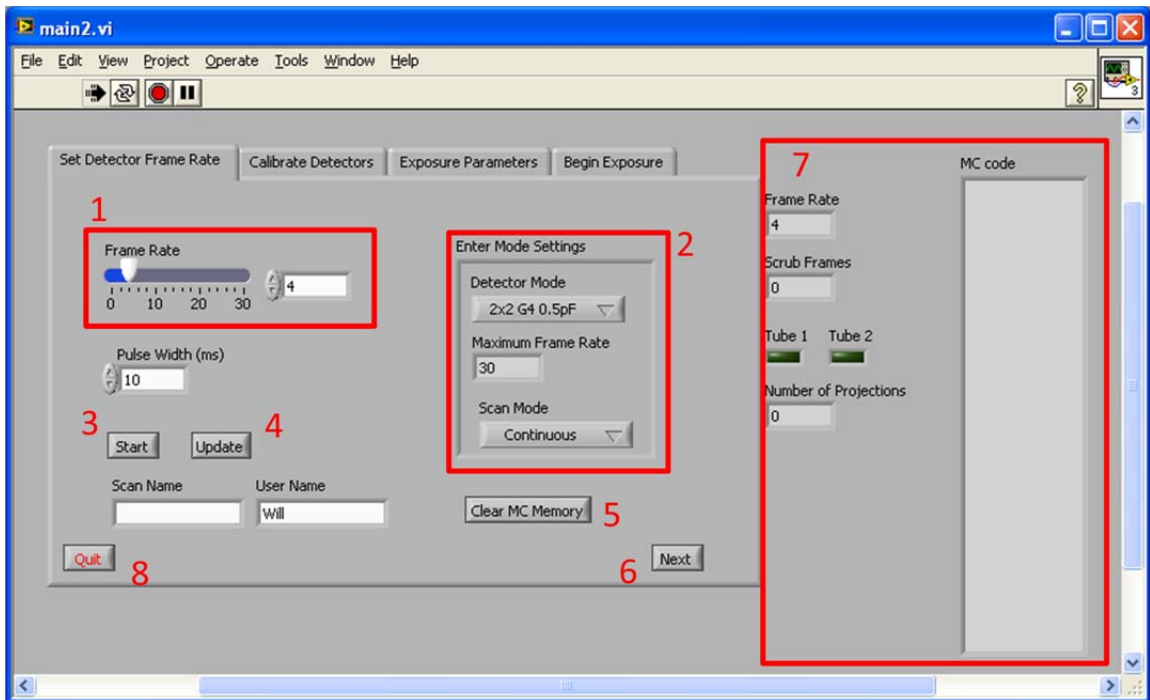


Figure 9.1: Tab 1 of the control software.

1. Frame rate setting. This defines the frame rate that the detectors at which the detectors will be operating during the scan. This should match the value in Viva that was used for the gain calibration of the detectors. The value can be set using the slider or the text box. This is a required input before moving to the next tab.
2. This portion of the GUI, displays the maximum frame rate for the detector mode selected from the drop down box. This in no way changes the behavior of the detectors during the scan and is only for the user's reference when setting the maximum frame rate. Additionally, the user can choose between step-and-shoot mode and continuous motion. Step

and shoot is no longer supported after the upgrade to hardware timed signals. Use of this mode is not recommended, but may still work.

3. This start button begins the detector waveforms (the User_sync signal). It is primarily used for debugging and testing purposes. It is not required.
4. The update button restarts the detector waveform with the current frame rate. This is primarily used for debugging and testing purposes. It is not required.
5. The clear motion controller memory button clears all of the memory buffers of the motion controller and puts the stage back to hardware zero and resets software zero to hardware zero. This button is useful when the memory buffer of the motion controller becomes full due to improper use of the software. See section 10.1.3 for further details. This button is not required for normal operations.
6. The next button accepts the inputs of a given tab and advances to the next tab. For all tabs this is the final step and is absolutely required. Manual advancement through the tabs (via clicking on them) will not ensure that all values are saved or that the necessary waveforms have been properly defined.
7. These indicators are used for debugging purposes.

8. The quit button is the only button that should be used to exit the software. This button runs scripts that ensure all outputs leading to any system device are off.

9.2.2 Tab 2: Calibrate Detectors

The second tab provides the tools to calibrate the detectors and warm up the X-ray tubes. If the tubes have been left idle for an extended period, the user should go through the warm-up procedure to ensure that the tubes are not damaged.

1. The tube warm-up button prompts the user through the tube warm-up procedure. The user will be prompted to set the kVp, mA, and ms for an exposure. This should be done any time the tubes have been idle for an extended period.
2. The fluoro switches will turn on the X-ray beam in fluoroscopy mode. These are used gain calibrations.
3. Calibration procedure instructions.

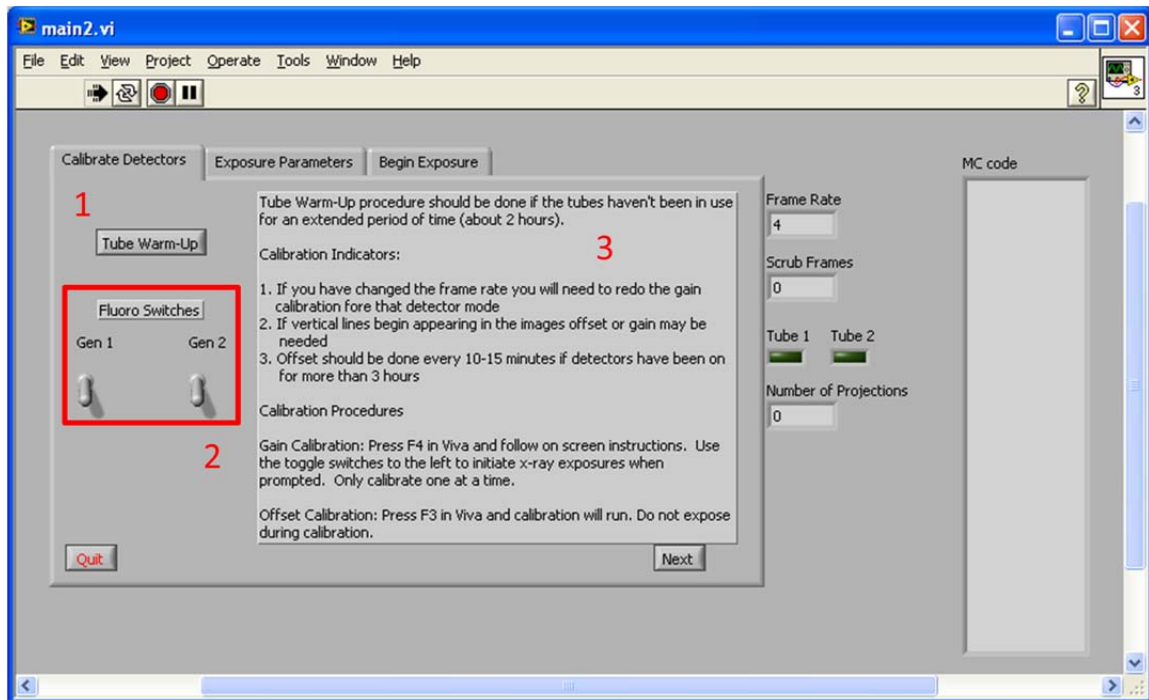


Figure 9.2: The second tab in the control software GUI.

9.2.3 Tab 3: Exposure Parameters

The third tab, **Error! Reference source not found.**, allows to the user to input the rest of the scan parameters. All available inputs on this tab are required for proper operation.

1. The number of scrub frames desired.
2. The initial angle of the rotation stage.
3. The number of unexposed frames before the scan starts. This is used to provide time for the user to begin data acquisition in the Viva program for each detector.
4. The final angle of the rotation stage.
5. The number of unexposed frames after a scan has completed.

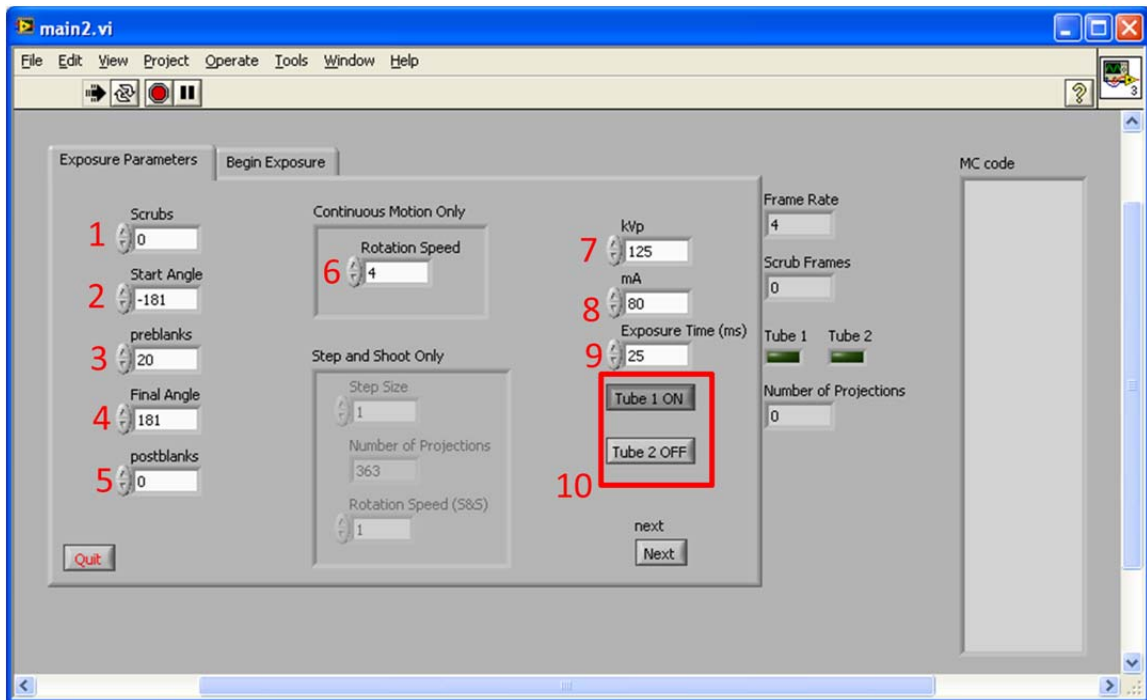


Figure 9.3: The third tab in the control software GUI.

6. The rotation speed of the stage in degrees per second.
7. The kVp of the scan. This has no bearing on the scan itself and will not change the kVp of the generators. It is used to provide a secondary log of the X-ray use.
8. The tube current (mA) of the generators. Also used for logging purposes and does not influence the scan.
9. The exposure length (ms) of the generators. It is vital that this number is correct. It is used to define the pulse length that requests exposures.
10. These buttons define which X-ray tubes are used for the scan.

9.2.4 Tab 4: Begin Exposure

The final tab, Figure 9.4, allows the user to begin the scan as well as stop any scans in progress. Once the scan has been initiated from this tab and completed normally, the program will return the state of all physical outputs to zero volts and end.

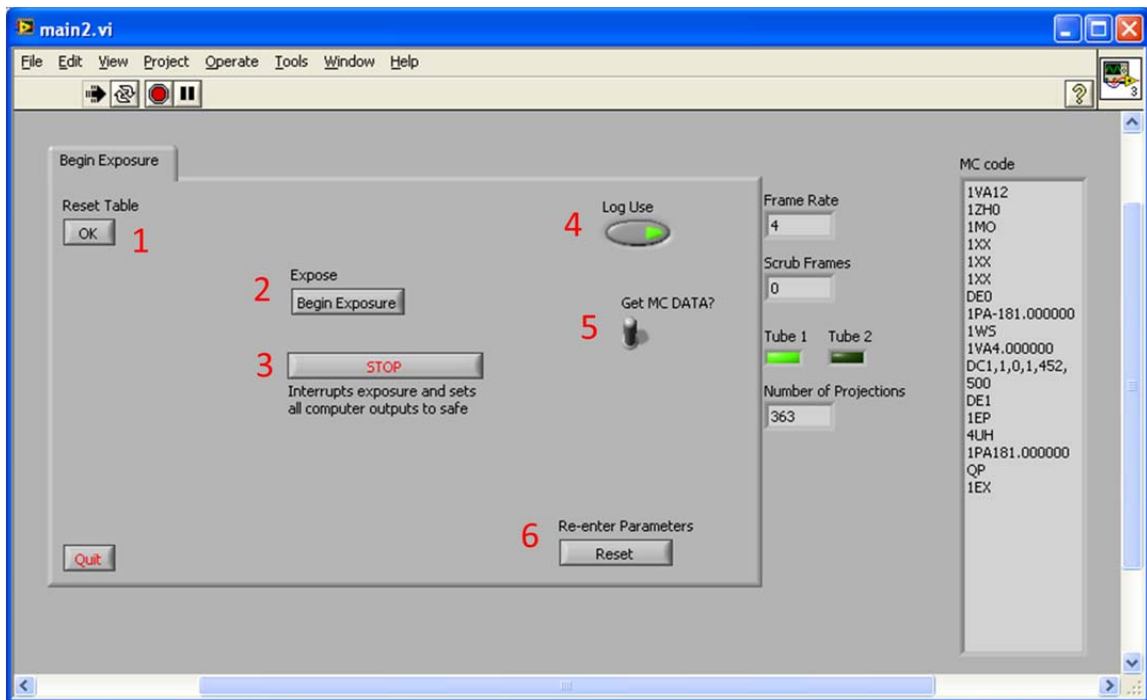


Figure 9.4: The final tab in the control GUI.

1. This button resends the program to the motion controller. It generally should not have to be used. Over use can lead to filling the memory of the motion controller which will keep the motion controller from executing any stored programs.
2. This button starts the exposures.
3. This button stops any scans in progress. All outputs to the X-ray tubes are set to safe levels and terminated.

4. This enables the backup software logging.
5. When flipped up, the software will guide the user through saving the projection angle files after the scan has completed.
6. This button allows the user to go back to the first tab and reenter any inputs that may need changing. The user should progress through the tabs as normal using the 'Next' button.

10. Appendix: Dual Source CBCT Troubleshooting Guide

There are a few known and unresolved bugs in the system software that will, on rare occasions, cause the system to behave in an unexpected manner. All of the software bugs are minor and at worst lead to the loss of a small number of projections. Incorrect use of the software and hardware may also lead to unexpected behavior. This appendix addresses the known bugs as well as several common mistakes that lead to unexpected system behavior. This appendix is organized by system component and further by the specific behaviors that indicate errors or bugs.

10.1 Motion Controller

10.1.1 Begins Rotation Too Early

Occasionally, the motion controller will begin rotating as soon as the 'Start Scan' button is pressed instead of waiting for the exposures to start. The specific cause of this is unknown, but this issue can be easily avoided. To avoid this problem, wait several seconds after the motion controller is stationary at the desired starting location. The indicator should remain constant for 3-4 seconds before you start the scan.

10.1.2 Does Not Rotate

If the 'Start Scan' button is pressed before the stage has settled on the starting location the stage will not rotate when the scan begins.

10.1.3 No Motor Detected

If the motion controller is turned off and the stage has been rotated past +/-150 degrees, the motion controller will not be able to detect it upon start up. All axes on the motion controller will display, "NO STAGE." There are three ways to solve this problem. One way is to turn on the motion controller and run main2.vi in LabVIEW. Then on Tab 1, use the Clear MC Memory button. This button will clear the motion controller memory, disable the hardware travel limits, and finally send the stage home. If that is successful restart the motion controller and it will detect the stage.

The other method is to use the buttons on the face of the motion controller. First push the top button immediately to the right of the LCD screen - which normally turns a motor on or off – one time. Then use the jog buttons to move the stage in one direction for about 90 degrees. If this is successful, restart the motion controller and it should detect the stage. If it does not give an error while moving the stage, but does not detect the stage upon the restart, follow the same procedure, but move the stage 180 degrees in the opposite direction.

Finally, if the previous two strategies fail, the ESP-Util program can be used to download a set of instructions that will move the stage. Open the program and establish communication with the stage and send the following commands: 1MO, 1ZH0, and 1PR-90. Then restart the motion controller. If this doesn't work, try again and replace 1PR-90 with 1PR180.

10.2 Detectors

10.2.1 Cannot Initialize Camera

If a second version of Viva is opened while another is running, Viva will throw an error stating that it cannot initialize the camera. Close all instances of Viva and restart. If this error persists make sure that the detectors are on and all connections are secure.

10.2.2 Allocate Buffers

If the buffers have not been allocated for the frame grabber, Viva will prompt the user to do so before beginning video acquisition. If this happens after a scan has been started, stop the scan and reset. Allocate the buffers and the video acquisition will be ready for any subsequent scans while Viva remains open.

10.3 Generators

The only known issues with the generators arise when one or both of the interlocks have been tripped. The generators will not even rotate the anode when either of the interlocks have been tripped and will start beeping when any actions are requested. Once the door is closed and the water is on these interlocks will clear and the generators will resume normal operation. To be safe, the control software should be quit before clearing the interlocks to ensure that the generators only fire when a user is present at the control console.

References

1. Jaffray, D.A. and J.H. Siewerdsen, *Cone-beam computed tomography with a flat-panel imager: Initial performance characterization*. *Medical Physics*, 2000. **27**(6): p. 1311-1323.
2. Ning, R., et al., *Flat panel detector-based cone beam volume CT imaging: detector evaluation*. *Medical Imaging 1999: Physics of Medical Imaging, Pts 1 and 2*, 1999. **3659**: p. 192-203.
3. Ning, R.L., et al., *Selenium flat panel detector-based volume tomographic angiography imaging: Phantom studies*. *Physics of Medical Imaging*, 1998. **3336**: p. 316-324.
4. Sorcini, B. and A. Tilikidis, *Clinical application of image-guided radiotherapy, IGRT (on the Varian OBI platform)*. *Cancer/Radiothérapie*, 2006. **10**(5): p. 252-257.
5. Smitsmans, M.H.P., et al., *Automatic prostate localization on cone-beam CT scans for high precision image-guided radiotherapy*. *International Journal of Radiation Oncology*Biology*Physics*, 2005. **63**(4): p. 975-984.
6. Hawkins, M.A., et al., *Assessment of residual error in liver position using kV cone-beam computed tomography for liver cancer high-precision radiation therapy*. *International Journal of Radiation Oncology*Biology*Physics*, 2006. **66**(2): p. 610-619.
7. Létourneau, D., et al., *Cone-beam-CT guided radiation therapy: technical implementation*. *Radiotherapy and Oncology*, 2005. **75**(3): p. 279-286.
8. Oldham, M., et al., *Cone-beam-CT guided radiation therapy: A model for on-line application*. *Radiotherapy and Oncology*, 2005. **75**(3): p. 271.E1-271.E8.
9. Kida, S., et al., *4D-CBCT reconstruction using MV portal imaging during volumetric modulated arc therapy*. *Radiotherapy and Oncology*, 2011. **100**(3): p. 380-385.
10. Li, T. and L. Xing, *Optimizing 4D cone-beam CT acquisition protocol for external beam radiotherapy*. *International Journal of Radiation Oncology*Biology*Physics*, 2007. **67**(4): p. 1211-1219.
11. Li, T., A. Koong, and L. Xing, *Enhanced 4D cone-beam CT with inter-phase motion model*. *Medical Physics*, 2007. **34**(9): p. 3688-3695.

12. Maurer, J., T. Pan, and F.-F. Yin, *Slow gantry rotation acquisition technique for on-board four-dimensional digital tomosynthesis*. *Medical Physics*, 2010. **37**(2): p. 921-933.
13. Godfrey, D.J., et al., *Digital tomosynthesis with an on-board kilovoltage imaging device*. *International Journal of Radiation Oncology*Biography*Physics*, 2006. **65**(1): p. 8-15.
14. Wu, Q.J., et al., *On-Board Patient Positioning for Head-and-Neck IMRT: Comparing Digital Tomosynthesis to Kilovoltage Radiography and Cone-Beam Computed Tomography*. *International Journal of Radiation Oncology*Biography*Physics*, 2007. **69**(2): p. 598-606.
15. Godfrey, D.J., et al., *Evaluation of three types of reference image data for external beam radiotherapy target localization using digital tomosynthesis (DTS)*. *Medical Physics*, 2007. **34**(8): p. 3374-3384.
16. Ren, L., et al., *Automatic registration between reference and on-board digital tomosynthesis images for positioning verification*. *Medical Physics*, 2008. **35**(2): p. 664-672.
17. Daly, M.J., et al., *Intraoperative cone-beam CT for guidance of head and neck surgery: Assessment of dose and image quality using a C-arm prototype*. *Medical Physics*, 2006. **33**(10): p. 3767-3780.
18. Orth, R.C., M.J. Wallace, and M.D. Kuo, *C-arm Cone-beam CT: General Principles and Technical Considerations for Use in Interventional Radiology*. *Journal of Vascular and Interventional Radiology*, 2008. **19**(6): p. 814-820.
19. Schafer, S., et al., *Mobile C-arm cone-beam CT for guidance of spine surgery: Image quality, radiation dose, and integration with interventional guidance*. *Medical Physics*, 2011. **38**(8): p. 4563-4574.
20. Pohlenz, P., et al., *Intraoperative Cone-Beam Computed Tomography in Oral and Maxillofacial Surgery Using a C-Arm Prototype: First Clinical Experiences After Treatment of Zygomaticomaxillary Complex Fractures*. *Journal of Oral and Maxillofacial Surgery*, 2009. **67**(3): p. 515-521.
21. Westendorp, H., et al., *Intraoperative adaptive brachytherapy of iodine-125 prostate implants guided by C-arm cone-beam computed tomography-based dosimetry*. *Brachytherapy*. **6**(4): p. 231-237.

22. Quereshy, F.A., T.A. Savell, and J.M. Palomo, *Applications of cone beam computed tomography in the practice of oral and maxillofacial surgery*. *Journal of Oral and Maxillofacial Surgery*, 2008. **66**(4): p. 791-796.
23. Scarfe, W.C., A.G. Farman, and P. Sukovic, *Clinical applications of cone-beam computed tomography in dental practice*. *Journal of the Canadian Dental Association*, 2006. **72**(1): p. 75-80.
24. Cowen, A.R., S.M. Kengyelics, and A.G. Davies, *Solid-state, flat-panel, digital radiography detectors and their physical imaging characteristics*. *Clinical Radiology*, 2008. **63**(5): p. 487-498.
25. Jeromin, L.S., et al. *Productivity improvements with a direct digital radiography system integrated with PACS*. 1996: SPIE.
26. Mail, N., P. O'Brien, and G. Pang, *Lag correction model and ghosting analysis for an indirect-conversion flat-panel imager*. *Journal of Applied Clinical Medical Physics*, 2007. **8**(3): p. 137-146.
27. Siewerdsen, J.H. and D.A. Jaffray, *Cone-beam computed tomography with a flat-panel imager: effects of image lag*. *Med Phys*, 1999. **26**(12): p. 2635-47.
28. Siewerdsen, J.H. and D.A. Jaffray, *A ghost story: spatio-temporal response characteristics of an indirect-detection flat-panel imager*. *Med Phys*, 1999. **26**(8): p. 1624-41.
29. Siewerdsen, J.H. and D.A. Jaffray, *Optimization of x-ray imaging geometry (with specific application to flat-panel cone-beam computed tomography)*. *Medical Physics*, 2000. **27**(8): p. 1903-1914.
30. Yoo, S., et al., *A quality assurance program for the on-board imager[sup [registered sign]]*. *Medical Physics*, 2006. **33**(11): p. 4431-4447.
31. Smith, B.D., *Image reconstruction from cone-beam projections: necessary and sufficient conditions and reconstruction methods*. *IEEE Trans Med Imaging*, 1985. **4**(1): p. 14-25.
32. Mathias, P., *General principles of MDCT*. *European Journal of Radiology*, 2003. **45**, **Supplement 1**(0): p. S4-S10.

33. Ning, R., et al., *Flat panel detector-based cone beam computed tomography with a circle-plus-two-arcs data acquisition orbit: Preliminary phantom study*. *Medical Physics*, 2003. **30**(7): p. 1694-1705.
34. Tang, X. and R. Ning, *A cone beam filtered backprojection (CB-FBP) reconstruction algorithm for a circle-plus-two-arc orbit*. *Medical Physics*, 2001. **28**(6): p. 1042-1055.
35. Alexander, K., *Image reconstruction for the circle and line trajectory*. *Physics in Medicine and Biology*, 2004. **49**(22): p. 5059.
36. Katsevich, A., *Image reconstruction for a general circle-plus trajectory*. *Inverse Problems*, 2007. **23**(5): p. 2223.
37. Mail, N., et al., *The influence of bowtie filtration on cone-beam CT image quality*. *Med Phys*, 2009. **36**(1): p. 22-32.
38. Ning, R., et al., *Flat panel detector-based cone beam computed tomography with a circle-plus-two-arcs data acquisition orbit: preliminary phantom study*. *Med Phys*, 2003. **30**(7): p. 1694-705.
39. Ding, G.X., D.M. Duggan, and C.W. Coffey, *Characteristics of kilovoltage x-ray beams used for cone-beam computed tomography in radiation therapy*. *Phys Med Biol*, 2007. **52**(6): p. 1595-615.
40. Tkaczyk, J.E., et al., *Simulation of CT Dose and Contrast-to-Noise as Function of Bowtie Shape*, in *MEDICAL IMAGING 2004: PHYSICS OF MEDICAL IMAGING, PTS 1 AND 2*, Y. MJ and F. MJ, Editors. 2004: San Diego, CA. p. 403-410.
41. Graham, S.A., et al., *Compensators for dose and scatter management in cone-beam computed tomography*. *Medical Physics*, 2007. **34**(7): p. 2691-2703.
42. Bootsma, G.J., F. Verhaegen, and D.A. Jaffray, *The effects of compensator and imaging geometry on the distribution of x-ray scatter in CBCT*. *Medical Physics*, 2011. **38**(2): p. 897-914.
43. Siewerdsen, J.H. and D.A. Jaffray, *Cone-beam computed tomography with a flat-panel imager: magnitude and effects of x-ray scatter*. *Med Phys*, 2001. **28**(2): p. 220-31.
44. Glover, G.H., *Compton scatter effects in CT reconstructions*. *Medical Physics*, 1982. **9**(6): p. 860-867.

45. Endo, M., et al., *Effect of scattered radiation on image noise in cone beam CT*. Medical Physics, 2001. **28**(4): p. 469-474.
46. Ning, R., *Apparatus and method for x-ray scatter reduction and correction for fan beam and cone beam volume CT*. 2003, University of Rochester: United States.
47. Siewerdsen, J.H., et al., *A simple, direct method for x-ray scatter estimation and correction in digital radiography and cone-beam CT*. Medical Physics, 2006. **33**(1): p. 187-197.
48. Flohr, T., *Scatter correction based on raw data in computer tomography*. 2010: United States.
49. Jin, J.-Y., et al., *Combining scatter reduction and correction to improve image quality in cone-beam computed tomography (CBCT)*. Medical Physics, 2010. **37**(11): p. 5634-5644.
50. Niu, T.Y. and L. Zhu, *Single-scan scatter correction for cone-beam CT using a stationary beam blocker: a preliminary study*. Medical Imaging 2011: Physics of Medical Imaging, 2011. **7961**.
51. Yao, W. and K.W. Leszczynski, *An analytical approach to estimating the first order x-ray scatter in heterogeneous medium*. Medical Physics, 2009. **36**(7): p. 3145-3156.
52. Yao, W. and K.W. Leszczynski, *An analytical approach to estimating the first order scatter in heterogeneous medium. II. A practical application*. Medical Physics, 2009. **36**(7): p. 3157-3167.
53. Rinkel, J., et al., *A new method for x-ray scatter correction: first assessment on a cone-beam CT experimental setup*. Physics in Medicine and Biology, 2007. **52**(15): p. 4633-4652.
54. Zhu, L., N.R. Bennett, and R. Fahrig, *Scatter correction method for X-ray CT using primary modulation: Theory and preliminary results*. Ieee Transactions on Medical Imaging, 2006. **25**(12): p. 1573-1587.
55. Berbeco, R.I., et al., *Integrated radiotherapy imaging system (IRIS): design considerations of tumour tracking with linac gantry-mounted diagnostic x-ray systems with flat-panel detectors*. Phys Med Biol, 2004. **49**(2): p. 243-55.
56. Takai, Y., et al., *Development of real-time tumor tracking system with dmlc with dual X-ray fluoroscopy and amorphous silicon flat panel on the gantry of linear accelerator*.

- International Journal of Radiation Oncology*Biology*Physics, 2002. **54**(2, Supplement 1): p. 193-194.
57. Takai, Y., et al., *Development of a new linear accelerator mounted with dual X-Ray fluoroscopy using amorphous silicon flat panel X-Ray sensors to detect a gold seed in a tumor at real treatment position.* International Journal of Radiation Oncology*Biology*Physics, 2001. **51**(3, Supplement 1): p. 381-381.
 58. Koto, M., et al., *A phase II study on stereotactic body radiotherapy for stage I non-small cell lung cancer.* Radiother Oncol, 2007. **85**(3): p. 429-34.
 59. Jin, J.Y., et al., *Use of the BrainLAB ExacTrac X-Ray 6D system in image-guided radiotherapy.* Med Dosim, 2008. **33**(2): p. 124-34.
 60. Willoughby, T.R., et al., *Evaluation of an infrared camera and X-ray system using implanted fiducials in patients with lung tumors for gated radiation therapy.* International Journal of Radiation Oncology*Biology*Physics, 2006. **66**(2): p. 568-575.
 61. Speiser, M., et al., *FIRST ASSESSMENT OF A NOVEL IGRT DEVICE FOR STEREOTACTIC BODY RADIATION THERAPY*, in *World Congress on Medical Physics and Biomedical Engineering, September 7 - 12, 2009, Munich, Germany*, O. Dössel and W.C. Schlegel, Editors. 2009, Springer Berlin Heidelberg. p. 266-269.
 62. Depuydt, T., et al. *WE-C-BRA-06: The VERO System, a Novel IGRT Device for Stereotactic Body Radiation Therapy: Commissioning and First Experience.* 2010: AAPM.
 63. Depuydt, T., et al. *SU-GG-J-13: Geometric Accuracy of Real-Time Tumor Tracking with the Gimbaled Linac System of the Novel VERO SBRT System.* 2010: AAPM.
 64. Johnson, T., et al., *Dual-source CT cardiac imaging: initial experience.* European Radiology, 2006. **16**(7): p. 1409-1415.
 65. Johnson, T., et al., *Material differentiation by dual energy CT: initial experience.* European Radiology, 2007. **17**(6): p. 1510-1517.
 66. Bowsher, J.E., et al., *3D Trajectories for Limited-angle and Full-angle Dual-X-ray Conebeam CT Onboard Radiation Therapy Machines.* International Journal of Radiation Oncology Biology Physics, 2009. **75**(3): p. S581-S582.

67. Forthmann, P., M. Grass, and R. Proksa, *Adaptive two-pass cone-beam artifact correction using a FOV-preserving two-source geometry: A simulation study*. *Medical Physics*, 2009. **36**(10): p. 4440-4450.
68. Maurer, J., et al., *On-board four-dimensional digital tomosynthesis: First experimental results*. *Medical Physics*, 2008. **35**(8): p. 3574-3583.
69. Bruder, H., et al., *Correction of cross-scatter in next generation dual source CT (DSCT) scanners - art. no. 69131W*. *Medical Imaging 2008: Physics of Medical Imaging*, Pts 1-3, 2008. **6913**: p. W9131-W9131.
70. Engel, K.J., C. Herrmann, and G. Zeitler, *X-ray scattering in single- and dual-source CT*. *Medical Physics*, 2008. **35**(1): p. 318-332.
71. Kyriakou, Y. and W.A. Kalender, *Intensity distribution and impact of scatter for dual-source CT*. *Physics in Medicine and Biology*, 2007. **52**(23): p. 6969.
72. Petersilka, M. and et al., *Strategies for scatter correction in dual source CT*. *Medical Physics*, 2010. **37**(11): p. 5971.
73. Systems, V.M., ed. *PaxScan (R) 4030CB system and service guide*. Vol. P/N 20099 Rev. A. 2005.
74. (CPI), C.P.I., ed. *Indico 100 series x-ray generator*. Vol. P/N 746069-00 Rev. A.
75. Corporation, N., ed. *ESP300 motion controller/driver user's guide*. Vol. P/N 28187-02 Rev. F. 2002.
76. Scherz, P., *Practical Electronics for Inventors*. 2000, Washington D.C.: McGraw-Hill.
77. NI PCIe-6320. [cited 2011; Available from: <http://sine.ni.com/nips/cds/print/p/lang/en/nid/207404>].
78. Giles, W.M., *Timing and Communications for a Synchronous Dual X-ray System*, in *Medical Physics*. 2009, Duke University: Durham. p. 45.
79. Seet, K.Y., et al., *The effects of field-of-view and patient size on CT numbers from cone-beam computed tomography*. *Phys Med Biol*, 2009. **54**(20): p. 6251-62.
80. *Customer Release Notes: On-Board Imager Advanced Imaging (1.4)*. 2008, Varian Medical Systems Inc.

81. Feldkamp, L.A., L.C. Davis, and J.W. Kress, *Practical Cone-Beam Algorithm*. Journal of the Optical Society of America a-Optics Image Science and Vision, 1984. **1**(6): p. 612-619.
82. Canny, J., *A Computational Approach to Edge-Detection*. Ieee Transactions on Pattern Analysis and Machine Intelligence, 1986. **8**(6): p. 679-698.
83. Matsinos, E., *Current status of the CBCT project at Varian Medical Systems*. Medical Imaging 2005: Physics of Medical Imaging, Pts 1 and 2, 2005. **5745**: p. 340-351.
84. Labratory, T.P., *Catphan(R) 500 and 600 Manual*. 2006.
85. Ning, R., et al., *Flat panel detector-based cone-beam volume CT angiography imaging: System evaluation*. Ieee Transactions on Medical Imaging, 2000. **19**(9): p. 949-963.
86. Ning, R., X.Y. Tang, and D. Conover, *X-ray scatter correction algorithm for cone beam CT imaging*. Medical Physics, 2004. **31**(5): p. 1195-1202.
87. Bushberg, J.T., et al., *The Essential Physics of Medical Imaging*. 2 ed. 2002, Philadelphia: Lipincott Williams & Wilkins. 933.
88. Kyriakou, Y. and W.A. Kalender, *X-ray scatter data for flat-panel detector CT*. Physica Medica, 2007. **23**(1): p. 3-15.
89. Mail, N., et al., *An empirical method for lag correction in cone-beam CT*. Med Phys, 2008. **35**(11): p. 5187-96.
90. Petersilka, M., et al., *Strategies for scatter correction in dual source CT*. Med Phys, 2010. **37**(11): p. 5971-92.
91. Vaseghi, S.V., *Advanced digital signal processing and noise reduction*. 3rd ed. 2006, Chichester, West Sussex, England ; Hoboken: Wiley. xxvi, 453 p.
92. Zavarehei, E. *Spectral Subtraction*. 2011 [cited 2011; Available from: http://dea.brunel.ac.uk/cmisp/Home_Esfandiar/Spectral%20Subtraction.htm].

Biography

William Michael Giles

Date of Birth: April 29, 1985

Place of Birth: Grand Rapids, MI

EDUCATION

Ph.D. in Medical Physics (anticipated September 2012) Duke University, Durham, NC	2009-present
M.S. in Medical Physics Duke University, Durham, NC	2007-2009
B.S. in Physics Westminster College, New Wilmington, PA	2003-2007

PUBLICATIONS

W. Giles, J. Bowsher, H. Li, and F. Yin, "Crescent artifacts in cone-beam CT," *Med. Phys.* **38** 2116-22 (2011).

W. Giles, J. Bowsher, H. Li, and F. Yin, "Interleaved Acquisition for Cross Scatter Avoidance in Dual Cone-Beam CT" *Med. Phys.* (*under review*)

PRESENTATIONS

W. Giles, J. Bowsher, H. Li, and F. Yin, "Measurement-Based Cross-Scatter Correction in Dual Detector Cone-Beam CT" *Med. Phys.* **38** 3446 (2011).

W. Giles, J. Bowsher, and F. Yin, "A technique to correct crescent artifacts in in on-board CBCT." *Med. Phys.* **37** 3370 (2010).

- W. Giles**, J. Bowsher, and F. Yin, "Characterization of cross scatter in dual source CBCT," *Med. Phys.* **37** 3163 (2010).
- H. Li, **W. Giles**, J. Roper, J. Bowsher, and F. Yin, "Performance evaluation of a dual cone-beam CT (dual CBCT) system." *Med. Phys.* **37** 3385 (2010).
- J. Bowsher, **W. Giles**, J. Roper, H. Li, T. Zhuang, F. Yin, "3D Trajectories for Limited-angle and Full-angle Dual-X-ray Conebeam CT Onboard Radiation Therapy Machines." *Int. J. Radiat. Oncol. Biol. Phys.* **75(3)** S581-S582.
- W. Giles**, J. Bowsher, J. Roper, and F. Yin, "Impact of cross scatter on CNR in fluoroscopic images with a dual flat panel x-ray imaging system." *Med. Phys.* **36** 2475 (2009).
- J. Bowsher, **W. Giles**, J. Roper, L. Ren, and F. Yin, "Limited-Angle imaging for target positioning using orthogonal conebeam x-ray systems." *Med. Phys.* **36** 2476 (2009).
- H. Li, J. Bowsher, **W. Giles**, J. Roper, T. Li, and F. Yin, "Geometric calibration of a dual cone Beam CT system with large flat panel detectors." *Med. Phys.* **36** 2595 (2009).